UNIVERSAL FRAMEWORK FOR LINEAR MOTORS AND MULTI-AXIS STAGES WITH MAGNETIC LEVITATION

A Dissertation

by

VU HUY NGUYEN

Submitted to the Office of Graduate and Professional Studies of
Texas A&M University
in partial fulfillment of the requirements for the degree of

DOCTOR OF PHILOSOPHY

Chair of Committee,	Won-Jong Kim
Committee Members,	Reza Langari
	Alan Palazzolo
	Hamid Toliyat
Head of Department,	Andreas Polycarpou

December 2015

Major Subject: Mechanical Engineering

ABSTRACT

This dissertation presents the electromagnetic design and experimental validation of a new framework for linear permanent-magnet (PM) machines with targeted applications in precision motion control. In this framework, a single forcer, which can generate two independent force components in two perpendicular directions, consists of a stationary Halbach magnet array and two Lorentz coils with a phase difference of 90° or 270°. Any number of coil pairs can be attached on the same moving frame to work with a common magnet array or matrix, forming a linear or planar PM motor. Key advantages of this framework are simple force calculation, a linear system model, and a reduced number of coils for force generation and allocation in multi-axis positioners. The proposed framework effectively allows for decoupled dynamics, simplifying the linear controller design and real-time implementation.

To experimentally verify the theoretical framework proposed herein, a high-precision 6-axis magnetically levitated (maglev) stage is designed, constructed, and controlled. The development of this 6-axis positioning system is an integrated work, including magnetic-force calculation and analysis, mechanical design, fabrication, assembly, system modeling, system identification, and control system design. The mechanical components of the system include a stationary superimposed Halbach magnet matrix, which was previously built, and a moving platen with a plastic frame, four sets of 2-phase coils, and two precision mirrors. For position measurements, there are three laser interferometers for in-plane position measurements, three laser displacement sensors for out-of-plane position sensing, and two 2-channel Hall-effect sensors for the position feedback to initialize the position and expand the travel ranges of the platen in the *XY* plane.

The positioning resolutions of 10 nm in the *xy* plane and in the vertical axis are demonstrated. In out-of-plane rotation about the two horizontal axes, experimental results show the unprecedented positioning resolution of 0.1 μrad. The maximum travel range in *X* and *Y* with nanoscale positioning resolution is 56 mm × 35 mm, limited by the lengths of the precision mirrors attached to the platen. With the trapezoidal-velocity input shaping, achieved performance specifications include the maximum acceleration and velocity of 0.6 m/s^2 and 0.06 m/s, respectively, in translations in the horizontal plane. With the platen supported by the air bearings, the maximum acceleration and speed are 1.5 m/s^2 and 0.15 m/s, respectively. A load test is performed with the platen carrying a load of 0.54 kg, which is 72% of its total mass, magnetically levitated in 6-axis closed-loop control. Experimental results show the reduced coupled dynamics between different axes in magnetic levitation. This framework of 2-phase Lorentz coils and linear Halbach arrays is highly applicable in precision-positioning linear motors and multi-axis stages, steppers, scanners, nano-scale manipulation and alignment systems, and vibration isolators.

DEDICATION

For my parents and my parents in law, who brought me and my wife to life and always give my little family unconditional love and supports.

For Loan Nguyen, my beloved wife, who has been going with me through hardships with her great love, care, and patience.

For Huy Nguyen and Lily Nguyen, who carry not only my blood stream to the future, but also peace, calm, and joy.

In memory of Ngoi Nguyen, my beloved aunt,
and Tieu Nguyen, my beloved uncle.

ACKNOWLEDGMENTS

I cannot thank Dr. Won-Jong Kim, my thesis advisor, enough for his supervision of my research work at Texas A&M University. I would like to express my respect toward him for his professional knowledge, work ethics, and willingness to help and courage his students to study and do the research. I wish to thank Drs. Reza Langari, Alan Palazzolo and Hamid Toliyat for serving on my Ph.D thesis committee.

I wish to thank Mr. Van Le, Ph.D., Mr. Nghi Nguyen, M.S, Mr. Son Nguyen, Ph.D., Mr. Ninh Le, Ph.D., and Mr. Bang Nguyen, Ph.D., in Hanoi, Vietnam. They were my great teachers and colleagues. Without their help and support, I would not be able to start my graduate study in the United States.

I would like to thank the Vietnam Education Foundation (VEF) for its financial support in 2012–2014. Dr. Lynne McNamara, former Executive Director of VEF, had several inspiring talks that I still can remember as of today. Mrs. Sandarshi Gunawardena and Ms. Diana Martens at VEF were very resourceful and willing to help.

The office of Sponsored Student Program at TAMU took care of my applications when I first applied to A&M, and then processed numerous documents for me during my study here. I would like to thank Mrs. Violetta Cook, Mrs. Nancy Barnes, and Mrs. Angela Sanchez for all their works and helps. I also thank Mrs. Marisa Ernst and Mrs. Katherine Mears in the International Student Services for their works to allow for my program extension in Fall 2015. I would like to thank Dr. Lau Sai, Dr. Alan Palazzolo, Dr. Daniel McAdams, Mrs. Missy Cornett, and Mrs. Tandilyn Phillips for their advices and their administrative work in the Department of Mechanical Engineering.

The graduate students in the Precision Mechatronics Lab, including Yi-chu Chang, Jose Silva Rivas, Abdullah Algethami, Young-shin Kwon, Kuktae Kim, Ruikang Zhu, and Jin Fa Chen, have created a very friendly environment during the time I did my graduate study at TAMU. I would like to thank them for their friendship and their willingness to help others.

I wish to thank Mrs. Linda Caraway, Mr. Patrick Caraway, Mr. Tim Thornton, and Mr. Robert Wenck for their great friendship and for teaching me and my wife English when we first came to College Station.

The Vietnamese Aggies, including Hau Tran, Lien Tran, Thien Duong, Tin Dao, Bac Dao, Hoang Tran, Tho Tran, Trung Le, Huy Nguyen, Anh Nguyen, Duc Nguyen, Dung Dam, Dung Nguyen, Minh Tran, Tam Nguyen, Ngoc Do, Tina Mai, and Minh Kha, made me feel like home when I was half of the globe away from my home town. We have had a very exciting, funny, and meaningful college life in Aggieland.

My uncles, Ty Nguyen and Bang Nguyen, are the ones who have had strong influences on the development of my characteristics. My grandmother, Duyen Nguyen, was with me when I was born, raised me up until I was in my primary school, and now is still mentally supporting me in her nineties. I can never thank my grandmother and my uncles enough for everything they have done for me. Without unconditional love, care, supports, and encouragement from my parents, my parents in law, my wife, and my sisters, I would not be able to do what I wished to do. I owe them everything.

NOMENCLATURE

°C	Degree in Celsius
2D	Two Dimensional
3D	Three Dimensional
CPU	Central Processing Unit
ADC	Analog-to-Digital Conversion
DAC	Digital-to-Analog Conversion
DOF	Degree of Freedom
DSP	Digital Signal Processor
I/O	Input/Output
LTI	Linear Time Invariance
Maglev	Magnetically Levitated
MIMO	Multi-input Multi-output
OP Amp	Operational Amplifier
PID	Proportional Integral Derivative
PM	Permanent Magnet
RAM	Read Only Memory
RC	Resistor-Capacitor
Rms	Root Mean Square
VME	Versa Module Europa
VMEbus	Versa Module Europa bus

TABLE OF CONTENTS

LIST OF FIGURES

Page

LIST OF TABLES

Page

CHAPTER I

INTRODUCTION*

1.1 Literature Review

1.1.1 Precision Positioning

Precision positioning has broad applications, and is a key research area that concerns position, speed, or acceleration control of one or many moving parts with respect to the stationary frame of a mechanical system. In many such applications, the precision of the moving part's position should be on the order ranging from sub-nanometer to micrometer. Precision positioning stages have been widely used in machine tools, highly precise manipulation and assembly, stepping and scanning devices, and optical alignment. Nanopositioning became a research-and-development interest when nano-scale motions were required in applications including photolithography, data storage, microscopy, and material characterization.

All of the device components, dynamics modeling, control, and system integration regarding precision positioning are of interest in research and development as

---

[*] Part of this chapter is reprinted with permission from "A Two-Phase Framework for Linear Permanent-Magnet Machines and Multi-Axis Stages with Magnetic Levitation" by V. H. Nguyen and W.-J. Kim, in *Proc. 2014 ASME Dynamic Systems and Control* Conference, No. 5936, Oct. 2014, Copyright [2014] by ASME Publishing.

well as commercialization. The performance of a precision positioning system is characterized by the travel ranges or working space, positioning resolution, maximum speed and acceleration, and repeatability. The positioning resolution is the minimum step size that a motion stage can perform in step responses. It is the smallest step size that can be clearly seen and recognized in some appropriate scales of the position versus time plots. The repeatability is the capability of the stage to perform exactly the same motions in multiple trials. From the control-system-design viewpoint, the settling time and overshoot in error tracking responses are of concern. In case of multi-axis positioning stages, another key factor is the perturbations occurred in different axes when a motion in one axis is produced. Regarding mechanical design, it is helpful to highlight the ratio between the maximum travel range along an axis of the positioning stage and the dimension of the entire structure along the same direction.

Kim developed a 6-degree-of-freedom (6-DOF) magnetically-levitated (maglev) planar stage with a single moving part. This maglev stage had the travel range of 50 mm × 50 mm and the positioning noise of 5 nm rms in x and y [1]. Ayela *et al.* introduced a flexure-based micromachined electrostatic actuator for two-axis nanopositioning with capacitive displacement sensors [2]. The positioning resolution was sub-nanometer and the travel range was of a few micrometers. Snitka presented a 2-axis nanopositioning stage using ultrasonic actuators with the travel range and positioning resolution of 100 mm × 100 mm and 15 nm, respectively [3]. Gao *et al.* presented a surface motor-driven planar motion stage integrated with a 3-axis surface encoder for precision positioning [4]. Its motion range was 40 mm × 40 mm, and the positioning resolution was 200 nm.

Verma *et al.* designed and controlled a 6-axis maglev nanopositioning device having the capability to generate translations of 300 μm in *x*, *y*, and *z* [5]. Laser interferometers were used for position measurement; the positioning resolution was 5 nm, and the rms position noise in *x* and *y* was 2 nm. Hu and Kim developed an extended-range 6-DOF maglev planar stage with an optimized triangular configuration [6]. This maglev positioning system demonstrated a travel range of 160 mm × 160 mm in the horizontal plane with the positioning resolution of 20 nm. Kim and Verma constructed and controlled another magnetic-levitation-based multi-axis nanoscale positioning system with the travel range of 5 mm × 5 mm and the positioning resolution of 5 nm [7]. Zhang and Menq presented a 6-axis maglev motion-control stage with the working volume of 8 mm^3 and the positioning accuracy of 1.1 nm rms in *x* and 0.74 nm rms in *y* [8]. Yao *et al*. developed a piezo-driven parallel-kinematics flexure nanopositioning system with capacitive gauges [9, 10]. Achieved motion range and resolution were 85 μm in each axis and 2–4 nm, respectively. Yong *et al.* presented the design, identification, and control of a flexure-based *XY* nanopositioning stage using piezoelectronic stack actuators [11]. It was able to scan over a range of 25 μm × 25 μm in high-speed scanning at 400 Hz. Polit and Dong developed a high-bandwidth *XY* nanopositioning stage using piezoelectric stack actuators and two capacitive gauges [12]. The stage could travel 15 μm along each axis with the resolution of 1 nm. Shinno *et al*. developed a single-axis positioning table system with a laser interferometer [13]. Aerostatic bearings were used to support a primary table on top of a secondary table, and voice-coil motors were used to actuate the primary table. Its travel range was 150 mm and the resolution was at sub-nanometer. Fesperman *et al.* constructed and controlled a multi-scale positioning and alignment system for nanomanufacturing with the travel range of 10 mm × 10 mm in *XY* and the positioning resolution of 1 nm [14]. Another structure for precision positioning with two moving masses was presented in [15] where the fine positioning was actuated by piezoelectric stack actuators. Xu designed and controlled a flexure-based *XY* positioning system with the working space of 11 mm × 11 mm and the positioning resolution of 200 nm [16].

A crossed-axis long-stroke nanopositioning stage is commercially available from Aerotech Incorporated[1]. The stage shown in Fig. 1-1 uses cross-roller bearings and direct-driven ironless linear motors [17]. The maximum travel range is 160 mm and the positioning resolution of 1 nm. Physik Instrumente[2] offers a 6-axis piezoelectric-actuated stage with 2.2-nm positioning resolution in x and y [18]. The translation working volume is 800 μm × 800 μm × 200 μm, and the rotational range is 10 mrad.

Fig. 1-1 Aerotech's ANT130-XY stage (photo courtesy of Aerotech, Inc.) [17].

---

[1] Aerotech Inc., 101 Zeta Drive, Pittsburgh, PA 15238, U.S.A

[2] Physik Instrumente (PI) GmbH & Co. KG, Auf der Roemerstrasse 1, 76228 Karlsruhe, Germany

From the observations of the nanopotioning stages presented in a chronological order above, existing stage structures primarily fall into the three main categories as follows. The first type is the combination of a coarse stage and a fine stage [13, 15], which are controlled cooperatively. The coarse stage that generates long-stroke translation is supported and guided by conventional sliding bearings. The fine stage, which sits on top of the coarse stage, can be supported by aerostatic or magnetic bearings and actuated by voice-coil or piezoelectric actuators. This design offers the advantages of long travel ranges on the order of hundreds of millimeters. The cost to pay is its bulky mechanisms, complicated control scheme, and lack of capability to perform motions in more than 2 DOFs. The second type is the multi-axis flexure-based stages actuated by piezoelectric motors or voice-coil actuators. An advantage of this design is good machinability with no bearings needed. A drawback is the short travel range in the order of 10 μm [11, 19] and 1 mm [16]. In addition, the force required to drive the stage is highly nonlinear with respect to the position and very large at the end of the travel ranges [20]. The third type is the single-moving-part maglev positioning stages [1, 5–8]. Regarding position sensing for nanopositioning, capacitive sensors can measure the displacements in sub-nanometer resolution, but the sensing range is limited to the order of 1 mm or below. Laser interferometers can measure the long travel range on the order of 100 mm with the resolution on the order of 1 nm. The challenge with laser interferometers is that ambient-temperature fluctuation and air flow may negatively affect the measurement results. Maglev nanopositioning stages are still in the research phase and not commercially available up to date. However, single-moving-part maglev structure is the only design that can offer 6-axis positioning capability with a nanometer resolution and the *XY* travel range in the order of 100 mm. Fig. 1-2 shows a photograph of the extended-range 6-DOF maglev nanopositioner developed by Hu and Kim [6].

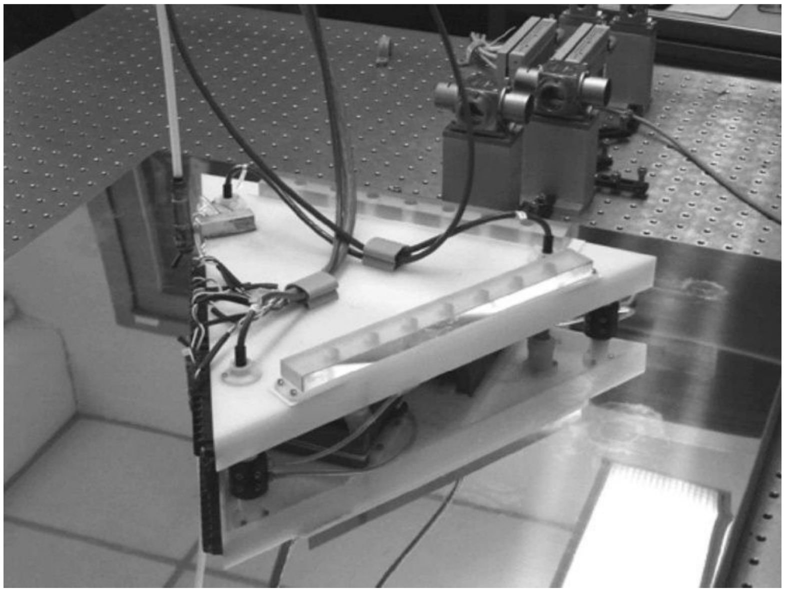

Fig. 1-2 The 6-DOF maglev planar stage that has a triangular configuration and the extended travel range of 160 mm × 160 mm [6].

1.1.2 Magnetic Levitation

Magnetic levitation is the technique that allows an object to be suspended by magnetic forces with the capability of stabilizing or controlling its position and speed. In 1905 and 1907, two patents on train cars propelled by direct-driven linear electric motors were granted to Alfred Zehden, a German inventor [21, 22]. In 1959, Polgreen, an English engineer, filed a patent on a magnetic system for transportation with a vehicle being levitated by magnetic forces [23]. Extensive research and development of maglev vehicles began back in the 1960s in Germany and Japan. Electromagnetic-levitation vehicle was first tested in West Germany in 1971 with the maximum speed of 200 km/h

[24]. An electrodynamic-levitation vehicle was first tested in Japan in 1972 and in West Germany in 1976 [24]. Research efforts and results in magnetic levitation, propulsion, and guidance included the ones presented in [25–37]. Comprehensive reviews of the research and developments in this area can be found in [24, 38–43]. To date, the fastest maglev train in the world is the JR-Maglev MLX01 in Japan with the recorded speed of 581 km/h [44].

In the laboratory scale and for various purposes, maglev devices have been designed since 1980s for motors with and without bearings [45–48], carrier systems and conveyors [49–51], precision positioning and manipulation [1, 5–8, 52–56], haptics and force feedback [57, 58], micro-robotics [59, 60], vibration reduction or isolation [61], and energy harvesting [62–65]. Fig. 1-3 shows a 3D rendering and a photograph of the maglev steel conveyor system developed in [49].

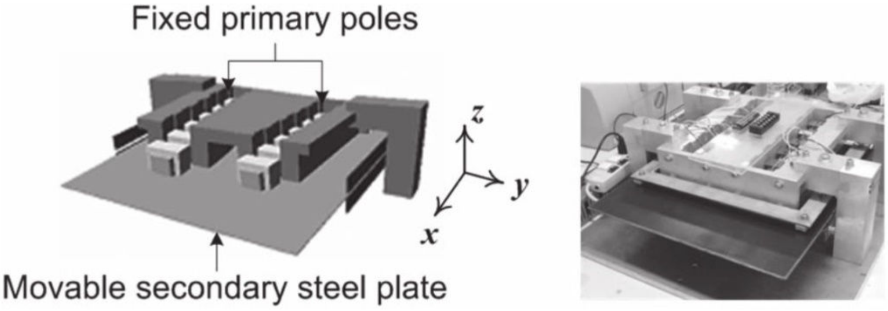

Fig. 1-3 The industrial maglev steel conveyor system [49].

The levitation force can be generated with 1) diamagnetic materials and permanent magnets (diamagnetic levitation), 2) time-varying magnetic field and superconducting plates or short-circuit tracks (electrodynamic levitation), 3) electromagnets and ferromagnetic materials or permanent magnets (electromagnetic levitation), 4) Lorentz coils and permanent magnets, and 5) permanent magnets in both the mover and the stator (PM passive levitation). In the first and second cases, no control is required to stabilize the position of the levitated part at some equilibrium points above the base. In the third and fourth cases, closed-loop control is required to stabilize and control the position of the levitated part. In electrodynamic levitation, the currents induced in a superconducting plate or short-circuit tracks generate the magnetic field that opposes the change in the varying magnetic field, forming a repulsive force between the mover and the stator. In electromagnetic levitation, the levitation force is attractive. Therefore, part of or the entire mover must be placed below the stator. In Lorentz-force levitation, the force between the stator and the mover can be actively controlled to be attractive or repulsive to stabilize the mover.

Magnetic levitation offers the advantages of frictionless and contactless motions, avoiding the effects of wear and surface damage, eliminating the need of lubricants, minimizing the cost of maintenance, and extending the lifetime of the motion-control systems. The nonlinearity of friction forces are avoided in maglev systems, making the dynamic models more accurate. The cost to pay is the sensors for out-of-plane position measurements and the extensive effort needed for control and testing to guarantee the stability, safety, and performance for the maglev device.

1.1.3 Maglev Nanopositioning

Magnetic levitation nanopositioning offers the advantage of non-contact and backlash-free motions with a precise force model due to the absence of mechanical friction. Trumper *et al.* introduced the utilization of linear Halbach magnet arrays for magnetic levitation [66]. This laid the foundation for a number of research results in maglev motors developed thereafter. In this structure, each forcer has a linear Halbach magnet array on top of 3-phase air-core stator windings and can generate two force components in the normal and transverse directions. The working sides of the coils are parallel to the magnet bars, and three phases of coil windings fit exactly half of a spatial pitch of the magnet array. The normal force is to levitate the moving magnets magnetically. The magnetic field due to the stator currents on the bottom surface of the magnet array was calculated by transfer relations [53]. With the pre-calculated field solution of the Halbach magnet array, the magnetic force acting on the moving part was computed by Maxwell stress tensors. Kim designed and controlled the world's first 6-DOF maglev planar motor [1]. The framework of 3-phase coil windings working with linear Halbach magnet arrays was formulated, and the control of associated planar stages was validated in [53, 54]. Fesperman *et al.* constructed and controlled the actuators for a multi-scale alignment and positioning system for micro-imprint [14]. Hu and Kim and Yu and Kim developed 6-DOF maglev stages using the same framework, but the coils were moving over a concentrated-field magnet matrix [6, 67].

Zhang and Menq developed a 6-DOF maglev stage actuated by three two-axis Lorentz-force linear actuators, as shown in Fig. 1-4 [8]. The magnets and an associated steel loop structure generated a nearly uniform magnetic field, which simplifies the force-current relation to be linear. The travel range is 2 mm × 2 mm × 2 mm, and that of the rotational motions is 4° × 4° × 4°. The structure of the two-axis linear actuator in this case did not offer the long-range linear motions in the horizontal plane. However, the design, by its nature, allowed for certain rotation angles of the mover about different axes without much error in the force model. Fulford and Maggiore presented a 5-DOF maglev stage with the mover, which carries the magnets, being suspended below the slotted stator with 3-phase coil windings [56]. The moving part was primarily levitated by the attractive force between the magnets and the stator's back iron. With the attractive force for levitation against gravity, a part of or the entire mover must be located under the motor stator. The advantage is that the currents required to levitate the mover are smaller than those in the case of air core.

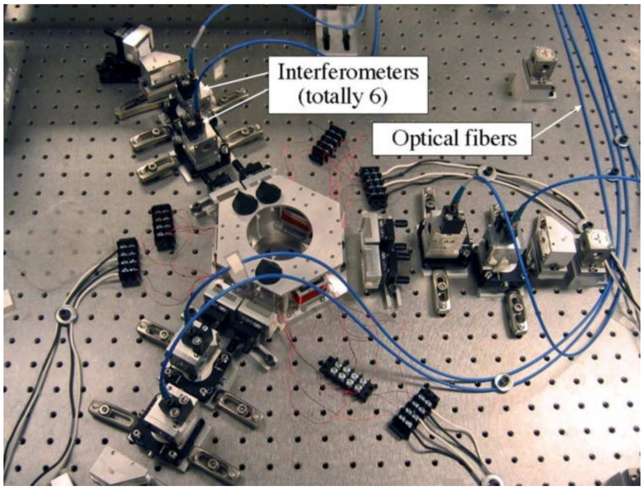

Fig. 1-4 A photograph of the 6-axis maglev nanopositioning stage developed by Zhang and Menq [8].

Among the maglev-stage designs for precision positioning, the stages in [1, 5, 7, 8] had absolutely no mechanical contact between the movers and the stationary parts. The stages in [56, 68] were shown to have the sensing frames to support the movers. The ones in [6, 67] had only the power cables and sensor wires (in [67]) connecting the moving parts with the base. Fig. 1-5 is a photograph of the 6-axis maglev stage presented in [7].

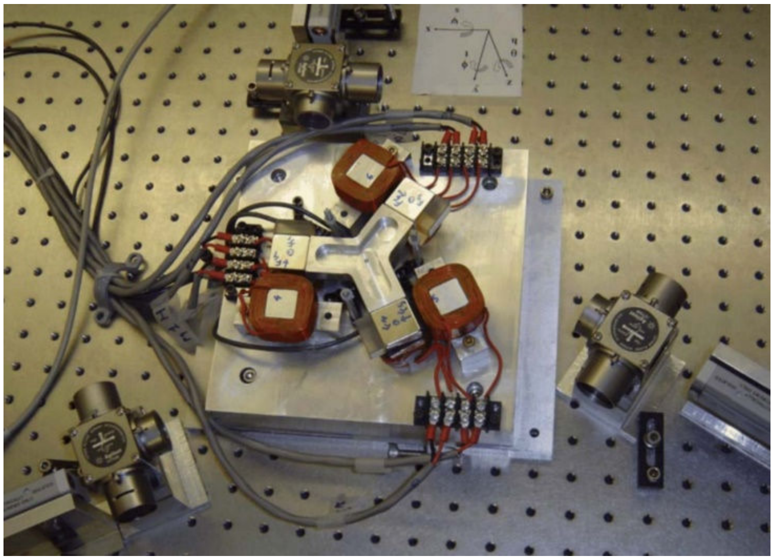

Fig. 1-5 A photograph of the maglev stage developed by Verma and Kim [7].

1.2 Design Considerations and Objectives

1.2.1 Design Considerations

For linear motors and multi-axis stages, there are air bearings, flexures, and magnetic bearings, in addition to conventional mechanical bearings. Air bearings can be assembled and operated with ease, but dust particles in compressed air make them inapplicable in vacuum and clean-room environments. Moreover, the dynamics of air bearings is highly dependent on the pressure of the compressed air and, therefore, subject to vibrations in the vertical direction. Flexures have been constructed and used along with piezoelectric actuators in *XYZ* stages [19] and electromagnetic actuators in *XY* stages [16, 20]. These structures offer the benefits of no friction or backlash at low cost. However, the flexure stiffness is nonlinear with a very high value at the maximum displacement, which is roughly 150 N/mm [20]. The actuators must be sufficiently strong and are power-consuming to drive the mover to travel along the entire travel ranges. The travel ranges of the positioning systems in and [16, 20] are 10 mm × 10 mm and 11.75 mm × 11.66 mm, respectively. The ratio between the maximum displacement and the dimension of the flexure is small, being approximately 1/10 in [16]. For vibration isolation, flexures are no perfect solution because multi-axis vibrations are transmitted from external structures to the moving parts through the supporting mechanisms.

Maglev multi-axis stages were demonstrated to have the *xy* motion ranges of 50 mm × 50 mm [1] and 160 mm × 160 mm [6] with a nanoscale positioning resolution and 100 mm × 100 mm [56] with a microscale positioning resolution. For a planar maglev stage using a magnet matrix and an array of Lorentz coils, the nominal travel range is the difference between the dimension of the magnet matrix and that of the coil array. Therefore, the ratio between the maximum displacement and the dimension of the structure can be designed to be much larger than that of flexure-based stages. In [67], this ratio is 5.24/10. Maglev linear motors and multi-axis stages have various potential applications in the systems that strictly require high positioning precision, long motion ranges, vibration isolation of the mover, and clean-room conditions.

For maglev stages, given several trade-offs between the moving-coil and stationary-coil configurations, this work focuses on the moving-coil design due to two main reasons. First, the rectangular coil's shorter sides that are not useful for force generation can be bent and farther away from the magnet surface. This significantly reduces the end effect of the coils and avoids the undesired forces from the coil's shorter sides, making the force calculation and allocation much simplified. Second, the stationary magnet arrays can be utilized in position sensing to extend the travel range of the movers. For in-plane position sensing in x and y, laser interferometers give excellent precision without depending on the distance between the sensor heads and the mirrors. However, the rotation angle about the vertical axis sensed by a combination of laser interferometers is limited because the reflected laser beams from the mirrors must be aligned and go into the receivers. In a moving-coil structure with a fixed magnet array, the magnetic field generated by the magnet array can be measured by Hall-effect sensors attached on the moving part. By this, the angular motion range is greatly increased [67].

1.2.2 Two-Phase Forcer

Figure 1-6 shows the 3-D rendering of a 2-phase forcer, the fundamental unit of the framework developed in this research. The forcer consists of two moving coils with a phase difference of 270° placed in parallel with a Halbach magnet array. This structure of the magnet array has the advantage of concentrating the magnetic flux on one side [66]. Four adjacent magnet blocks form a spatial pitch of the magnet array, which is denoted by L. On a plane parallel to and close to the Halbach array's strong side, both normal and transverse components of the magnetic flux density vary sinusoidally with position. Based on this fact, a forcer can be designed with two longer sides of each coil placed at a distance of half the Halbach array's spatial pitch. Two coils are needed to produce two independent force components in the normal and transverse directions.

The two coils in a 2-phase forcer can be made to be overlapped to further reduce the volume that the coils occupy. A longer side of each coil fills the space between two longer sides of the other coil, forming a more compact structure with higher power density. In this case, two coils of a forcer have a phase difference of 90° instead of 270°. However, the force-generation principle and the force calculation stay essentially the same. This configuration is tested in the work presented herein.

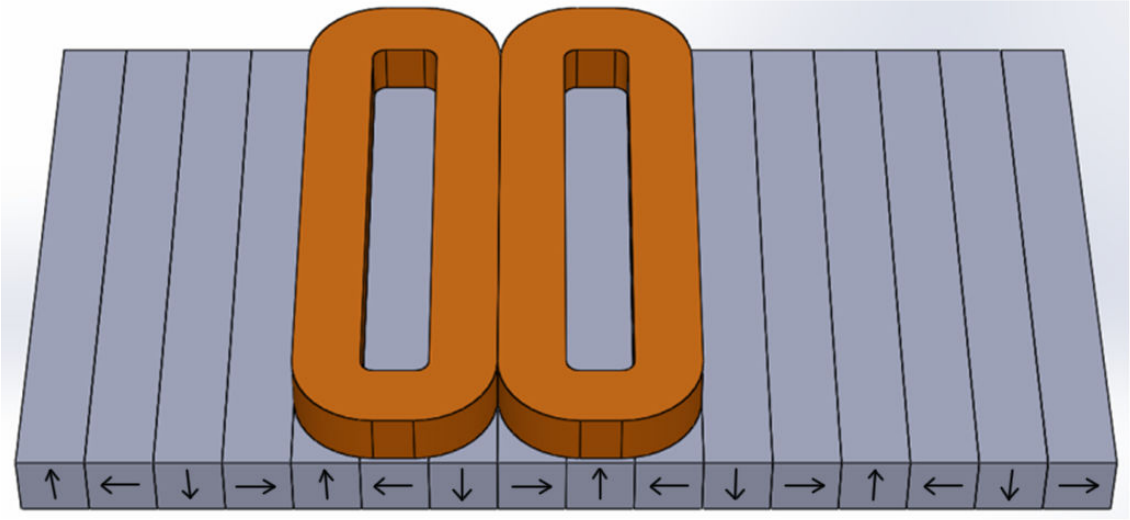

Fig. 1-6 3D rendering of the forcer with two coils above the Halbach magnet array [75].

With two independent force components generated by a forcer, multiple forcers can be combined to form a single-axis linear motor or a multi-axis stage. Different coil pairs can work with magnet arrays arranged in a plane to form a planar motion-control stage. For a 6-axis maglev stage, at least three forcers are required. In order to have a symmetric structure in both the *x*- and *y*-axes and to make the force allocation simple, four forcers are currently employed for a 6-axis maglev stage. In this work, the 2-phase framework in [69] that could only generate 3-DOF planar motions is expanded to allow for all out-of-plane motions with magnetic levitation.

1.2.3 Design Objectives

The main objective of this research work is to develop a theoretical framework using Lorentz coils and linear Halbach magnet arrays for linear motors and multi-axis stages and to experimentally validate the framework by a 6-axis maglev nanopositioning stage. The linear force model allows for real-time controller design and implementation at the sampling rate of up to 4 kHz. The coil arrangement and the design of the moving parts allow for the decoupled dynamics between different control axes, reducing the vibrations during high-precision motions. The positioning stage is targeted to have the position resolution of 10 nm over a working range in the order of tens of millimeters in x and y and carry a load of hundreds of grams. In translations in the order of millimeters along X and Y, this stage is targeted to have the settling time within a few hundreds of milliseconds.

1.3 Dissertation Contributions

In this research project, a universal 2-phase framework of Lorentz coils and linear Halbach magnet array is developed for applications in linear motors and multi-axis stages. A 6-DOF nanopositioning stage has been constructed and controlled to verify the theoretical framework. In this framework, each forcer has two planar rectangular coils placed above a linear Halbach magnet array and separated by a 270° or 90° phase difference. The overlapped coil is essential for a compact moving platen. The shorter coil sides were bent away from the magnet array, reducing the undesired fringing effects of the coil sides that are not useful for force generation. The design simplifies the

Lorentz-force calculation and allocation, allowing for real-time control design and implementation.

Compared to the 3-phase moving coils in [6, 67] with only one side of each coil contributing to the force generation, the moving coils in our forcer have two sides of each coil being used. Provided that the width of each coil side in Fig. 1-6 and that of the magnet blocks are equal, the two coils in this framework cover a spatial width of 1.5 L while nine coils were required for the same spatial width in [6, 67]. With the same maximum currents, the peak force generated by this 2-phase forcer is 2/3 that of the 3-phase forcer with 9 coils with the same coil thickness and coil length. The total coil volume of the 2-phase forcer is only 1/3 that of the 3-phase forcer. Hence, the power density of the 2-phase forcer is twice that of the 3-phase forcer. Another benefit is that the number of required power amplifier units is two for a 2-phase forcer whereas a 3-phase forcer requires three units.

The aforementioned 2-phase framework is validated by a newly developed 6-DOF maglev stage. The moving part is a compact frame carrying Lorentz coils and the stationary part is a concentrated-field Halbach magnet matrix [1, 6, 69, 70]. Figure 1-7 is a photograph of the experimental setup. The key in the arrangement of the coil pairs on the moving platen is that the number of forcers contributing to the force allocation for each axis is minimized. This simplifies the relation between 6 resultant forces (3 for in-plane motions and 3 for out-of-plane motions) and the currents flowing in the coils on the platen. Moreover, each forcer participating in the dynamics of a less number of axes implies that the coupled dynamics among axes are reduced. With the four forcers arranged in a cross configuration, each axis can be fully actuated by only two forcers, except for the *Z*-axis translational motion.

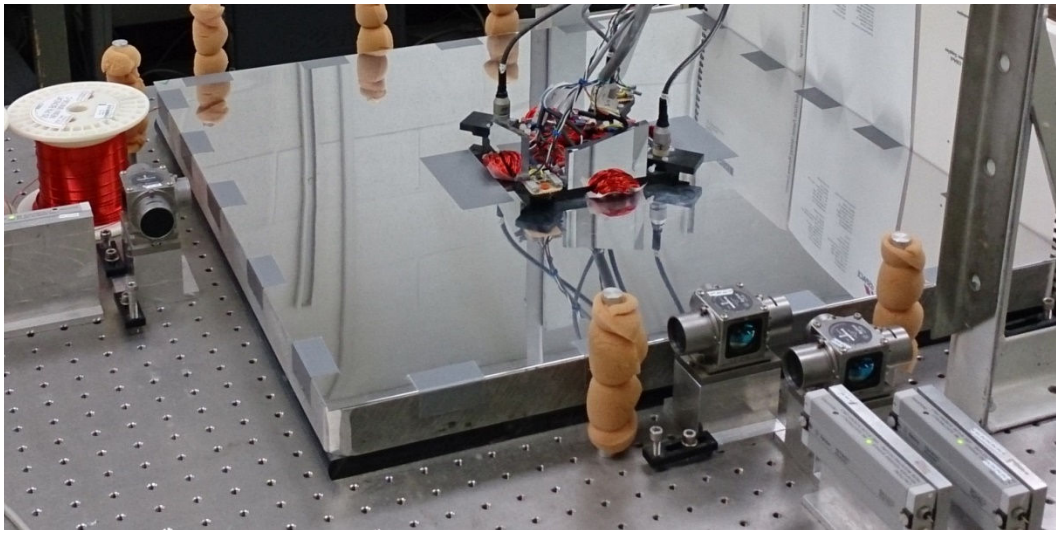

Fig. 1-7 A photograph of the moving platen above the magnet matrix.

The control of the 6-axis maglev stage developed herein is subjected to the force disturbances caused by the umbilical cables and model uncertainties from the coil fill factor and mechanical fabrication errors. To model the dynamics of the 6-axis maglev stage's out-of-plane control axes better, system identification is performed. The platen is levitated by a DC control effort in Z to a certain height within 40 µm while the control loops in X, Y and θ_z are closed. The effect of the DC control effort in Z and the cables connected to the platen can be represented by a spring constant and a damping coefficient added to the theoretical models in Z, θ_x, and θ_y. Two experiments are designed and conducted to identify these spring constants and damping coefficients. With the identified out-of-plane models, PID controllers are designed and tuned to give satisfactory performance in all 6 axes.

Experimental results are given to demonstrate the achieved positioning resolution, maximum speed and accelerations, maximum travel ranges, reduced coupling effects between different control axes, and load-carrying capability of the positioning stage. The achieved positioning resolution in *X*, *Y*, *Z*, out-of-plane rotation, and rotation about the vertical axis are 10 nm, 0.1 μrad, and 1 μrad, respectively. The maximum speed and acceleration in magnetic levitation are 60 mm/s and 0.6 m/s^2, respectively. With air bearings, the results are 150 mm/s and 1.5 m/s^2. The maximum travel ranges in the *XY* plane with the laser interferometers for position sensing are 56 mm in *X* and 35 mm in *Y*, respectively, dependent on the lengths of the precision mirrors. A load test demonstrates the capability of the stage to carry an extra mass of 539.6 g when the platen is magnetically levitated and the closed-loop controllers effectively drive its out-of-plane positions to the references.

The 6-DOF maglev stage developed in this work is targeted for a variety of applications, including micro- and nano-precision manipulation and assembly, stepping and scanning, and vibration isolation. The framework presented herein can also be applied for moving-magnet linear motors and motion-control stages with the dimension of the moving magnet array in the translational direction being relatively larger than that of the stationary coils. This is to reduce the end effects of the magnet arrays and guarantee the Lorentz-force model's accuracy.

CHAPTER II

A NEW FRAMEWORK FOR LINEAR MOTORS AND MULTI-AXIS STAGES WITH 2-PHASE LORENTZ COILS AND A LINEAR HALBACH ARRAY*

2.1 Linear Halbach Magnet Array

2.1.1 Brief History of the Linear Halbach Array

In 1973, Mallinson proposed a planar structure with sinusoidally varying magnetizations and theoretically proved that the magnetic scalar potential in one side of the structure is zero. Fig. 2-1 illustrates the magnetization patterns that yield such property. Here, x is the horizontal axis, y is the vertical axis with the upper surface at $y = 0$, m_x and m_y are the magnetizations in x and y, respectively.

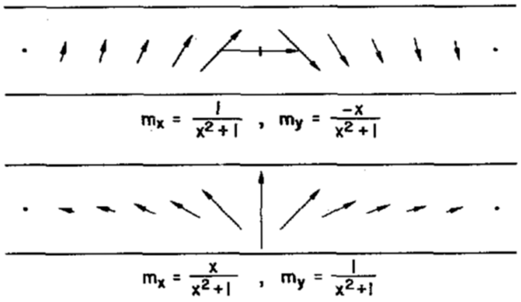

Fig. 2-1 Magnetization patterns that do not generate the fluxes on one side of the structure [71].

---

*Part of this chapter is reprinted with permission from "A Two-Phase Framework for Linear Permanent-Magnet Machines and Multi-Axis Stages with Magnetic Levitation" by V. H. Nguyen and W.-J. Kim, in *Proc. 2014 ASME Dynamic Systems and Control* Conference, No. 5936, Oct. 2014, Copyright [2014] by ASME Publishing.

Halbach in 1980 presented the segmented multipole magnet, as shown in Fig. 2-2, and calculated the field produced by this magnet structure [72]. This laid the foundation for the linear magnet arrays used in the linear undulators [73–74]. Fig 2-3 shows the experimental setup using the linear Halbach arrays to produce elliptically polarized synchrotron light [74].

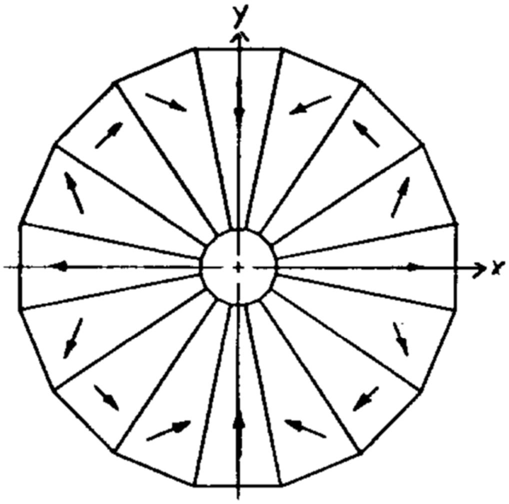

Fig. 2-2 A Cross-sectional view of a 16-segment circular Halbach array [72].

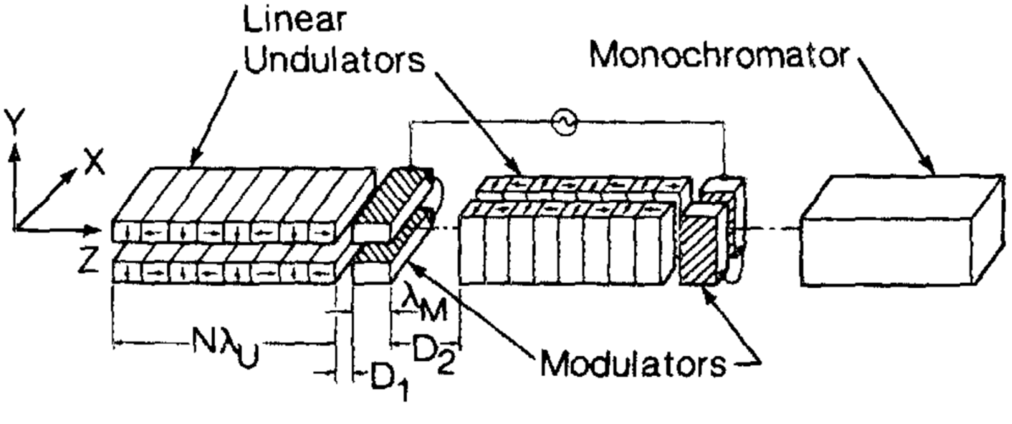

Fig. 2-3 The setup to generate elliptically polarized synchrotron light [74].

A linear Halbach magnet array is a planar structure comprising of a number of magnet bars with the same thickness, the same length, and the magnetization directions rotating in one direction (either clock-wise or counter clock-wise) along the axis parallel with the width of the magnet bars, as shown in Figs. 2-3, 4, and 5. The fluxes are focused on one side of the structure, where there are two magnetic flux-density components in the directions of the width and the thickness of the magnet array. In Fig. 2-4, the length of the magnet bars is in the direction perpendicular to the drawing plane.

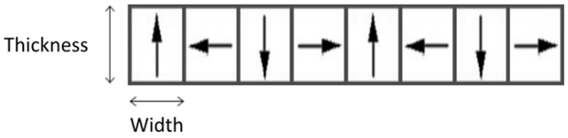

Fig. 2-4 The convention on the thickness and width of the magnet bars in a linear Halbach array.

Trumper *et al.* demonstrated the applicability of Halbach arrays in synchronous machines [66]. In this work, a particular configuration of linear Halbach array was of interest. There were four magnet bars per spatial pitch of the linear Halbach array and each magnet bar had the square cross section. The fundamental field on the strong side of this array was shown to be within 90% of the field of the ideal array in which the rotation is continuous [66].

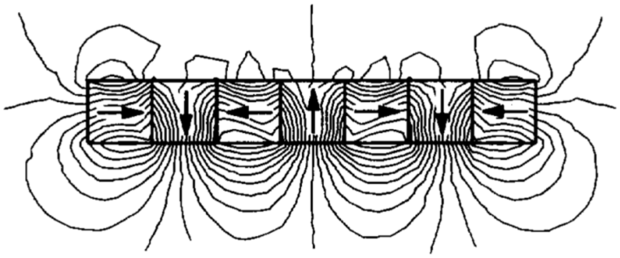

Fig. 2-5 A linear Halbach array with 4 identical magnet bars per spatial pitch [66].

The magnet array as in Fig. 2-5 only has one type of magnet bars. This allows for the assembly of the magnet array more readily implementable due to the commercial availability of such magnet bars. This array has the magnetic field strengthened on one side and weakened on the other side, generating a magnetic flux density being $\sqrt{2}$ times stronger than that of a conventional magnet array [66]. This magnet structure is highly applicable in single-sided linear PM motors and actuators to enhance the force density. It is targeted to the Lorentz-force linear electric machines where cogging forces need to be avoided and the good linearity of the force model is of importance.

2.1.2 Field Solution

Fig. 2-6 illustrates a linear Halbach magnet array having 17 identical magnet blocks. The side that has strong magnetic field corresponds to the positive *z*-direction. Over the top surface of the magnet array, the magnetic field has two components in the *y*- and *z*-directions.

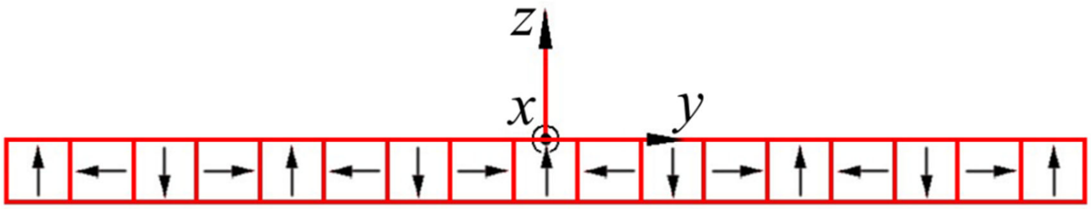

Fig. 2-6 A Cross-sectional view of a linear Halbach array.

With the assumption that the magnet array is infinitely long in the *y*-direction, the field solution was derived in [1, 53, 66]. The *y*- and *z*-direction magnetic flux-density components at the point (*y*, *z*) above the top surface of the magnet array are, respectively

$$B_y(y,z) = \sum_{k=0}^{+\infty}(-1)^k c_n(z)\sin(\gamma_n y) \tag{2.1}$$

$$B_z(y,z) = \sum_{k=0}^{+\infty}(-1)^k c_n(z)\cos(\gamma_n y), \tag{2.2}$$

where

$$c_n(z) = \frac{2\sqrt{2}\mu_0 M_0}{\pi n}(1 - e^{-\gamma_n \Delta})e^{-\gamma_n z}. \tag{2.3}$$

Here, $n = 4k + 1$, μ_0 is the permeability of the free space, M_0 is the peak magnetization of the magnets, L is a spatial pitch of the magnet array, $\gamma_n = 2\pi n/L$, and Δ is the thickness of the magnet array along the z-direction.

2.2 Framework of 2-Phase Lorentz Coils and a Linear Halbach Array

2.2.1 Introduction to the Framework

The cross-sectional view of a forcer, which has two planar coils moving over a fixed linear Halbach array is shown in Fig. 2-7. Taking the advantage of the sinusoidally varying magnetic flux density along the *y*-direction, the rectangular coil's dimensions are designed so that the two long sides are spatially separated by 180° or half of the pitch of the Halbach array. By having this, the magnetic flux densities are distributed equally (in magnitude) but in the opposite directions in the volumes of the two coil sides. The Lorentz forces of the two sides of each coil end up being the same and the resultant force is twice as much as that generated by each side. This helps simplify the Lorentz force calculation and increase the peak force generated by each coil.

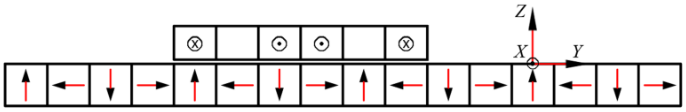

Fig. 2-7 A cross-sectional view of the coil sides and magnet bars with the electric current and magnetization directions [75].

This structure of two planar Lorentz coils can generate two independent force components, one in the *y*-direction and the other in the *z*-direction. Two coils are needed due to a number of reasons. If only one coil is used, when it moves along the *y*-direction, there must be the locations where the magnetic flux density is equally distributed in the volumes of the two long coil sides. In this case the resultant Lorentz force generated by the two coil sides is zero regardless of how large the electric current is. Therefore, to guarantee the force generation capability at any points along the *Y*-axis, there must be at least two coils used. Practically the concept of a forcer having two coils may not be needed. One may place a certain number of coils separated in an axis *x* or *y*, perform the Lorentz force calculation and establish the force model for the actuator. However, for the convenience of grouping the coils for force allocation in different directions and control of the structure having multiple coils, it is necessary to have the building block to construct more complicated actuating systems. For the mechanical designs to be compact, the force model to be simple, and the number of power amplifier units to be simplified, it is feasible that a forcer has two coils.

The two coils must be separated by an angle not being a multiple of 180°. If the two coils are spatially separated by 180°, when the resultant Lorentz force generated by one coil is zero due to the magnetic flux density distributed equally in its two long sides, the other coil has the same problem. In case the two coils are separated by an angle of 90° or 270°, when one coil can only generate zero force, the other coil generates the maximum force. In addition, the analytical result of the resultant Lorentz force generated by two coils stay sufficiently simple for the purpose of control system design and implementation.

To derive the force model, the two independent and orthogonal Lorentz-force components generated by two coils of a forcer are calculated by volume integration with the precalculated field solution of the Halbach magnet array. The volume integration was started from a right-rectangular-prism coil side placed over the linear Halbach array, as in Fig. 2-7. The forces for one and two coils are then interpreted. The analytical result is compared to that from the finite element method (FEM) with some particular dimensions of the structure.

2.2.2 Lorentz-Force Calculation for a Right-Rectangular-Prism Coil Side

To establish the current-force relation for a 2-phase forcer with two coils placed over a linear Halbach magnet array, a right-rectangular-prism coil side, as in Fig. 2-8, is considered. The force calculation is approximated with the assumption that all parts of the coil turns in the coil sides are straight-line segments. In practice, the coil turns slightly bend near the end of the coil sides to curve around the corners. For the two longer coil sides in Fig. 2-9, the transverse force is due to the z-direction magnetic-flux density $B_z(y, z)$, and the normal force is due to the y-direction magnetic-flux density $B_y(y, z)$. Volume integration is performed to calculate the resultant Lorentz force acting on the right-rectangular-prism coil side in the z- and y-directions. The base point from which the integration is taken is (x_1, y_1, z_1), as noted in Fig. 2-8. In the field solution given by (2.1) and (2.2), the total y- and z-direction flux densities are expressed in the form of Fourier-series expansions with harmonic orders of $n = 4k + 1$.

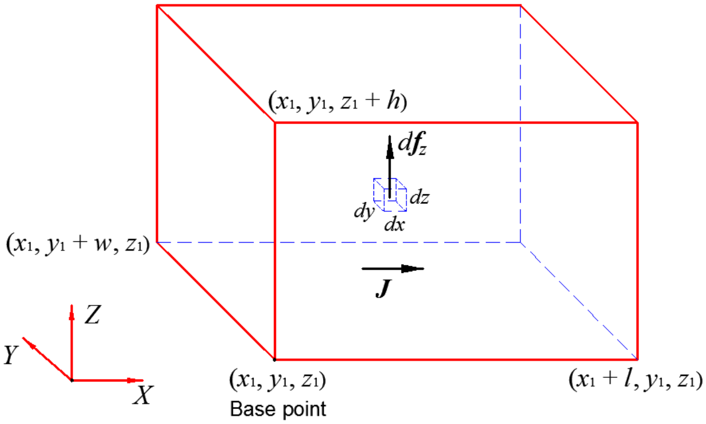

Fig. 2-8 A right-rectangular-prism coil side for the volume integration in the force calculation.

The Lorentz force f_z generated by the y-direction magnetic-flux density in (2.1) is calculated. The Lorentz force acting on the incremental volume of $dxdydz$ of the coil is

$$d\boldsymbol{f}_z = (Jdydzdx\boldsymbol{e}_x) \times \left(B_y\boldsymbol{e}_y\right) = JB_ydydzdx\boldsymbol{e}_z, \tag{2.4}$$

where J (A/m^2) is the current density along the x-direction in the coil. $\boldsymbol{e}_x$, $\boldsymbol{e}_y$, and $\boldsymbol{e}_z$ are the unit vectors in the x-, y-, and z-axes, respectively. The z-direction Lorentz force acting on a right-rectangular parallel prism having the base point of (x_1, y_1, z_1) with dimensions of l in x, w in y, and h in z, is calculated as

$$f_{lwh,z} = J\int_{lwh} B_y \, dxdydz =$$

$$J\int_{z_1}^{z_1+h}\int_{y_1}^{y_1+w} \sum_{k=0}^{+\infty} q_n(z)\sin(\gamma_n y)\left(\int_{x_1}^{x_1+l} dx\right)dydz, \tag{2.5}$$

where

$$q_n(z) = (-1)^k c_n(z) = \frac{(-1)^k 2\sqrt{2}\mu_0 M_0}{\pi n}\left(1 - e^{-\gamma_n \Delta}\right)e^{-\gamma_n z}.$$

Using

$$\int_{z_1}^{z_1+h} \frac{q_n(z)}{\gamma_n} dz = \frac{1}{\gamma_n^2} q_n(z_1)\left(1 - e^{-\gamma_n h}\right),$$

we have

$$f_{lwh,z} = Jl\sum_{k=0}^{+\infty}\frac{2}{\gamma_n^2}q_n(z_1)\sin\left[\gamma_n\left(y_1+\frac{w}{2}\right)\right]\sin\left(\frac{\gamma_n w}{2}\right)\left(1-e^{-\gamma_n h}\right). \tag{2.6}$$

In a similar way, the *y*-direction Lorentz force acting on the same right-rectangular prism is calculated as

$$f_{lwh,y} = -Jl\sum_{k=0}^{+\infty}\frac{2}{\gamma_n^2}q_n(z_1)\cos\left[\gamma_n\left(y_1+\frac{w}{2}\right)\right]\sin\left(\frac{\gamma_n w}{2}\right)\left(1-e^{-\gamma_n h}\right). \tag{2.7}$$

2.2.3 Lorentz Force Generated by a Single Coil

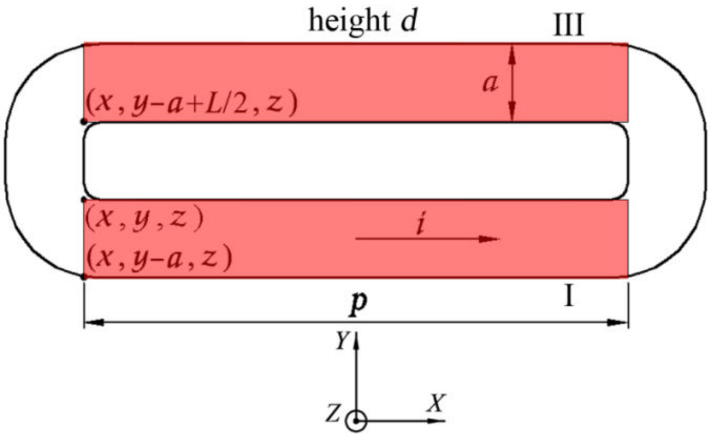

Fig. 2-9 Two coil sides with the base points for force calculation [75].

In case the size of the coil along the *x*-direction is smaller than that of the magnet array, neglecting the effects of the four coil corners, the two shorter coil sides with the *y*- and *z*-direction magnetic-flux densities only generate the forces in *x*. Because the currents flowing in the two shorter coil sides have the same magnitude and are in the opposite directions, two *x*-direction electromagnetic forces acting on the shorter coil sides cancel out. The shaded rectangular regions in Fig. 2-9 illustrate two longer coil sides that are useful for force generation. The point (*x*, *y*, *z*) is the reference point for the force computation of the coil; *z* is the gap between the top surface of the magnet array and the bottom surface of the coil.

The base points to calculate the Lorentz force acting on the right-rectangular-prism coil sides I and III as in Fig. 2-9 are, respectively, $(x, y - a, z)$ and $(x, y - a + L/2, z)$. Using the results of the force calculation from Section 2.2.2 and noting that $\sin\left[\gamma_n\left(y - \frac{a}{2} + \frac{L}{2}\right)\right] = -\sin\left[\gamma_n\left(y - \frac{a}{2}\right)\right]$ with n odd, the Lorentz forces acting on the coil are as follows.

$$f_{coil,z} = Jp \sum_{k=0}^{+\infty} \frac{4}{\gamma_n^2} q_n(z) \sin\left[\gamma_n\left(y - \frac{a}{2}\right)\right] \sin\left(\frac{\gamma_n a}{2}\right)\left(1 - e^{-\gamma_n d}\right) \tag{2.8}$$

$$f_{coil,y} = -Jp \sum_{k=0}^{+\infty} \frac{4}{\gamma_n^2} q_n(z) \cos\left[\gamma_n\left(y - \frac{a}{2}\right)\right] \sin\left(\frac{\gamma_n a}{2}\right)\left(1 - e^{-\gamma_n d}\right) \tag{2.9}$$

It is assumed that the position of the coil in the vertical direction is not changed. When the coil moves along the y-axis, the amplitudes of the force components in (2.8) and (2.9) associated with the harmonics of $n = 5$, $n = 9$, and $n > 9$ are negligible compared with that of $n = 1$. For example, with $\Delta = 12.7$ mm, $z = 2$ mm, $p = 42.29$ mm, $a = 9.65$ mm, and $d = 2.54$ mm, the ratios between the force amplitudes with the 5th and 9th harmonics and that of the fundamental harmonics are 0.3% and 0.1%, respectively. Therefore, to simplify the force-current relation for the purpose of controller design and real-time implementation, it is reasonable to neglect all the force components associated with the harmonics order higher than 1. The simplified force calculations are given as follows.

$$f_{coil,z} = Jp \frac{4}{\gamma_1^2} c_1(z) \sin\left[\gamma_1\left(y - \frac{a}{2}\right)\right] \sin\left(\frac{\gamma_1 a}{2}\right)\left(1 - e^{-\gamma_1 d}\right) \tag{2.10}$$

$$f_{coil,y} = -Jp \frac{4}{\gamma_1^2} c_1(z) \cos\left[\gamma_1\left(y - \frac{a}{2}\right)\right] \sin\left(\frac{\gamma_1 a}{2}\right)\left(1 - e^{-\gamma_1 d}\right) \tag{2.11}$$

2.2.4 Force-Current Transformation for a Two-Coil Forcer

In Fig. 2-10, the two coils of a forcer are separated by a distance of $3L/4$ along the y-axis. This corresponds to a phase difference of 270°. With only the fundamental component being considered, the z- and y-direction Lorentz forces acting on Coil 1 are, respectively

$$F_{1,z} = J_1 p c_1(z) \frac{4}{\gamma_1^2} \sin\left[\gamma_1 \left(y - \frac{a}{2}\right)\right] \sin\left(\frac{\gamma_1 a}{2}\right)(1 - e^{-\gamma_1 d}) \tag{2.12}$$

$$F_{1,y} = -J_1 p c_1(z) \frac{4}{\gamma_1^2} \cos\left[\gamma_1 \left(y - \frac{a}{2}\right)\right] \sin\left(\frac{\gamma_1 a}{2}\right)(1 - e^{-\gamma_1 d}), \tag{2.13}$$

where J_1 is the current density in Coil 1. The z- and y-direction electromagnetic forces acting on Coil 2 are derived by replacing y in (2.12) and (2.13) by $y + 3L/4$ and J_1 by J_2, the current density in Coil 2.

$$F_{2,z} = -J_2 p c_1(z) \frac{4}{\gamma_1^2} \cos\left[\gamma_1 \left(y - \frac{a}{2}\right)\right] \sin\left(\frac{\gamma_1 a}{2}\right)(1 - e^{-\gamma_1 d}) \tag{2.14}$$

$$F_{2,y} = -J_2 p c_1(z) \frac{4}{\gamma_1^2} \sin\left[\gamma_1 \left(y - \frac{a}{2}\right)\right] \sin\left(\frac{\gamma_1 a}{2}\right)(1 - e^{-\gamma_1 d}) \tag{2.15}$$

The resultant forces acting on the 2-coil forcer are

$$F_{12,z} = b_1(z)\left\{J_1 \sin\left[\gamma_1 \left(y - \frac{a}{2}\right)\right] - J_2 \cos\left[\gamma_1 \left(y - \frac{a}{2}\right)\right]\right\} \tag{2.16}$$

$$F_{12,y} = b_1(z)\left\{-J_1 \cos\left[\gamma_1 \left(y - \frac{a}{2}\right)\right] - J_2 \sin\left[\gamma_1 \left(y - \frac{a}{2}\right)\right]\right\}, \tag{2.17}$$

where

$$b_1(z) = p c_1(z) \frac{4}{\gamma_1^2} \sin\left(\frac{\gamma_1 a}{2}\right)(1 - e^{-\gamma_1 d}).$$

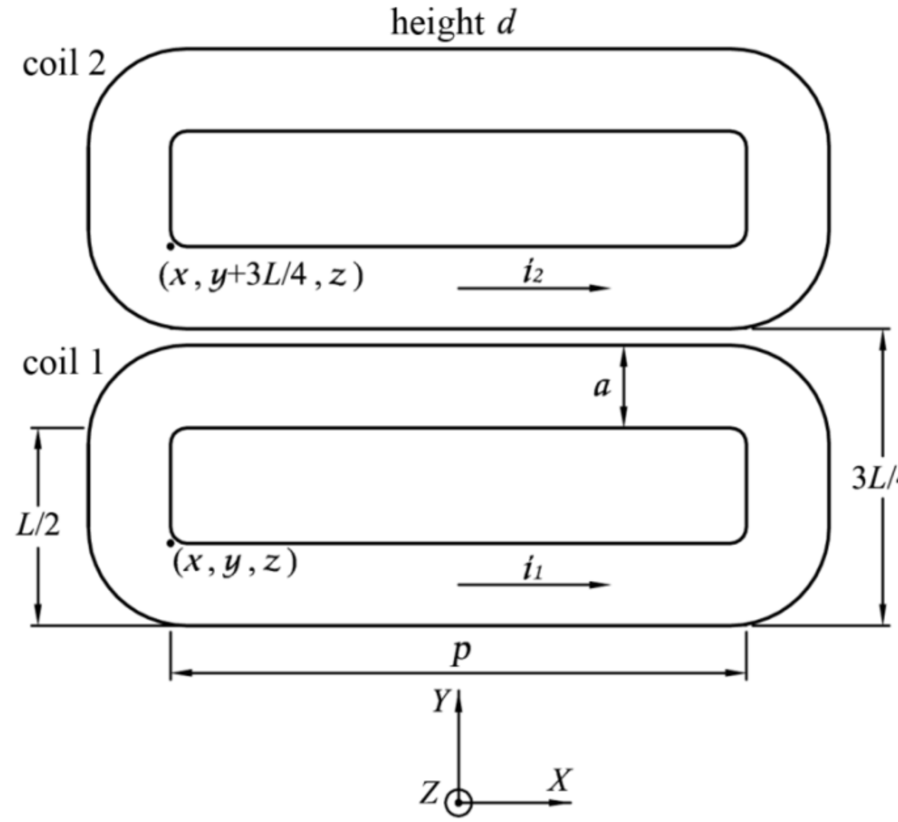

Fig. 2-10 Illustration of two coils with a phase difference of 270° [75].

In case the two coils of a forcer are overlapped with one side of each coil being in the middle of the two sides of the other coil, the coils are separated by $L/4$ along the y-axis and have a phase difference of 90°. With (x, y, z) and $(x, y+L/4, z)$ being the base points of Coils 1 and 2, respectively, the Lorentz forces acting on Coil 2 are given by replacing y in (2.12) and (2.13) with $y + L/4$ and the current density J_1 by J_2.

$$F_{2,z} = J_2 p c_1(z) \frac{4}{\gamma_1^2} \cos\left[\gamma_1 \left(y - \frac{a}{2}\right)\right] \sin\left(\frac{\gamma_1 a}{2}\right) (1 - e^{-\gamma_1 d}) \tag{2.18}$$

$$F_{2,y} = J_2 p c_1(z) \frac{4}{\gamma_1^2} \sin\left[\gamma_1 \left(y - \frac{a}{2}\right)\right] \sin\left(\frac{\gamma_1 a}{2}\right) (1 - e^{-\gamma_1 d}) \tag{2.19}$$

The resultant forces acting on the two overlapping coils with a 90° phase difference are

$$F_{12,z} = b_1(z)\left\{J_1 \sin\left[\gamma_1\left(y - \frac{a}{2}\right)\right] + J_2 \cos\left[\gamma_1\left(y - \frac{a}{2}\right)\right]\right\} \tag{2.20}$$

$$F_{12,y} = b_1(z)\left\{-J_1 \cos\left[\gamma_1\left(y - \frac{a}{2}\right)\right] + J_2 \sin\left[\gamma_1\left(y - \frac{a}{2}\right)\right]\right\} \tag{2.21}$$

For a moving-coil planar stage with the gap between the magnet array and the coils varying in a small range, $b_1(z)$ in (2.16–17), and (2.20–21) can be fixed as a constant b_1 corresponding to the nominal air gap. In this case, the linear force-current relation is dependent only on the position in y. Although the force model is approximated with a nominal air gap, the mover's position in z can still be controlled precisely by a feedback controller. This is demonstrated in Chapter IV.

2.2.5 Finite-Element-Method Verification of the Force Calculation

A 2D finite element method (FEM) is applied to verify the correctness and accuracy of the force calculation derived above. In the case considered here, the Lorentz forces in the y- and z-directions generated by a forcer having two overlapping coils with a 90° phase difference are obtained by an FEM and the analytical solution derived in Section 2.2.4. The geometrical parameters in Fig. 2-10 are given as $\Delta = 12.7$ mm, $z = 2$ mm, $p = 42.29$ mm, $a = 9.65$ mm, and $d = 2.54$ mm. The two-coil forcer considered herein is different from the one in Fig. 2-10 only in the distance between the two coils, $L/4$ instead of $3L/4$. The permanent magnets are NdFeB 35. The currents densities in the coils are $J_1 = J_2 = 4 \times 10^6$ A/m^2. The end effects of the magnets and the shorter coil sides are neglected. This negligence is reasonable for two cases: (1) the effective coil sides are longer than the magnet bars, and the length of each magnet bar in the *x*-direction is relatively larger than its dimensions in *y* and *z*, and (2) as in the experiment of this work, the magnet bars are longer than the effective coil sides, and the shorter coil sides are made to be farther away from the magnets than the effective coil sides are.

Figures 2-11–2-12 show the flux lines and the magnetic flux density plotted from an FEM at the same position of the set of coils above the magnet array. In Fig. 2-13, the *y*-direction forces obtained analytically and by an FEM are plotted in a spatial pitch in *y* of the Halbach magnet array. The error between the results from the FEM and the analytical solution stays within only 1% of the peak-to-peak force amplitude.

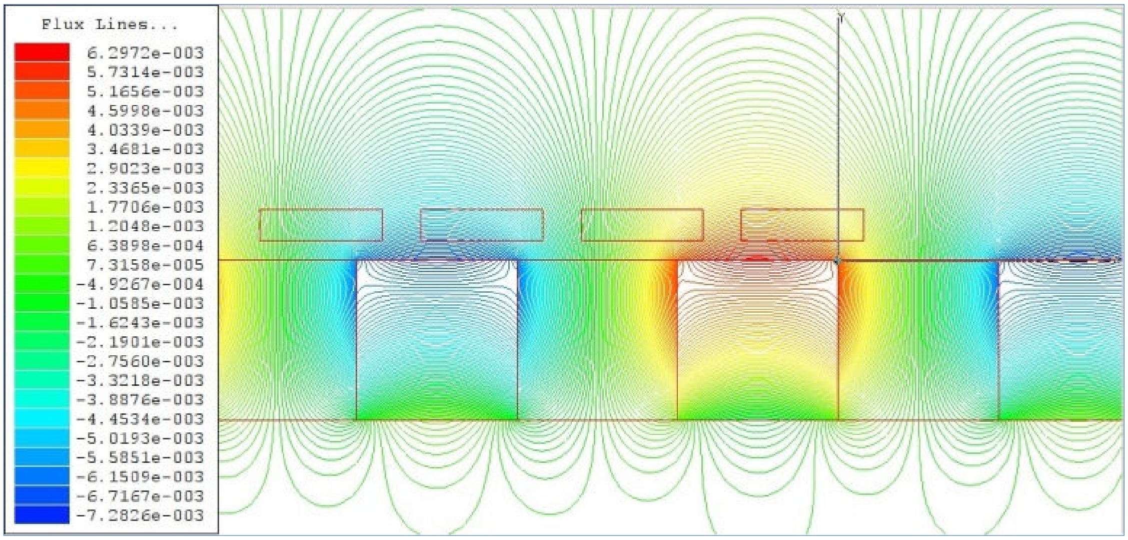

Fig. 2-11 An FEM image of the flux lines generated by a linear Halbach magnet array [75].

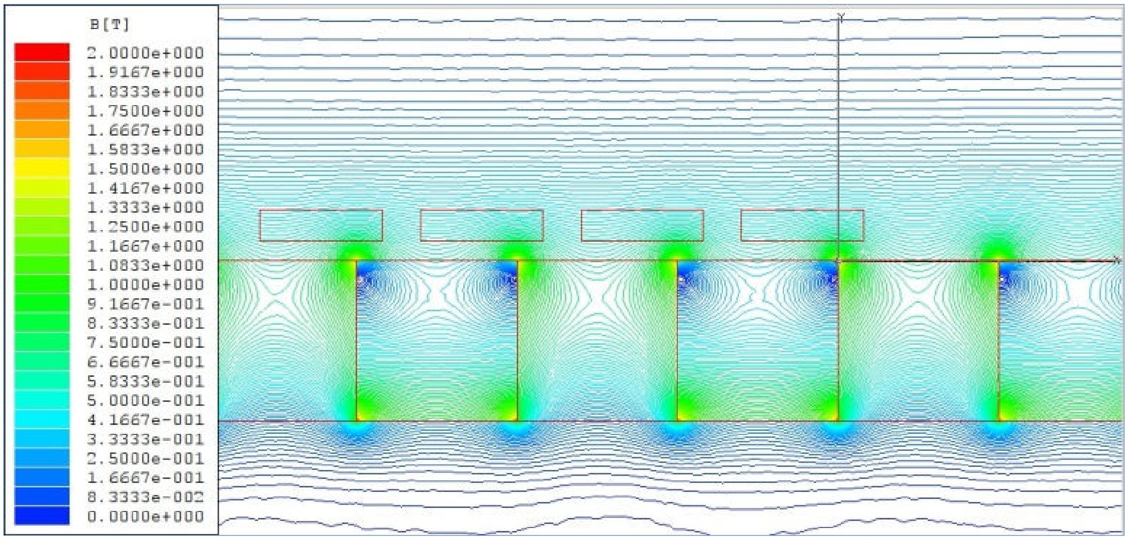

Fig. 2-12 An FEM image of the flux density generated by a linear Halbach array [75].

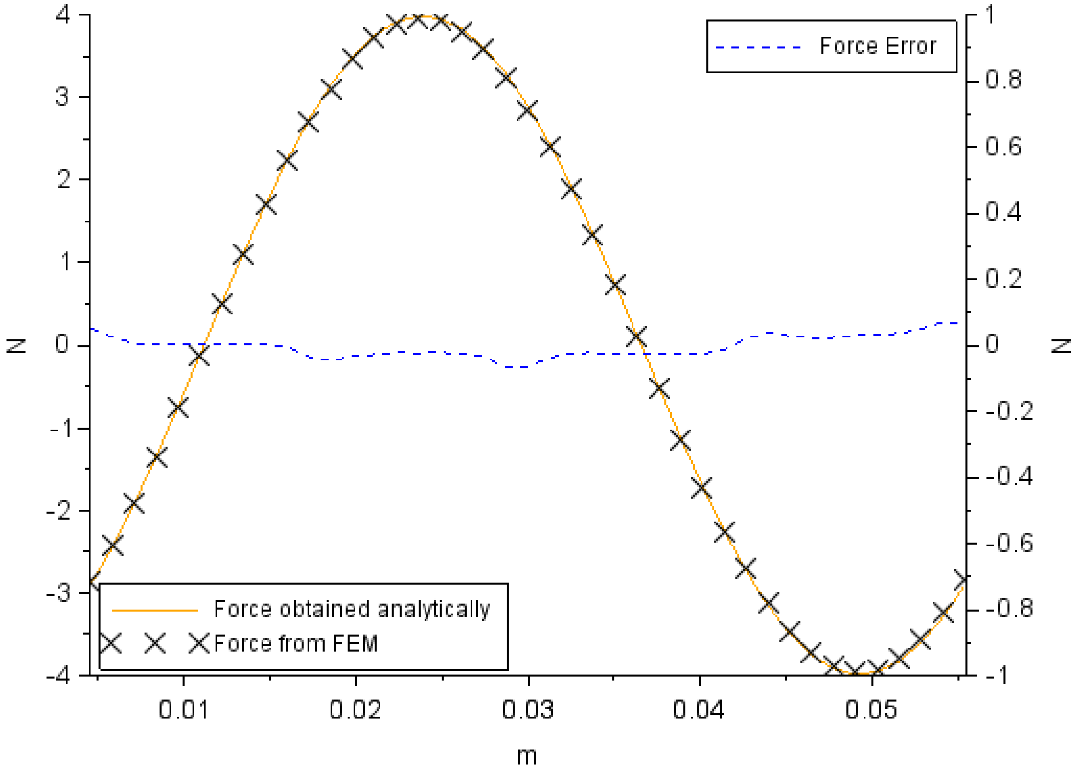

Fig. 2-13 Plots of the force from the FEM compared with that of the analytical calculation [75].

CHAPTER III

DEVELOPMENT OF A 6-DOF MAGLEV POSITIONING STAGE*

3.1 The Superimposed Halbach Magnet Matrix

3.1.1 Structure of the Superimposed Halbach Magnet Matrix

A linear Halbach magnet array as shown in Fig. 2-6, being denoted as the *yz* magnet array, generates the magnetic flux-density components in both the *y*- and *z*-directions. A rectangular planar coil, which is placed on the strong side of the magnet array and has the coil sides parallel with the array's edges, produces a zero resultant force in *x*. For a planar stage that can perform in-plane motions in *x* and *y*, at least one *yz* and one *xz* linear Halbach arrays are needed.

Kim introduced the concentrated-field magnet matrix by superimposing a *yz* linear Halbach magnet array and an *xz* one [1, 70]. The fundamental element of a *yz* or *xz* magnet array is the right-rectangular-prism magnet bar as in Figs. 1-6 and 2-3. For the superimposed magnet matrix, fundamental elements are cubic magnet blocks with different magnetization directions and magnetic remanence. Figure 3-1 presents a top view of the strong side's surface of the superimposed Halbach magnet matrix with four

---

*Part of this chapter is reprinted with permission from "A Two-Phase Framework for Linear Permanent-Magnet Machines and Multi-Axis Stages with Magnetic Levitation" by V. H. Nguyen and W.-J. Kim, in *Proc. 2014 ASME Dynamic Systems and Control* Conference, No. 5936, Oct. 2014, Copyright [2014] by ASME Publishing.

spatial pitches along each side. The magnet blocks denoted by a letter N and S have the magnetization vector pointing in the positive and negative z-direction, respectively. Magnet blocks with an arrow parallel to the x or y-axis and pointing to N and away from S have the magnetization vector directed 45° with respect to the positive and negative z-direction, respectively. The magnetization direction of magnet blocks marked with a diagonal arrow is the same as the arrow's direction in the horizontal plane. Theoretically, the magnet blocks denoted by N and S have the remanence $\sqrt{2}$ times stronger than that of the magnets marked with an arrow.

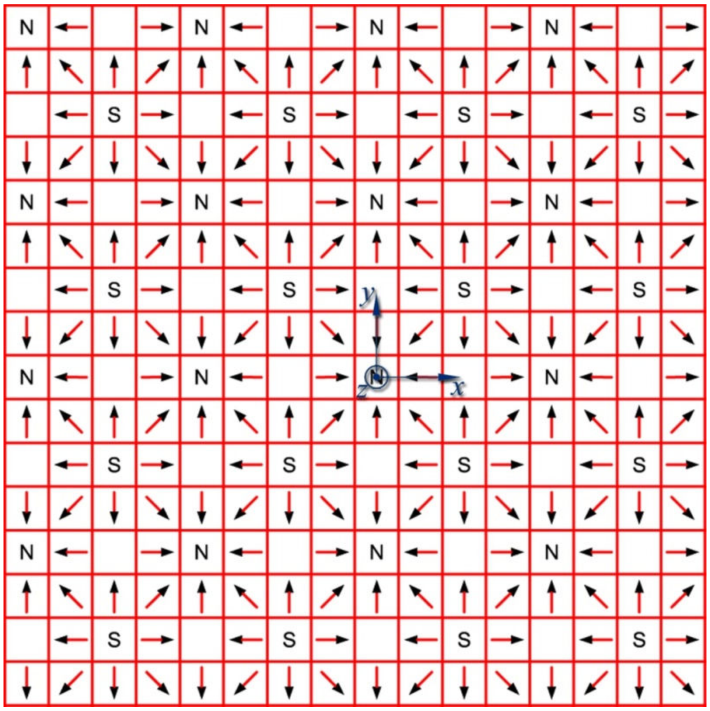

Fig. 3-1 Illustration of the superimposed magnet matrix's structure [75].

The superimposed magnet matrix used in this work has 6 spatial pitches in x and y. Figure 3-2 is a photograph showing the assembly of the magnet matrix. The spatial pitch of the yz and xz magnet arrays is L = 0.0508 m. The strong magnets are NdFeB50 with the magnetic remanence of 1.43 T. The weak magnets are NdFeB30 with the remanance of 1.10 T. The thickness of the magnet matrix is $h = 12.7 \times 10^{-3}$ m. On the top surface of the magnet matrix, there are an epoxy layer of 0.51 mm and a mirror-finished aluminum plate with the thickness of 0.81 mm [70]. The aluminum plate having the surface flatness of 0.1 μm is to reflect the laser beams of the vertical laser displacement sensors.

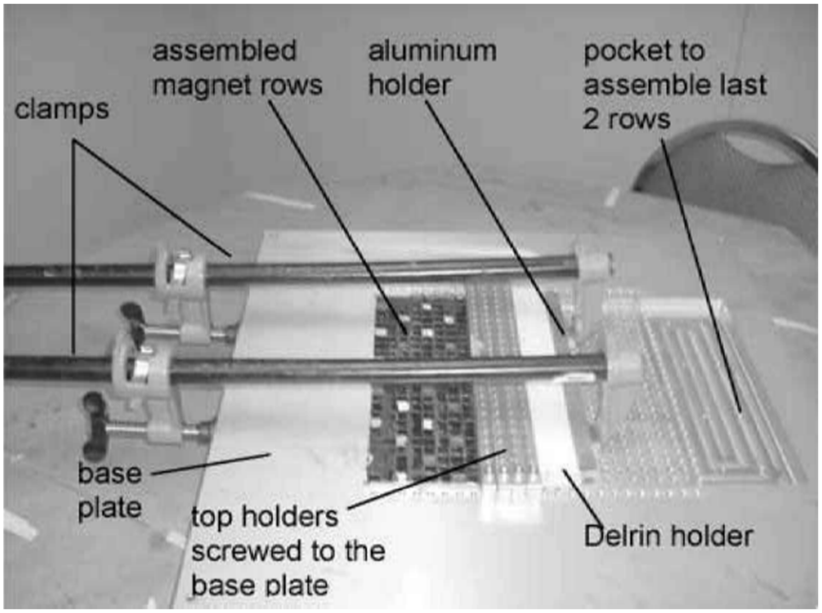

Fig. 3-2 A photograph taken during the process of making the magnet matrix [70].

3.1.2 The Field Solution and Force-Generation Considerations

The superimposed magnet matrix's field solution for the flux-density component in y and x is that of the yz and xz magnet array, respectively. The field solution for the flux-density component in z of the magnet matrix is the superposition of those from the yz and xz arrays.

By utilizing this structure of the magnet matrix, Lorentz coils can be arranged in a compact moving part that has forces generated in both *x*- and *y*-directions. Regarding the Lorentz force calculation in (2.9), (2.11), (2.13), (2.15), and (2.19), there are *y*-direction Lorentz forces acting on the coil sides I and III due to the *z*-direction magnetic flux density generated by the *xz* Halbach array. However, these two *y*-direction forces cancel out because the *z*-direction flux-density components in the two coil sides are equal and the same electric current flows in the two coil sides in the opposite directions. These equations, therefore, still work with the superimposed magnet matrix.

3.2 The Pair of Two Overlapping Coils

3.2.1 Why Overlapping Coils?

With air core and small coil inductance, the two coils in a forcer are made to be overlapped to save the space and weight for the moving platen. In the set of two coils forming a forcer, a longer side of each coil occupies the space between the two longer sides of the other coil. By doing this, the two coils are separated by a 90° phase difference. The shorter sides of each coil are curved to be farther away from the magnets to reduce the end effects of the coils, simplify the force calculation, and improve the model accuracy of the system. The cost to pay is the time to manually wind the coils.

3.2.2 Coil Tooling and Fabrication

The tooling to make the pairs of two overlapped coils is shown in Fig. 3-3. The top surface of the coils in Fig. 3-3(a) is to be placed in parallel and close to the top surface of the Halbach magnet matrix. Both the upper part in Fig. 3-3(b) and the coil housing in Fig. 3-3(a) are made of aluminum by vertical milling. AWG 20 heavy-build bondable copper wire was used to fabricate the coil. After the first layer of the coil on the left is finished, the first layer of the other coil on the right is wound, and then the second layer of the coil on the left is wound. After an equal number of layers of the two coils were wound, the upper part of the tooling shown in Fig. 3-3(b) and the housing shown in Fig. 3-3(a) are clamped to press the coils down, improving the coils' rigidity and thickness uniformity. Alcohol is used as the solvent to melt the bonding material and make coil turns glued to each other. The coils are baked at 250°F for 12 minutes and then left intact for 8 hours.

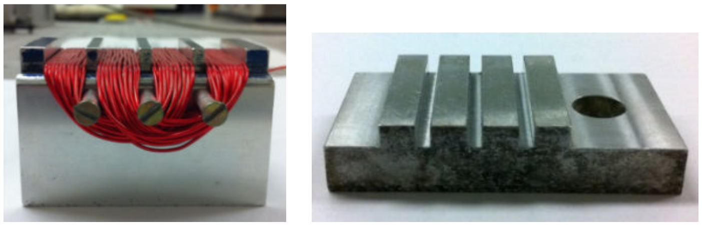

(a) (b)

Fig. 3-3 Photographs of (a) a pair of overlapped coils in the housing after being wound and set and (b) the upper part of the tooling [75].

Each coil side has $N = 30$ turns stacked in three layers. The thickness, width, and effective length useful for force generation of each coil side are $d = 2.54$ mm, $a = 9.65$ mm, and $p = 42.29$ mm, respectively. The adjacent sides of two overlapping coils are separated by 12.7 mm, a quarter of one spatial pitch of the magnet arrays. The resistance and the inductance of a coil are 0.19 Ω and 59 μH, respectively. A pair of two coils weighs 51.3 g. Figure 3-4 is a set of engineering drawings of the coil tooling.

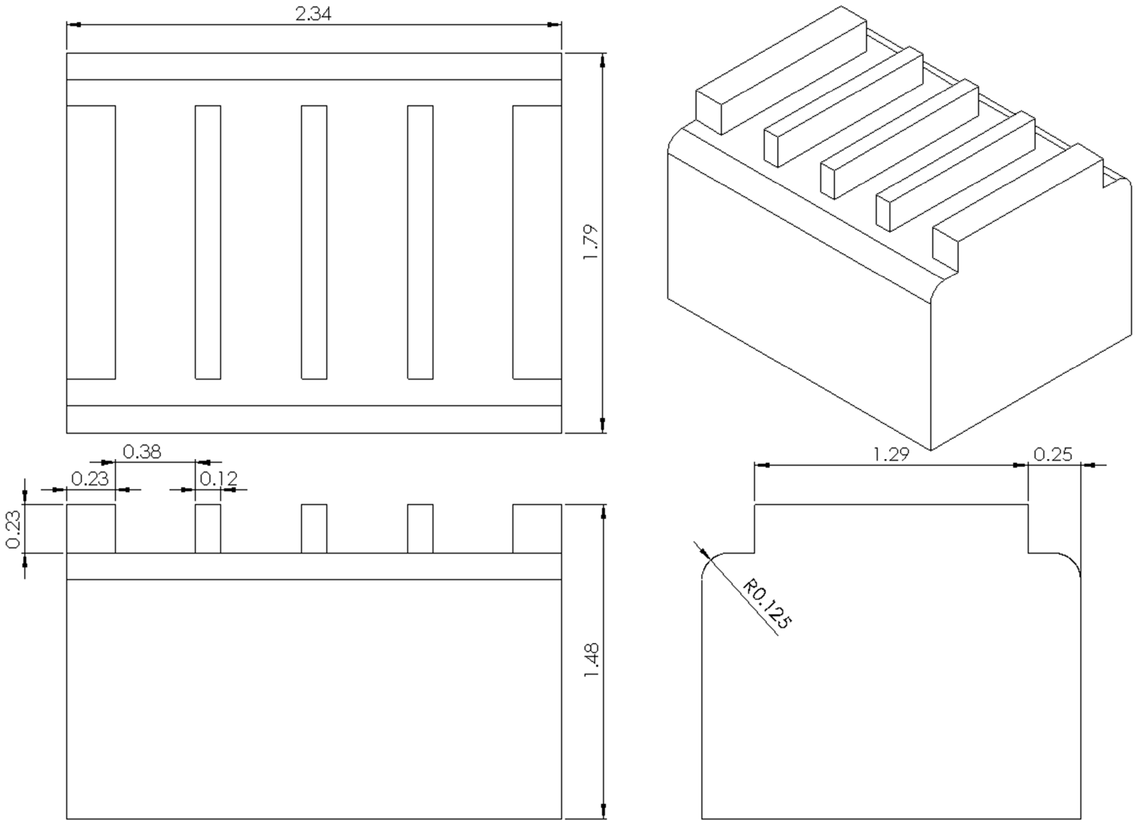

Fig. 3-4 Engineering drawing of the coil tooling.

3.3 The Compact Single-Part Moving Platen with 4 Overlapped Coils

3.3.1 Overview of the Moving Platen's Mechanical Design

The 2-phase framework discussed in Section 2.2 is validated by a newly developed 6-DOF maglev stage. The moving part is a compact frame carrying Lorentz coils and the stationary part is the above-mentioned concentrated-field Halbach magnet matrix. The coil arrangement in the moving part is shown in Fig. 3-5. The shorter coil sides are illustrated by the dashed lines in Fig. 3-5(a). Figure 3-5(b) is a photograph of the moving platen without the precision mirrors placed on top of the magnet matrix.

The key in the arrangement of the coil pairs on the moving platen is that the number of forcers contributing to the force allocation for each axis is minimized. This simplifies the relation between 6 resultant forces (3 for in-plane motions and 3 for out-of-plane motions) and the currents flowing in the coils on the platen. Moreover, each forcer participating in the dynamics of a less number of axes implies that the coupled dynamics among axes are reduced. With the four forcers arranged in a cross configuration as in Fig. 3-5(a), each axis can be fully actuated by only two forcers, except for the z-axis translational motion. Each of the coil pairs 1&2 and 5&6 generates the forces in the x- and z-directions. Each of the coil pairs 3&4 and 7&8 generates the forces in the y- and z-directions. Only forcers 1&2 and 5&6 are needed for the x-direction translation and the rotation about the X'-axis. Only forcers 3&4 and 7&8 are needed for the y-direction translation and the rotation about the Y'-axis.

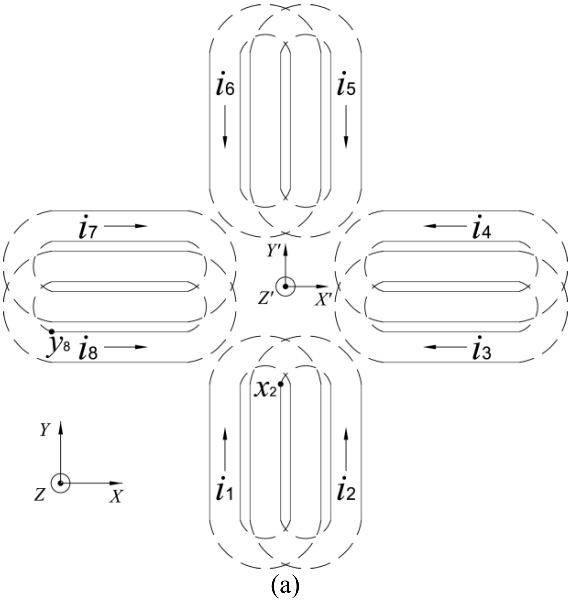

(a)

Fig. 3-5 (a) The cross configuration of the 4 pairs of coils with the current-direction convention and (b) a photograph of the assembled platen on top of the magnet matrix without the precision mirrors [75].

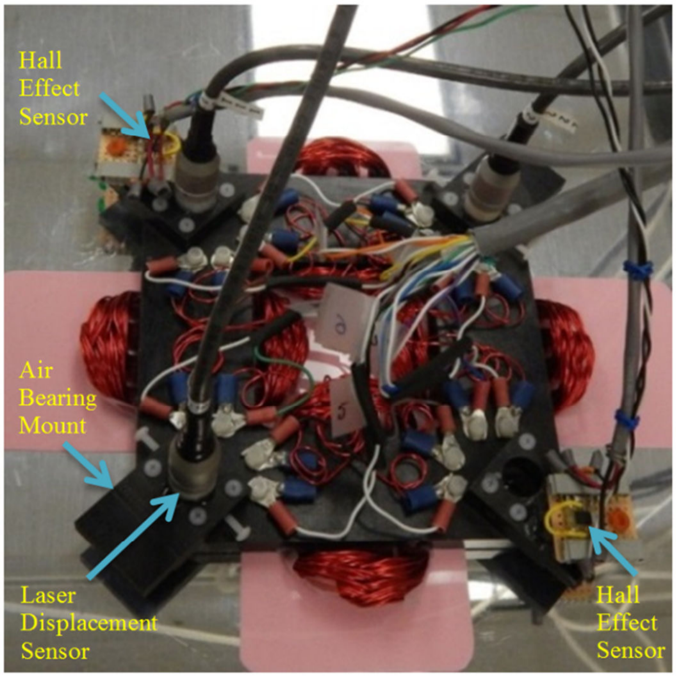

(b)
Fig. 3-5 Continued.

Except for the sensors and the coils, the moving platen has only a square frame and four other identical parts. In Fig. 3-5(b), the four rectangular parts fixed to the frame's corners have dual functions, being the sensor mounts and the air bearing supports. The frame and the sensor mounts are made of Delrin Acetal Resin, an easy-machinability plastic material with high tensile strength (62.05–75.84 MPa) and low mass density (1.41 g/cm^3) [76]. Three laser displacement sensors, NanoGage proximity sensors manufactured by OPTRA Inc.[3], are used for out-of-plane positioning. Two 2-channel Hall-effect sensors, which are Sentron[4] 2SA-10G-SO, are used to initialize the position of the platen with the laser interferometers. Figure 3-6 is an engineering

---

[3] OPTRA Inc., 461 Boston Street Suite E6, Topsfield MA 01983-1234, U.S.A
[4] Sentron AG, Baarerstrasse 73 CH-6300 Zug, Switzerland

drawing of the moving platen's frame with four air bearing supports and sensor mounts at its corners.

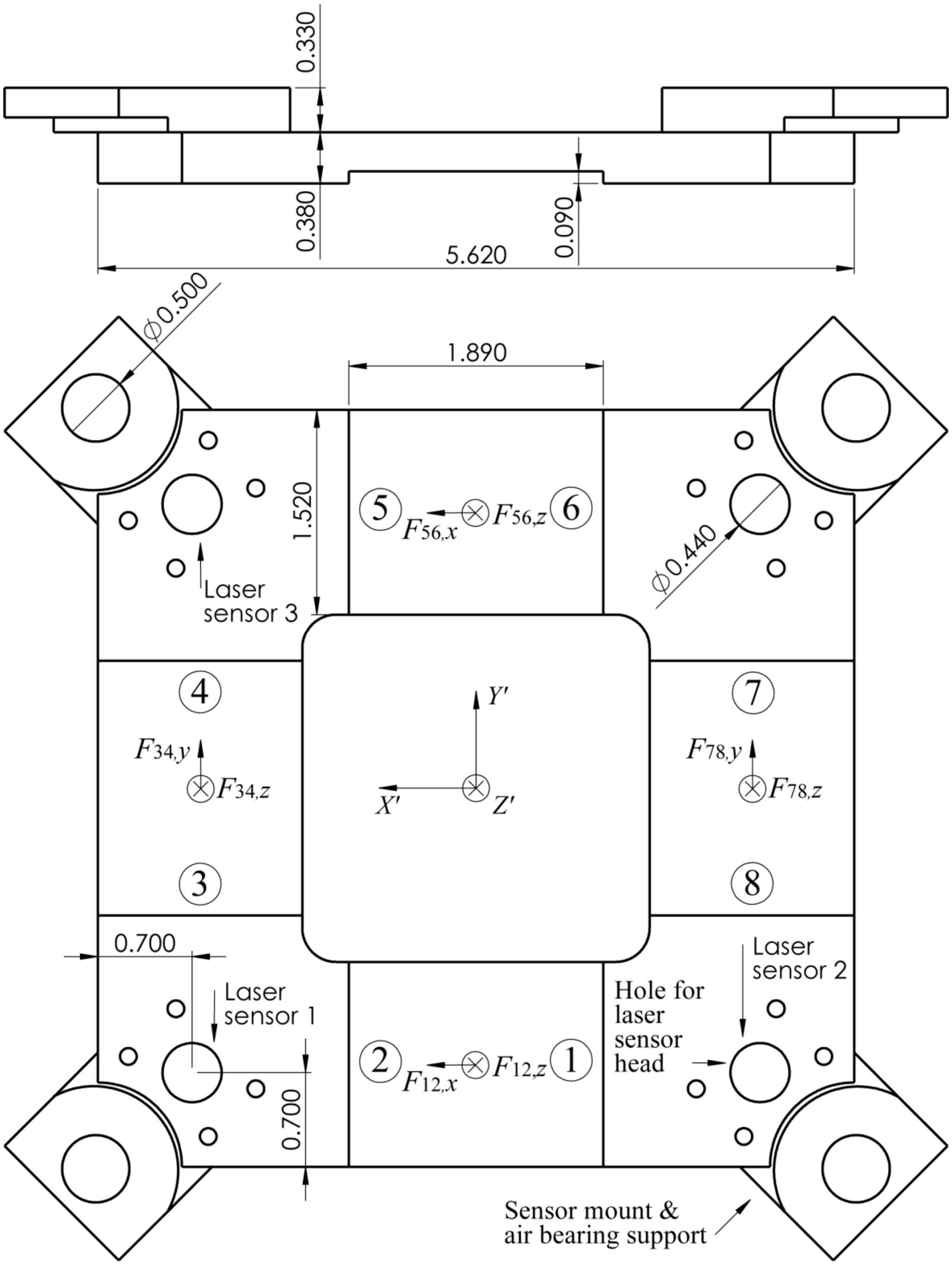

Fig. 3-6 Engineering drawing of the side view and bottom view of the moving platen's frame with the sensor mounts. Unit: Inch.

3.3.2 Mechanical Components and Parts

Figure 3-7 is a 3-D rendering of the Delrin plastic frame of the moving platen. It has a square shape trimmed at the four corners so that the air bearings can be placed there. The square holes in the center of the part are to reduce the mass of the moving part and to allow for the placement of the four pairs of coils with the shorter coil sides bent up. To reduce the total number of parts in the moving platen and to save the room for the four coils to be assembled, the air bearing supports are designed to have the function of the sensor mounts. The larger round holes in the frame body shown in Fig. 3-7 are to house the cylindrical-shape laser displacement sensors to measure the platen's position in the vertical direction and in the out-of-plane rotations. The smaller round holes are tapped to fit the 4-40 screws in order to fix the sensor mounts to the frame. The four rectangular spaces in the bottom of the frame's sides are to assemble the coils. The frame is machined with a 3-axis vertical milling machine.

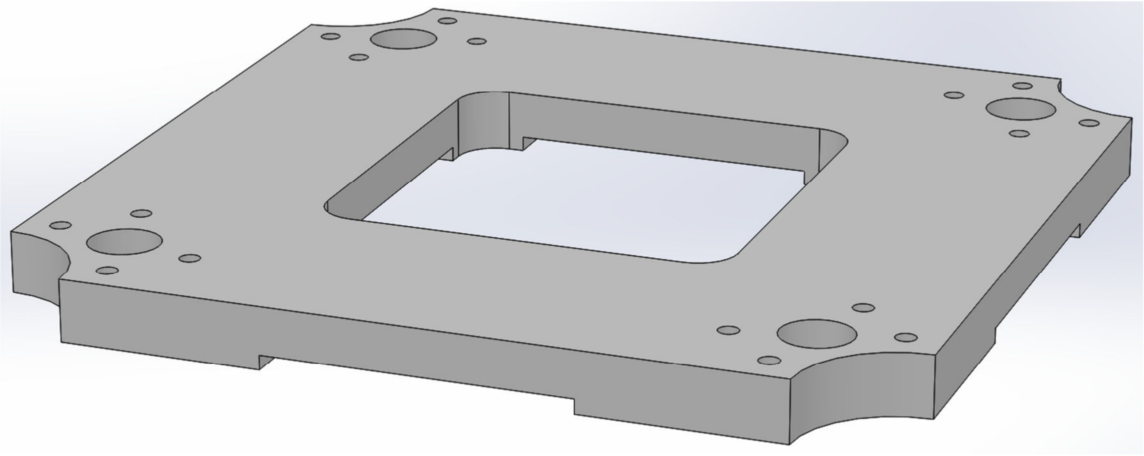

Fig. 3-7 A 3D rendering of the moving platen's plastic frame.

The sensor mounts/air bearing supports are machined by a vertical milling machine. Figure 3-8 is an engineering drawing of the part with two side views, a bottom-up view, and a perspective view. In the bottom-up view in the bottom right corner of Fig. 3-8, the space on the left with the boundary surface having the diameter of 0.625 in is to house a cylindrical air bearing. The air bearings used herein are FP-C-010 round flat pad air bearings manufactured by Nelson Air Corporation[5]. The round hole on the right, which has the diameter of 0.562 in, is to assemble the vertical laser displacement sensor.

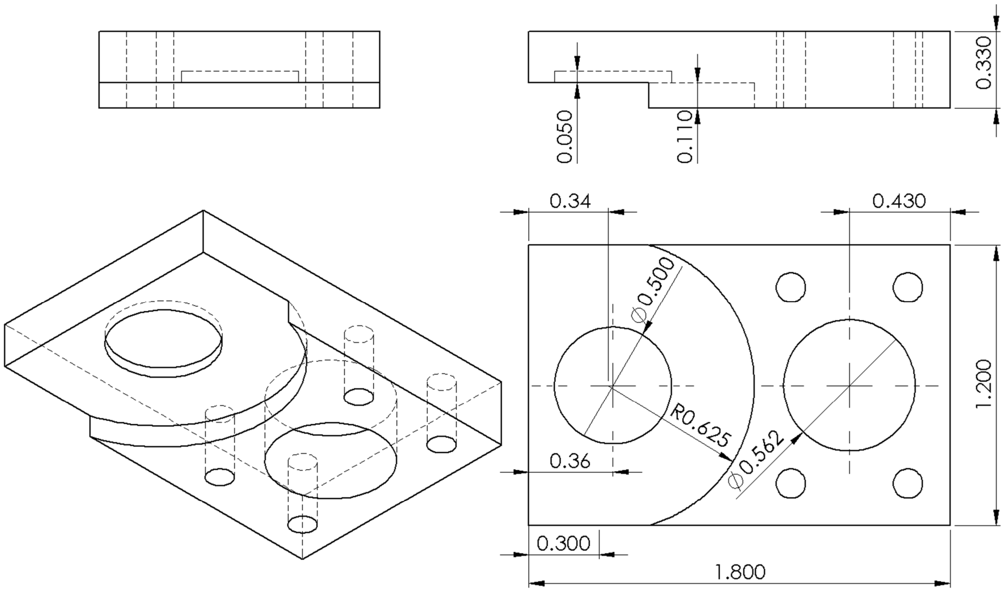

Fig. 3-8 An engineering drawing with multiple views of the sensor mount/air bearing support. Unit: Inch.

The air bearing supports are designed to do the function of the sensor mounts and to guarantee a uniform distance of 1.6 mm between the bottom surface of the coils and the top surface of the magnet matrix. The Hall-effect sensors to measure the magnetic flux densities generated by the magnet matrix need to be located at a certain height

---

[5] Nelson Air Corp., 559 Route 13 South, PO Box 2 Milford, NH 03055, U.S.A

where the flux density falls well in the range from –40 mT to 40 mT. Figure 3-9 gives the dimensions of the aerostatic bearings used in this design.

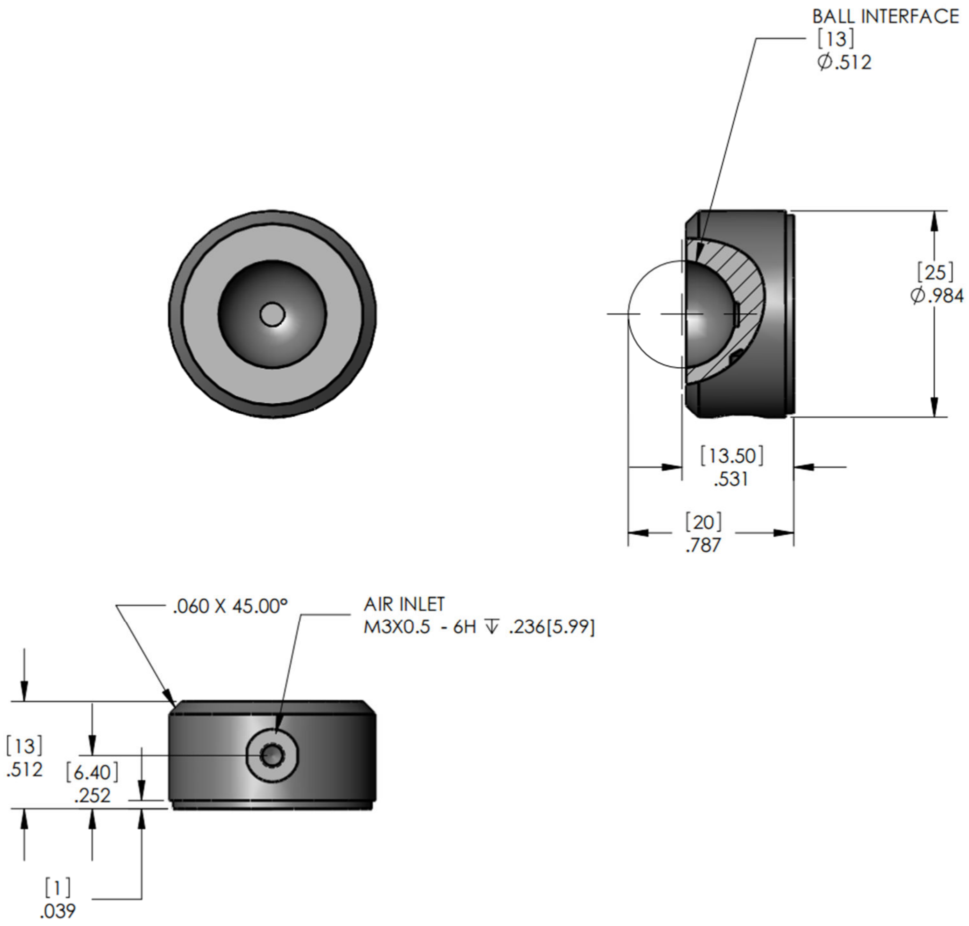

Fig. 3-9 Engineering drawings of the FP-C-010 round flat pad air bearings manufactured by Nelson Air Corp. The unit is inch (mm in the bracket) [77].

Three laser displacement sensors manufactured by OPTRA Inc. are used to measure the platen's position in the vertical axis and in the out-of-plane rotations. A photograph of the sensor is given in Fig. 3-10. The total length of the sensor body is 2.310 inch and the maximum body diameter is 0.623 inch.

Fig. 3-10 Photograph of the Nanogage 100 laser displacement sensor [78].

3.3.3 Mechanical Assembly of the Moving Platen

The coils are fixed to the flat rectangular spaces in the bottom of the four sides of the platen's frame. Loctile[6] super glue is used. Each sensor mounts are assembled to the frame by four 4-40 nylon screws through the holes as in Figs. 3-7–3-8. The sensors are assembled to the platen's frame by fitting their cylindrical heads to the 0.440 inch holes shown in Figs. 3-6–3-7. In order to guarantee a standoff of 3.0 mm between the sensor head's surface to the mirror-finished aluminum plate on top of the magnet matrix, plastic shims with precise thickness are placed between the bottom surface of the sensor mounts and the top surface of the platen's frame.

The size of the Delrin frame of the moving part is 142.5 mm × 142.5 mm. The total height of the frame and the sensor mounts without the sensors is 18.03 mm. The total mass of the fully assembled moving part is $m = 0.75$ kg. The moments of inertia of the moving part with respect to the X'-, Y'-, and Z'-axes, as in Fig. 3-6, are estimated to be $I_x = I_y = 0.0019$ kg-m^2, and $I_z = 0.0036$ kg-m^2, respectively.

---

[6] Loctite Brand - Consumer Products, 26235 First Street Westlake Ohio 44145, U.S.A

3.4 Modeling of the 6-DOF Positioning Stage

With the moving part considered a pure mass, its equations of motion are derived from the Newtonian dynamics.

$$m\ddot{x} = F_x, m\ddot{y} = F_y, I_z\ddot{\theta}_z = T_z \tag{3.1}$$

$$m\ddot{z} = F_z, I_x\ddot{\theta}_x = T_x, I_y\ddot{\theta}_y = T_y \tag{3.2}$$

Here, x, y, z, θ_x, θ_y, and θ_z are the position of the moving part in the X-, Y-, and Z-axes and its rotation angles about the X'-, Y'-, and Z'-axes, respectively. The XYZ coordinate frame shown in Fig 3-5(a) is fixed to the magnet matrix and the $X'Y'Z'$ frame in Fig. 3-6 is fixed to the moving part. F_x, F_y, and F_z are the resultant Lorentz forces acting on the platen in X, Y, and Z, respectively. T_x, T_y, and T_z are the resultant torques acting on the platen about the X'-, Y'-, and Z'-axes, respectively, generated by the Lorentz forces acting on the coils. In the targeted applications of this 6-DOF planar stage, the position of the moving platen in z is controlled only to track a constant reference. In order to lift the moving platen up from rest to a certain height, the control effort in z is increased by repeatedly feedforwarding a constant amount until the platen is within an allowable distance from the reference. This is done while the feedback control loops in x, y, and θ_z are closed. After that the feedback loop in z is closed. Therefore, in the first equation of (3.2), the weight of the platen is omitted because it is eventually canceled by a DC control effort.

In Fig. 3-5(a), the base point along the X-axis for force calculation of the forcers 1&2 and 5&6 is x_2. The base point along the Y-axis for force calculation of the forcers 3&4 and 7&8 is y_8. The relation between the resultant magnetic forces and torques acting on the moving platen and the Lorentz forces generated by the four forcers is given as follows. Here, $F_{12,x}$ is the Lorentz force along the x-direction generated by the coil pair 1 and 2. F_x is the resultant Lorentz force acting on the entire moving platen in the x-direction. T_z is the resultant torque acting on the entire moving platen about the Z'-axis generated by $F_{12,x}$, $F_{56,x}$, $F_{34,y}$, and $F_{78,y}$.

$$\begin{bmatrix} F_x \\ F_y \\ T_z \\ F_z \\ T_x \\ T_y \end{bmatrix} = \begin{bmatrix} 1 & 0 & 0 & 0 & 1 & 0 & 0 & 0 \\ 0 & 0 & 1 & 0 & 0 & 0 & 1 & 0 \\ l & 0 & l & 0 & -l & 0 & -l & 0 \\ 0 & 1 & 0 & 1 & 0 & 1 & 0 & 1 \\ 0 & -l & 0 & 0 & 0 & l & 0 & 0 \\ 0 & 0 & 0 & -l & 0 & 0 & 0 & l \end{bmatrix} \begin{bmatrix} F_{12,x} \\ F_{12,z} \\ F_{34,y} \\ F_{34,z} \\ F_{56,x} \\ F_{56,z} \\ F_{78,y} \\ F_{78,z} \end{bmatrix} = A \begin{bmatrix} F_{12,x} \\ F_{12,z} \\ F_{34,y} \\ F_{34,z} \\ F_{56,x} \\ F_{56,z} \\ F_{78,y} \\ F_{78,z} \end{bmatrix} \tag{3.3}$$

Here, $l = 0.05207$ m is the distance from the midpoint of each coil side to the platen's symmetric axis perpendicular to the coil side.

The force-current transformation between the 8 currents flowing in the 8 coils and the 8 force components acting on the forcers is

$$[F_{12,x}\ F_{12,z}\ F_{34,y}\ F_{34,z}\ F_{56,x}\ F_{56,z}\ F_{78,y}\ F_{78,z}]^T =$$

$$b_*(z) \begin{bmatrix} sx & -cx & 0 & 0 & 0 & 0 & 0 & 0 \\ cx & sx & 0 & 0 & 0 & 0 & 0 & 0 \\ 0 & 0 & cy & sy & 0 & 0 & 0 & 0 \\ 0 & 0 & -sy & cy & 0 & 0 & 0 & 0 \\ 0 & 0 & 0 & 0 & cx & -sx & 0 & 0 \\ 0 & 0 & 0 & 0 & -sx & -cx & 0 & 0 \\ 0 & 0 & 0 & 0 & 0 & 0 & -sy & -cy \\ 0 & 0 & 0 & 0 & 0 & 0 & -cy & sy \end{bmatrix} \begin{bmatrix} i_1 \\ i_2 \\ i_3 \\ i_4 \\ i_5 \\ i_6 \\ i_7 \\ i_8 \end{bmatrix}, \tag{3.4}$$

here $sx = \sin(x_2)$, $cx = \cos(x_2)$, $sy = \sin(y_8)$, and $cy = \cos(y_8)$. The current flowing in the coil with the index $j = 1, 2\ldots 8$, is i_j. The function $b_*(z)$ is defined as

$$b_*(z) = \frac{N}{da} b_1(z) = pc_1(z) \frac{4N}{da\gamma_1^2} \sin\left(\frac{\gamma_1 a}{2}\right)(1 - e^{-\gamma_1 d}), \tag{3.5}$$

where $c_1(z)$ is evaluated at the nominal distance of z_0 = 0.0016 m between the top surface of the magnet matrix and the bottom surface of the coils.

From (3.3), to have linear relations between the resultant forces and torques acting on the platen and the control efforts u_x, u_y, $u_{\theta z}$, u_z, $u_{\theta x}$, and $u_{\theta y}$ of the 6 axes, the pseudo-inverse B of the matrix A is computed and used in the relation introduced below.

$$\begin{bmatrix} F_{12,x} \\ F_{12,z} \\ F_{34,y} \\ F_{34,z} \\ F_{56,x} \\ F_{56,z} \\ F_{78,y} \\ F_{78,z} \end{bmatrix} = 2Bb_*(z_0) \begin{bmatrix} u_x \\ u_y \\ u_{\theta z} \\ u_z \\ u_{\theta x} \\ u_{\theta y} \end{bmatrix} \tag{3.6}$$

Here, the matrix B is calculated to be

$$B = \begin{bmatrix} 0.5 & 0 & 4.8012 & 0 & 0 & 0 \\ 0 & 0 & 0 & 0.25 & -9.6025 & 0 \\ 0 & 0.5 & 4.8012 & 0 & 0 & 0 \\ 0 & 0 & 0 & 0.25 & 0 & -9.6025 \\ 0.5 & 0 & -4.8012 & 0 & 0 & 0 \\ 0 & 0 & 0 & 0.25 & 9.6025 & 0 \\ 0 & 0.5 & -4.8012 & 0 & 0 & 0 \\ 0 & 0 & 0 & 0.25 & 0 & 9.6025 \end{bmatrix}.$$

Equations (3.1) and (3.2) are written in the matrix format to be

$$[m\ddot{x}\ m\ddot{y}\ I_z\ddot{\theta}_z\ m\ddot{z}\ I_x\ddot{\theta}_x\ I_y\ddot{\theta}_y]^T = \left[F_x\ F_y\ T_z\ F_z\ T_x\ T_y\right]^T \tag{3.7}$$

Substitute the left side of (3.6) into (3.3) and then substitute the left side of (3.3) to (3.7) with the notice that $AB = I_{6\times 6}$, the identity matrix, we have

$$[m\ddot{x}\ m\ddot{y}\ I_z\ddot{\theta}_z\ m\ddot{z}\ I_x\ddot{\theta}_x\ I_y\ddot{\theta}_y]^T = 2b_*(z_0)\left[u_x\ u_y\ u_{\theta z}\ u_z\ u_{\theta x}\ u_{\theta y}\right]^T. \tag{3.8}$$

Within a small travel range of the moving platen in the vertical axis, $b_*(z_0)$ is considered a constant. With (3.8), a linear model of the system is established. This is a LTI MIMO system with all the control axes decoupled.

The relations between the 8 currents flowing in the coils and the 6 control efforts are derived from (3.4) and (3.6). First, (3.4) is written in a reverse way.

$$[i_1\ i_2\ i_3\ i_4\ i_5\ i_6\ i_7\ i_8]^T$$
$$= \frac{1}{b_*(z_0)} \begin{bmatrix} sx & cx & 0 & 0 & 0 & 0 & 0 & 0 \\ -cx & sx & 0 & 0 & 0 & 0 & 0 & 0 \\ 0 & 0 & cy & -sy & 0 & 0 & 0 & 0 \\ 0 & 0 & sy & cy & 0 & 0 & 0 & 0 \\ 0 & 0 & 0 & 0 & cx & -sx & 0 & 0 \\ 0 & 0 & 0 & 0 & -sx & -cx & 0 & 0 \\ 0 & 0 & 0 & 0 & 0 & 0 & -sy & -cy \\ 0 & 0 & 0 & 0 & 0 & 0 & -cy & sy \end{bmatrix} \begin{bmatrix} F_{12,x} \\ F_{12,z} \\ F_{34,y} \\ F_{34,z} \\ F_{56,x} \\ F_{56,z} \\ F_{78,y} \\ F_{78,z} \end{bmatrix} \tag{3.9}$$

Substituting the left-hand side of (3.6) into (3.9), we have

$$[i_1\ i_2\ i_3\ i_4\ i_5\ i_6\ i_7\ i_8]^T = 2S_{xy}\, B\, [u_x\ u_y\ u_{\theta z}\ u_z\ u_{\theta x}\ u_{\theta y}]^T. \tag{3.10}$$

Here, S_{xy} is the 8×8 matrix on the right side of (3.10).

From the measurements of the moving platen's position taken at the Hall-effect sensors' locations, the locations of the base points as in Fig. 3-5(a) in the fixed coordinate frame *XYZ* are determined. The elements *sx*, *cx*, *sy*, and *cy* of the matrix S_{xy} can be computed in real-time. The system model in (3.8) and the relations between the electric currents and the control efforts in (3.10) facilitate the linear control system design and real-time implementation for the six decoupled control axes. The model uncertainty due to the out-of-plane error torques generated by the magnetic forces in the horizontal plane is discussed in the Appendix.

3.5 Instrumentation

3.5.1 Hall-Effect Sensors

Two 2-axis Hall-effect sensors 2SA-10G are utilized to measure the magnetic flux-density components generated by the superimposed Halbach magnet matrix. Each sensor can sense two orthogonal flux-density components along the directions shown in Fig. 3-11 [79]. The sensor has the sensing range from −40 mT to 40 mT, magnetic sensitivity of 50 V/T (with the supply voltage of 5.00 V), bandwidth from DC to 18 kHz, and magnetic input conditions of greater than 1000 mT (devices saturates, but not damaged) [79].

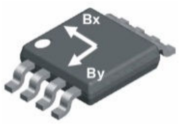

Fig. 3-11 A 3D rendering of the 2SA-10G sensor [79].

For the 2SA-10G sensor to be operated, it is recommended to have the connections as in Fig. 3-12. With a constant distance from the sensor to the magnet matrix, when the sensor moves along a horizontal direction, *x* or *y*, the sensor reading of the *X*- or *Y*-direction magnetic flux density component varies sinusoidally as in (2.1). By taking an inverse trigonometric function, the position of the platen in *x* or *y* can be interpreted. However, one sensor is not sufficient because two positions of the sensor having the peak of the magnetic flux density at the midpoint cannot be distinguished. Therefore, two sensors are needed with a phase separation of 90° or 270° along the motion direction of *x* or *y*.

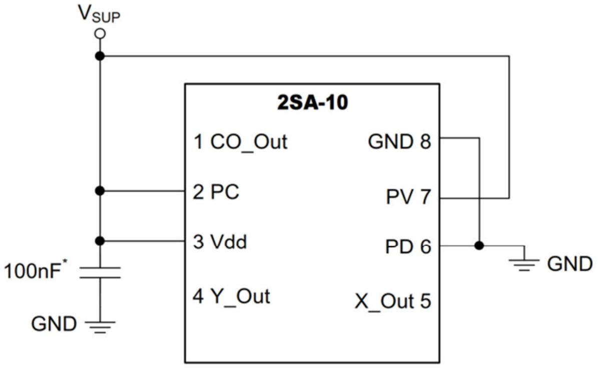

Fig. 3-12 Circuit diagram for the Hall-effect sensor 2SA-10G to be connected with the ground and the power supply [79].

To filter out the high frequency noise in the measurement, an RC low-pass filter is placed between each output of the Hall-effect sensor and an input channel of the ADC board. The corner frequency of the RC filter is 217 Hz. The rms positioning noise of the measurements is between 6 to 8 μm. The output signals of the low-pass filters are fed to the input of four ADC channels of the Pentek[7] 6012 I/O board.

3.5.2 Agilent Laser Interferometers for In-Plane Positioning

A laser head (HP 5517D) and three laser interferometers (HP 10706B) manufactured by Agilent Technologies[8] are used for nano-precision position sensing in *x*, *y*, and the rotation about the vertical axis. The laser beam from the laser head goes through the first beam splitter. One beam coming out from the first splitter is to measure the platen's position in *y*. The other beam from the first splitter is split by the second beam splitter to go through two interferometers to measure the position of the platen in *x*

---

[7] Pentek Inc., One Park Way, Upper Saddle River, NJ 07458, U.S.A

[8] Keysight Technologies (Agilent), 1400 Fountaingrove Parkway, Santa Rosa, CA 95403-1738 U.S.A

at two locations separated by 0.055 m. Figure 1-7 shows the experimental setup with three laser interferometers, three laser receivers, and the moving platen on top of the magnet matrix. The moving platen’s rotational angle about the vertical axis is determined from the difference of the measurements in *x* and the separation of 0.055 m between the two center axes of the laser interferometers.

HP 5517D is a Helium-Neon continuous-wave two-frequency laser source with the output beam power in the range from 180 μW to 1 mW [80]. The nominal vacuum wavelength is 633 nm. Table 3-1 lists other specifications of the HP 5517D laser head. The interferometers used herein are 10706B high-stability plane mirror interferometers. The 10706B design offer high measurement stability during temperature changes with the change of the indicated distance being 40 nm per °C [81].

Table 3-1 Summary of the 5517D laser head [80].

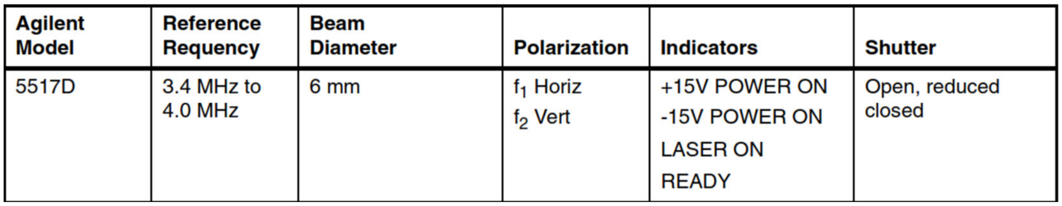

Agilent Model	**Reference Requency**	**Beam Diameter**	**Polarization**	**Indicators**	**Shutter**
5517D	3.4 MHz to 4.0 MHz	6 mm	f_1 Horiz f_2 Vert	+15V POWER ON -15V POWER ON LASER ON READY	Open, reduced closed

A piece of aluminum-coated precision mirror manufactured by Edmund Optics[9] is used to reflect the laser beam for position measurement in the *y*-direction. The mirror’s length and thickness are 75 mm and 7.5 mm, respectively, and the substrate material is fused silica with the mass density of 2.2 g/cm^3. The surface accuracy is 1/10 of the wavelength, being 63 nm.

---

[9] Edmund Optics Inc., 101 East Gloucester Pike, Barrington, NJ 08007-1380, U.S.A

For the x-direction position sensing, two mirrors are used, one for initial testing and one for the long travel-range experiments. Since there are two laser interferometers to measure the position in x, in case the same travel range as in y is desired, the mirror to reflect the laser beams in x must be lengthier than the mirror to measure the position in y. The mirror to measure the platen's position in x for the initial testing is the same as the one mentioned above for the y-axis position sensing. The mirror for long travel range in x is an aluminum-coated precision mirror manufactured by Advanced Optics[10]. The mirror's length is 101.6 mm and its thickness is 9.6 mm. The surface accuracy is ¼ of the wavelength, being 158 nm. The substrate material is fused silica.

The output signal from each laser receiver are fed to a high resolution VMEbus Laser Axis Board placed in a VME chassis. The position and velocity information from each laser interferometer can be accessed by reading the corresponding RAM location of the DSP board in the VME system. The readings are in 32-bit long-integer format.

3.5.3 Nanogage Laser Sensors for Out-of-Plane Positioning

For out-of-plane position measurements, three Nanogage laser displacement sensors are employed. Three sensor heads are arranged at the corners of the moving platen as shown in Fig. 3-5(b) and Fig. 3-6. The readings from sensors 2 and 3, as shown in Fig. 3-6, are to determine the position of the platen in the vertical axis. The readings from sensors 2 and 1 are to calculate the rotation angle of the platen about the Y'-axis. The platen's angular position about X' is determined by the measurements from sensors

---

[10] Advanced Optics Inc., P.O. Box 117, Pewaukee, WI 53072-0117, U.S.A

3 and 1. The maximum displacement range that each sensor can measure is 800 µm [78]. However, to have good linearity between the output voltage and the actual displacement, in this work the sensors are operated in the sensing range from –50 µm to 50 µm relative to the nominal standoff of 3.0 mm from the aluminum plate on top of the magnet matrix. A number of the sensor specifications are given in the following table.

Table 3-2 Specifications of the Nanogage 100 laser displacement sensor [78].

Bandwidth (3 dB)	100 kHz
Input power	12 V at 80 mA
Surface reflectivity for full resolution	4% to 100% specular
Perpendicular tolerance	0.1°

The output signals of the Nanogage laser displacement sensors go through three RC low-pass filters to the input of three ADC channels of the 6012 board. The rms noise of the vertical laser sensors can be as good as 7 nm.

Assuming that z_{s1}, z_{s2}, and z_{s3} are the position measurements from the vertical laser displacement sensors. The position of the moving platen in the vertical axis and in rotations about the *X′*-axis and *Y′*-axis are as follows.

$$z_{platen} = (z_{s2} + z_{s3})/2 \tag{3.11}$$

$$\theta_x = \tan^{-1}[(z_{s3} - z_{s1})/D] \tag{3.12}$$

$$\theta_y = \tan^{-1}[(z_{s2} - z_{s1})/D] \tag{3.13}$$

Here, D = 0.1072 m is the distance between the center axes of sensors 1 and 2 and between those of sensors 1 and 3. For very small angles within a few milliradians, the angular positions in (3.12–13) can be well approximated as

$$\theta_x = (z_{s3} - z_{s1})/D \tag{3.14}$$

$$\theta_y = (z_{s2} - z_{s1})/D. \tag{3.15}$$

3.5.4 Power Amplifier Circuits

There are eight power amplifier units independently supplying the currents to the eight coils on the moving part of the positioning system. At the heart of the power amplifier unit is the power Op Amp PA12A manufactured by Apex Microtechnology[11]. The circuit diagram of the power unit is shown in Fig. 3-13. Except R_6 = 27.4 kΩ, R_7 = 5 kΩ, and R_a = 0.19 Ω, the resistance of each coil, all other resistors are 10 kΩ with the tolerance of 1%. All capacitors in the diagram have the same capacitance of 10 nF. The inductance of each copper coil is L_a = 59 μH.

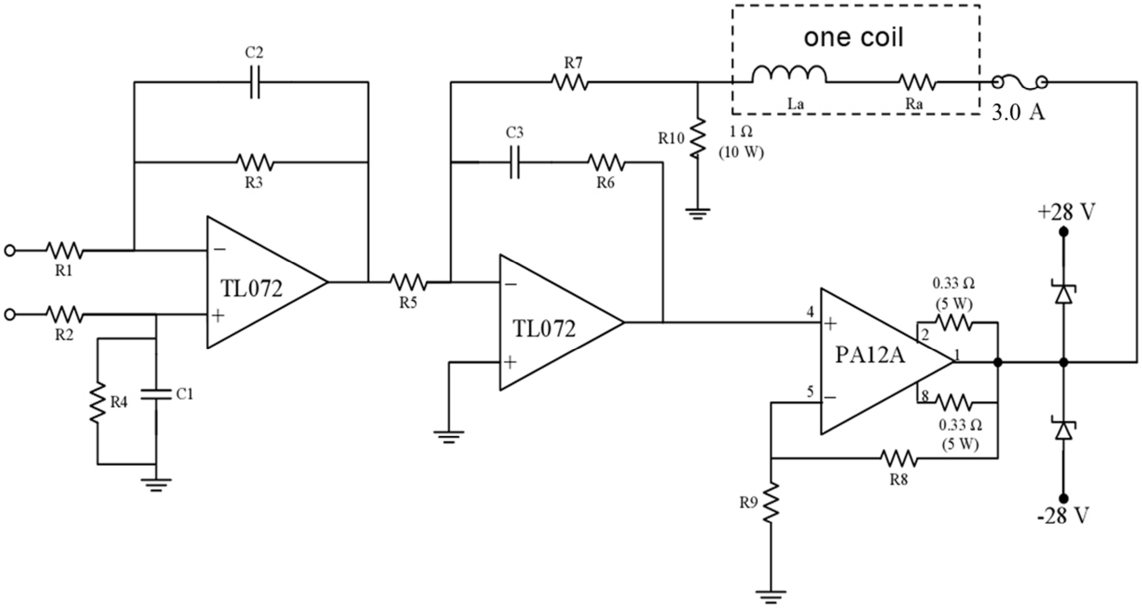

Fig. 3-13 Circuit diagram of the power amplifier unit using Apex PA12A [1].

---

[11] Apex Microtechnology, 5980 N. Shannon Road Tucson, AZ 85741, U.S.A

The PA12A power OP Amp has differential inputs, high slew rate, and very good linearity. Its technical specifications are listed in table 3-3. Figure 3-14 shows a 3D rendering and the pin diagram of the PA12A integrated circuit.

Table 3-3 Technical specifications of the PA12A power OP Amp [82].

Supply voltage range	±10 V to ±50 V
Output current	±15 A peak
Settling time to 0.1% (2V step at 25°C)	2 μs
Slew rate (at 25°C)	4 V / μs
Maximum power dissipation	125 W

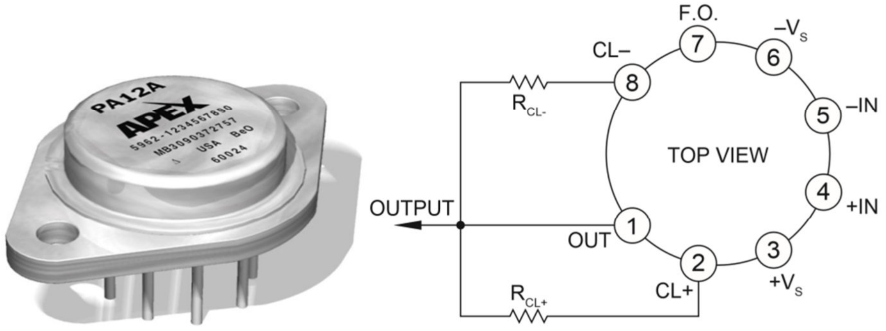

Fig. 3-14 A 3D rendering of the power operational amplifier PA12A and the required connections [82].

The input to a power amplifier unit as in Fig. 3-13 is the commanded voltage signal from a DAC channel of the I/O board connected to the DSP board. The output of the power amplifier unit is the electric current flowing in the coil R_a. From the circuit diagram in Fig. 3-13, the transfer function of the power amplifier unit is established as follows. Here, I_a is the coil current and V_{12} is the differential input voltage of the power amplifier unit.

$$\frac{I_a(s)}{V_{12}(s)} = \frac{(R_9 + R_8)R_7R_3(R_6C_3s + 1)}{R_1R_5[R_{10}(R_9 + R_8)(R_6C_3s + 1) + R_9R_7C_3(L_as + R_a + R_{10})s](R_3C_2s + 1)} \tag{3.16}$$

The magnitude and phase plots versus the frequency of the power amplifier circuit's transfer function are shown in Fig. 3-15. The low-frequency gain of the transfer function is 0.5 and the bandwidth is 1334 Hz. For the control bandwidths of the 6 axes of the positioning system being within 50 Hz, the phase lag that the power amplifier circuit contributes to the system is less than 2.4°. Therefore, it is reasonable to neglect the dynamics of the power amplifier units.

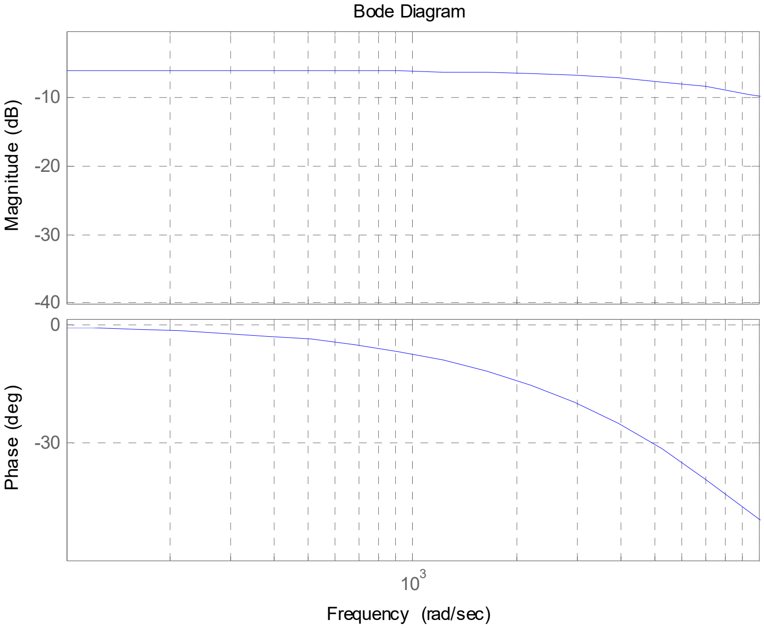

Fig. 3-15 Plots of the magnitude and phase versus frequency of the power amplifier circuit.

3.5.5 Digital-Signal-Processor Board

The control hardware of the positioning system is the DSP board, Pentek 4284, manufactured by Pentek Inc. In the heart of this board is the TMS320C40 processor manufactured by Texas Instrument[12] with the capability to process up to 50 million-floating-point operations per second [83]. The DSP board works on a 32-bit-address

---

[12] Texas Instrument, 12500 TI Boulevard, Dallas, Texas 75243, U.S.A

VME-bus system with the I/O board Pentek 6102 and three laser axis boards. Real-time data communication is established and implemented between the DSP boards and the other four boards. A number of technical specifications of the TMS320C40 processor are listed below [84]. Figure 3-16(a) is a photograph of the 4284 board and Fig. 3-16(b) is its block diagram.

- 40-ns Instruction Cycle Time, single cycle $1/x$, $1/\sqrt{x}$.
- Single-Cycle 40-Bit Floating-Point, 32-Bit Integer Multipliers.
- Twelve 40-Bit Registers, 14 Control Registers, and Two Timers.
- 512-Byte Instruction Cache.
- 8K Bytes of Single-Cycle Dual-Access Program or Data RAM.
- Six-Channel Direct Memory Access (DMA) Coprocessor.

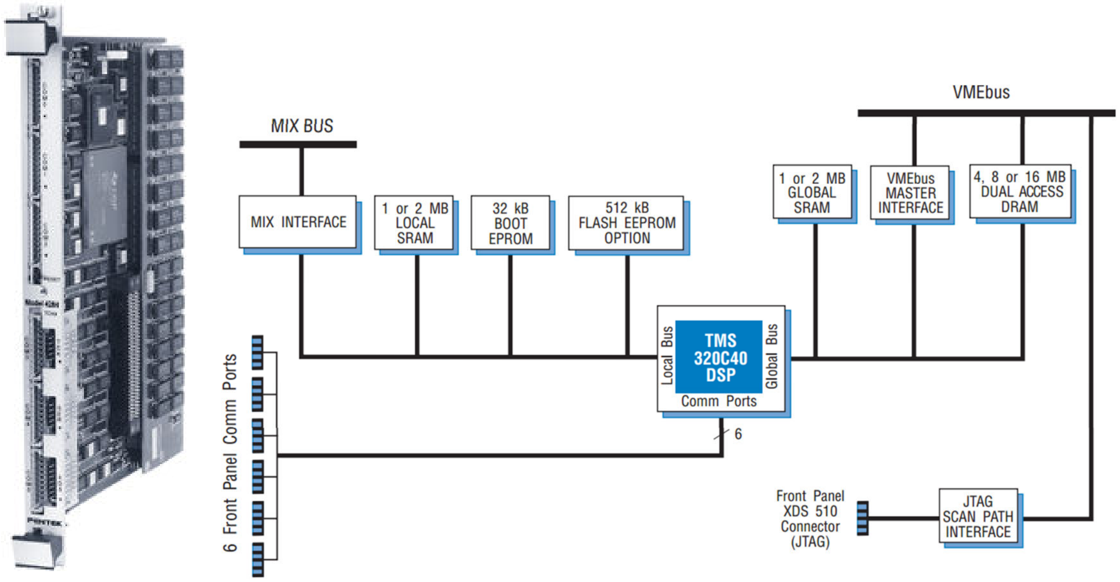

(a) (b)

Fig. 3-16 (a) Photograph of the Pentek 4284 board and (b) its block diagram [83].

3.5.6 Analog-to-Digital and Digital-to-Analog Conversions

The Pentek 6102 I/O board is used for data acquisition and commanding the control signal from the DSP board to the power amplifier circuits. Pentek 6102 has 8 differential-input 16-bit ADC channels and 8 16-bit DAC channels. The maximum sampling rate is 250 kHz; the sampling clock can be either internal or external. The differential input voltage range is –5 V to 5 V [85]. Along with the VMEbus slave interface, the model 6102 has a MIX module to interface directly with a DSP processor [85]. Figure 3-17 is a photograph of the Pentek 6102 I/O board. Table 3-4 gives its technical specifications.

Fig. 3-17 A photograph of the I/O board Pentek 6102 [85].

Table 3-4 Technical specifications of the Pentek 6102 I/O board [85].

Input impedance	10 kΩ (Each Input to Ground)	Output impedance	50 Ω
Signal to noise ratio	> 75 dB (250 kHz)	Output voltage range	±2.5 V (1 kΩ load) ±5.0 V (high impedance)
Sample Clock Reference	20 MHz (Internal) 15 MHz max (External)	Interface	Slave, 32 bit

3.5.7 Overall Instrumental Diagram

The overall instrumental diagram of the maglev stage developed in this work is shown in Fig. 3-18. The diagram describes the instrumentation elements with the signal flows among them. Thanks to the VMEbus interface, the position and velocity information measured by the laser interferometers can be read directly by the DSP board through the laser axis boards. Seven out of eight ADC channels of the I/O board Pentek 6102 are used for data acquisition, three for the vertical laser displacement sensors and four for the two 2-channel Hall-effect sensors. All of eight DAC channels of the 6102 board are utilized to command the signals to control the electric currents flowing in the eight coils on the moving platen.

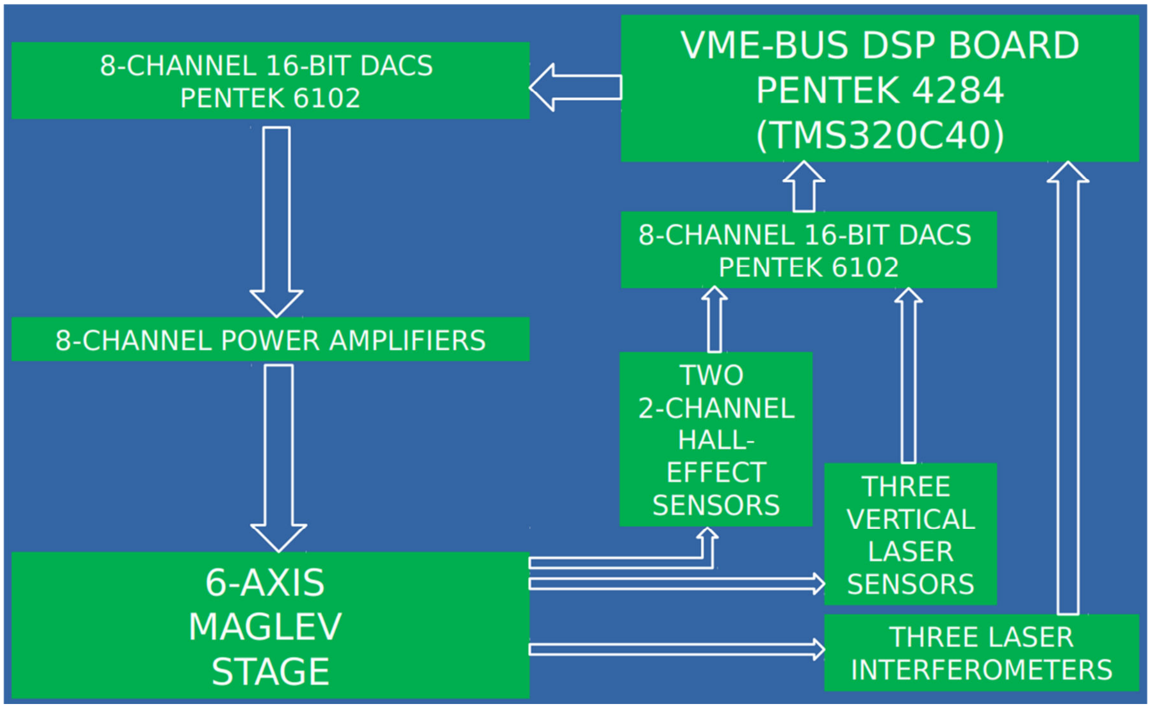

Fig. 3-18 Overall instrumental diagram of the positioning system.

CHAPTER IV

CONTROL SYSTEM DESIGN AND EXPERIMENTAL RESULTS

4.1 Control System Design

4.1.1 Overview of the Control System Design for the 6-DOF Maglev Stage

With the system model established in Chapter III, linear control system design is performed and the controllers are tested to validate the theoretical framework presented in Chapter II. It can be seen from (3.8) that the MIMO system is decoupled into six independent SISO systems for the six axes. Theoretically, the SISO controllers for different axes can be designed and tested independently. However, as this maglev system is naturally open-loop unstable, for the moving platen to be stably magnetically levitated, at least the controllers in x and y must be closed with adequate stability margin. Therefore, some SISO controllers among the six axes have to be designed, tuned, and tested while the controllers for other axes are in open or closed loop with the control stability and performance not yet satisfactory.

PID controllers are selected for the control system design in this work due to a number of factors. Simple structure, ease of implementation, good intuition for tuning and loop shaping are a few to name. Figure 4-1 gives the diagram of the feedback control system for the X- and Y-axes. The feedback loops of other axes have the same structure except that there is no input shaping. The reason is that this planar stage was designed especially for the long-range motions in x and y. In the targeted applications of stepping, scanning, and micro/nano scale manipulation, the controllers of the other axes are for constant reference tracking or just making small adjustments of the platen's orientations and vertical displacements. In translations along *x* and *y*, input shaping is needed only when the platen travels a distance on the order of millimeters. For these motions, the trapezoidal-velocity trajectory planning helps reduce the vibrations and make the platen's movement smooth. Details of the input shaping are presented in the next part. For step responses in *x* and *y* with the step size from 10 nm to hundreds of micrometers, the vibrations and perturbations in other axes are relatively small and not considerably affect the stability and performance of the 6-DOF system. In this case the input shaping can be skipped if there is a concern about the CPU time usage.

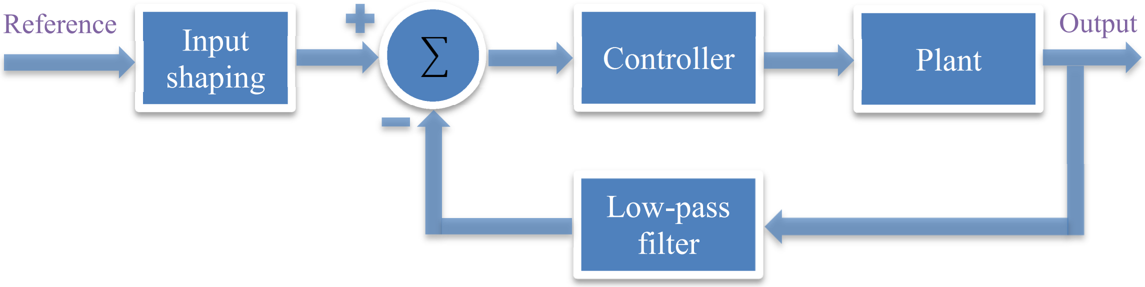

Fig. 4-1 Feedback control diagram of the *X*- and *Y*-axes.

The digital low pass filters in the feedback paths in all of the six control loops have the same continuous-time transfer function of 1/(0.001s + 1) and the corner frequency of 159.15 Hz. The sampling rate of the system is 4000 Hz based on the tests of the computing time of the CPU to run all the commands in the interrupt service routine of the control software.

If the closed-loop control bandwidth is too low, the control stiffness is small accordingly, and the capability to reject the force disturbances is limited. If the closed-loop control bandwidth is too high, the low-pass filter's corner frequency must also be high, allowing more noise to pass through the system to the output. The choice of the closed-loop control bandwidth is, therefore, based on the characteristics of the sensing noise, the control performance in positioning noise, and disturbance rejection.

4.1.2 Control System Design for In-Plane Motions

According to the system model in (3.8), the transfer function of the *x*, *y*, and θ_z plants are, respectively

$$G_{xy}(s) = \frac{2.27}{s^2}, G_{\theta_z}(s) = \frac{473}{s^2}. \tag{4.1}$$

The continuous time PID controller in the *X*- and *Y*-axes is designed to be

$$C_{xy}(s) = 36000 + 100s + \frac{2400000}{s}. \tag{4.2}$$

Figures 4-2 is the Bode plot of the *X*- and *Y*-axes loop transfer functions with the controller given in (4.2). The phase margin is 33.2° and the crossover frequency is 313 rad/s, or 49.8 Hz. Figure 4-3 shows the Bode plot of the closed-loop system. The 3-dB bandwidth is 87.8 Hz. This high control bandwidth is sufficient for the purpose of disturbance rejection and maintaining adequate stiffness when the platen is magnetically levitated. A tradeoff is that the 12.7 dB peak of the closed-loop gain is seen at 44.9 Hz. For small step sizes below 1 mm in translations along *x* and *y*, the controller performs satisfyingly. For larger travels in the *X*- and *Y*-directions, perturbations in the other axes induce the vibrations back to the *X*- and *Y*-axes and input shaping is needed to make the platen's movement smooth.

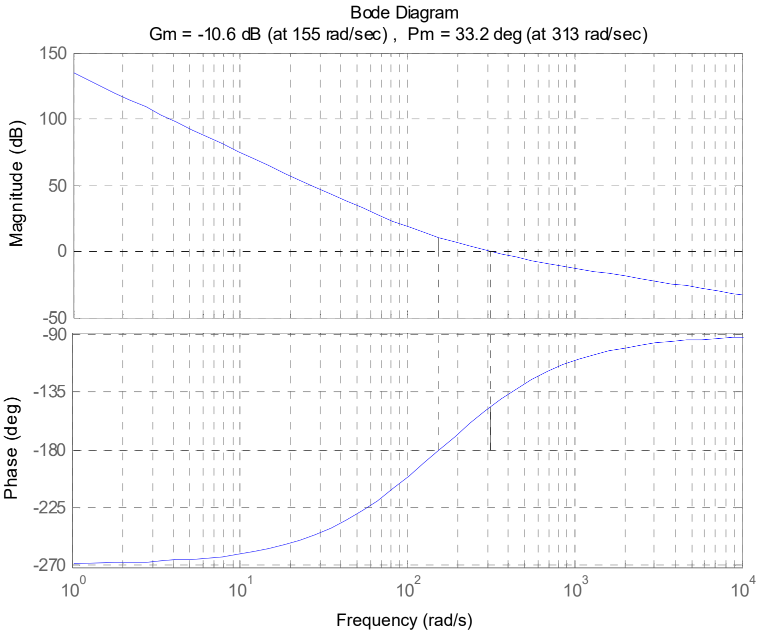

Fig. 4-2 Bode plot of the loop transfer function in *x* and *y*.

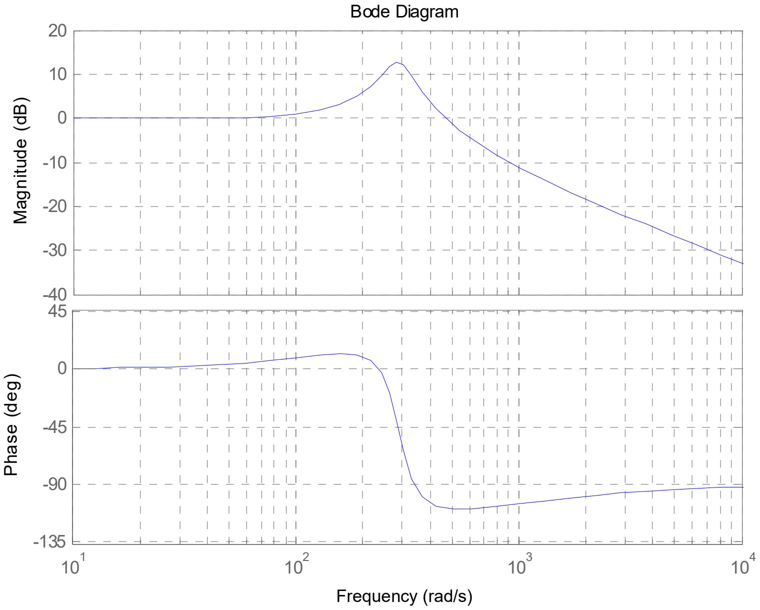

Fig. 4-3 Bode plot of the closed-loop systems in *x* and *y*.

For high-speed and high-acceleration long-range stepping motions in x and y, trapezoidal-velocity profile is selected to be the input shaping to make the control system more stable and reduce the perturbations and vibrations. The purpose of the trapezoidal-velocity profile for input shaping is to make a smooth transition of the position profile and a continuous transition of the velocity profile during the motion. With a trapezoidal velocity profile, the acceleration is constant and positive during accelerating, zero during cruise, and constant and negative during deceleration. For the trapezoidal-velocity profile to test the maximum speed and acceleration in this work, the accelerating time, cruise time, and the decelerating time are set equal. This is to distribute the jerk into different phases of the motion equally within the settling time only on the order of hundreds of milliseconds.

Assuming that T is the theoretical transient time of the trapezoidal velocity profile for a translational motion from 0 to x_{ref} in x, a_{cc} is the acceleration in the time from 0 to $T/3$ and $-a_{cc}$ is the acceleration in the time from $2T/3$ to T, we have

$$x = a_{cc}t^2,\ 0 \le t \le T/3 \tag{4.3}$$

$$x = \frac{a_{cc}T^2}{9} + \left(t - \frac{T}{3}\right)\frac{2a_{cc}T}{3} = \frac{2a_{cc}T}{3}t - \frac{a_{cc}T^2}{9}, T/3 \le t \le 2T/3 \tag{4.4}$$

$$x = x_{ref} - a_{cc}(t - T)^2, 2T/3 \le t \le T \tag{4.5}$$

$$x_{ref} = 4a_{cc}T^2/9. \tag{4.6}$$

Here, t is the time and $t = 0$ at the beginning of the trapezoidal velocity profile. The trapezoidal velocity profile given in (4.3–4.8) can be characterized by only two parameters among x_{ref}, a_{cc}, and T. In the experiments presented in this chapter, the theoretical time of the trapezoidal velocity profile is $T = 0.3$ s.

With the plant model in θ_z given in (4.1), the continuous-time PID controller for θ_z is designed to be

$$C_{\theta_z}(s) = 300 + s + \frac{24000}{s}. \tag{4.7}$$

Figures 4-4 is the Bode plot of the loop transfer function in θ_z with the controller given in (4.7). The phase margin is 57.2°, and the crossover frequency is 512 rad/s, or 81.5 Hz.

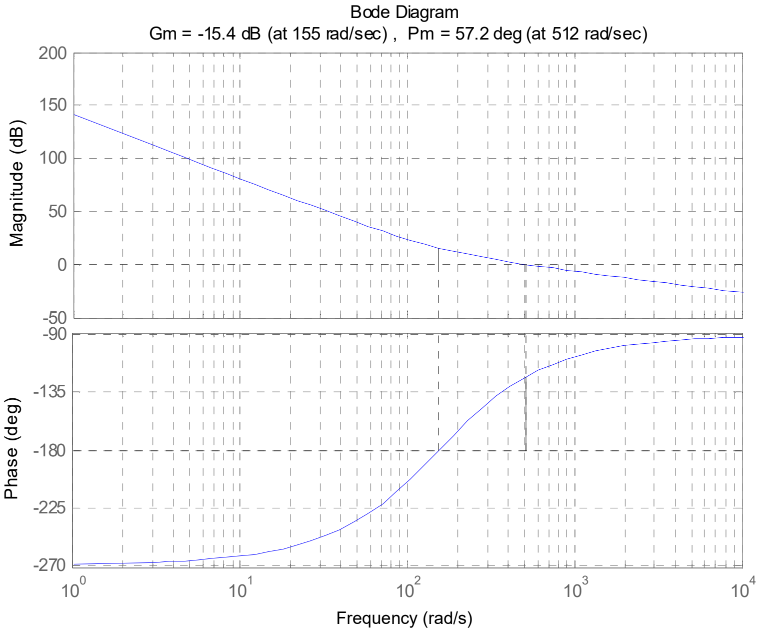

Fig. 4-4 Bode plot of the loop transfer function in θ_z with the PID controller in (4.7).

Figure 4-5 is the Bode plot of the closed-loop system in θ_z. The 3-dB bandwidth is 154 Hz. In practice, the positioning stage has less vibration when the control bandwidth in θ_z is higher than that of x and y. This is reasonable because any perturbations in θ_z cause considerable perturbations in x and y but a perturbation in x or y alone may cause no significant vibration in θ_z. Therefore, the control stiffness in θ_z need to be relatively strong and the control bandwidth in θ_z must be high enough to reject the disturbances. The gain of the sensitivity transfer function in θ_z must be sufficiently small at the disturbance frequencies to attenuate the fluctuations in θ_z before they induce vibrations in x and y.

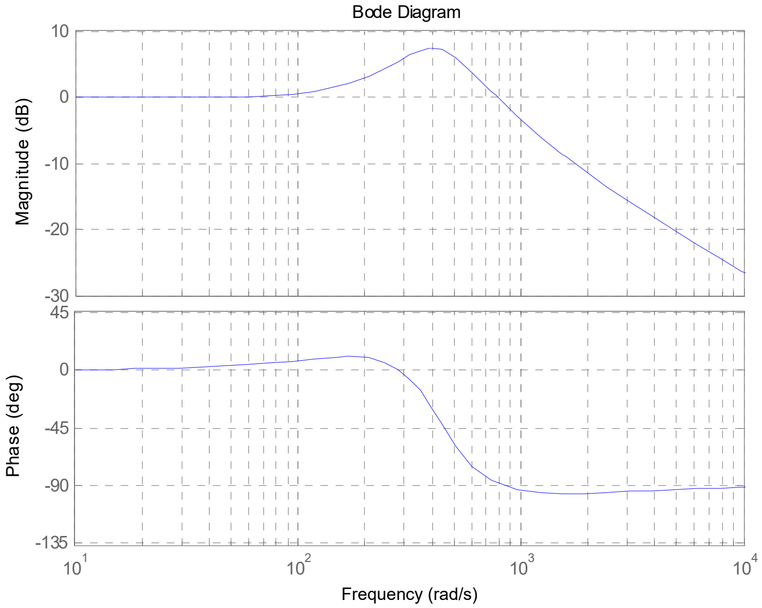

Fig. 4-5 Bode plot of the closed-loop systems in θ_z.

4.1.3 System Identification and Controller Design for Out-of-Plane Motions

As discussed in Section 3.4 where the mathematical model of the positioning stage was established, the moving platen's weight was canceled by a DC control effort. In the experiments presented herein, this DC control effort is introduced to the *Z*-axis after all the control loops in x, y, θ_z, θ_x, and θ_y are closed. Gradually increasing the control effort in z makes the moving platen lifted up. The moving platen can be magnetically levitated stably with a DC control effort in z and five other control axes in closed loop. However, in this case, the capability of the moving platen to reject the force disturbances and attenuate the vibrations is very limited. In addition, the platen cannot perform precise motion generation in z.

To have the desired stability and performance quality, the control loop in z must be closed. In addition to the closed-loop control effort in z, the DC control effort is needed so that the low-frequency gain and the control bandwidth of the closed-loop controller do not have to be too large. Without the DC control effort, the closed-loop controller treats the platen's weight as a force disturbance. It needs a high control bandwidth with a large low-frequency controller gain to reject that large disturbance. The system ends up having considerable noise in the output and the capability to attenuate the vibrations induced by the perturbations from other axes is limited.

For the moving platen to be levitated by a DC control effort, the controllers to close the control loops in θ_x and θ_y are manually tuned to have a negligible steady-state error and the positioning noise on the order of microradians. When the platen is magnetically levitated, the impact of the DC control effort and the cables connected to the platen can be quantified by a spring constant and a damping coefficient added to the model given in (3.2) and (3.8). The new dynamic model in the Z-axis has the form of

$$G_z(s) = \frac{b_*(z_0)}{ms^2 + cs + k} = \frac{1.70}{0.75s^2 + cs + k}. \tag{4.8}$$

The spring constant k is identified by two methods. In the first method, several experiments are performed in which sample masses are added or taken out from the levitated platen and the associated changes in the vertical positions of the platen are recorded. In the second methods, a known DC control effort (–0.1, 0.1 or 0.2 A) is introduced to the dynamics of the moving platen while it is stably lifted up by a DC control effort to a certain height within 40 μm. The DC control effort is to cancel the weight of the moving part and maintain a steady-state position of the platen in z. Any displacements of the platen from this steady-state position are caused by the added control effort. From this, the DC gain of the transfer function in (4.8) is determined. The spring constant k is identified to be 94600 N/m. Figure 4-6 shows the response to a DC control effort of 0.2 A added to the levitated platen at 13.5 s. The consistency of the results between the two methods mentioned above also demonstrates the accuracy of the calculation of $b_*(z_0)$ in the theoretical work in Chapter III.

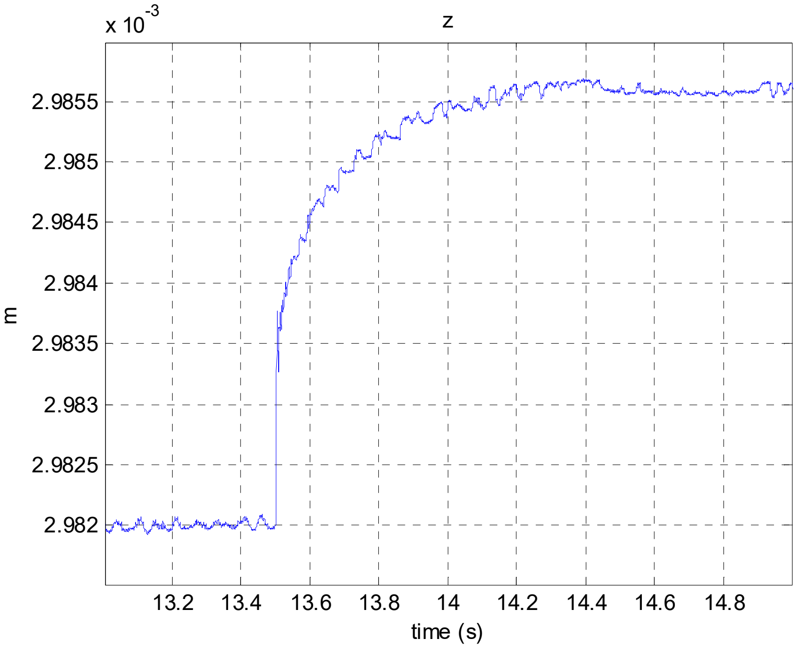

Fig. 4-6 Response to a *Z*-axis DC control effort of 0.2 A added in open loop.

The damping coefficient c in (4.8) is identified by the phase lag between the output and the input of the open-loop system response to the sinusoidal inputs. While the moving platen is magnetically levitated by a DC control effort in open loop, a sinusoidal input in the *Z*-axis is introduced, and the output is recorded and plotted. Figure 4-7 presents the platen's open-loop response to a sinusoidal input. After 15 s, the input frequency is 40 Hz, and the observed phase lag in the output is 57.6°. From the model in (4.8), the spring constant k = 94600 N/m, the damping coefficient c is calculated to be 890 N-s/m. The Z-axis system model identified in the vicinity of the position where the platen is levitated stably by the primary DC control effort is

$$G_z(s) = \frac{1.70}{0.75s^2 + 890s + 94600}. \tag{4.9}$$

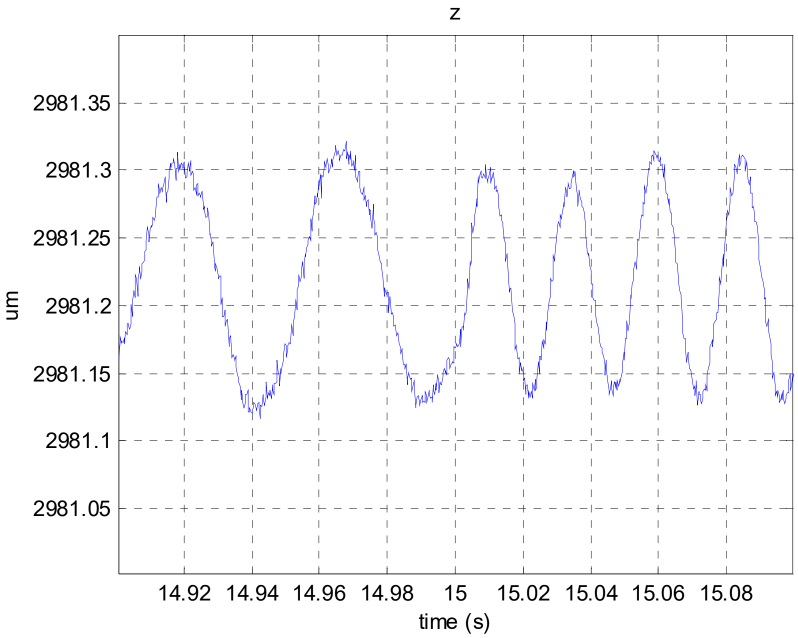

Fig. 4-7 The open-loop response in z to a sinusoidal input at 20 Hz before 15 s and 40 Hz after.

The Z-axis system model given in (4.9) is highly overdamped with the damping ratio of 1.67. For this system, a proportional integral (PI) controller is sufficient so that the control performance and stability are satisfactory. The Bode plot of the plant only is shown in Fig. 4-8. The continuous-time PI controller for the Z-axis is designed to be

$$C_z(s) = 40000 + \frac{560000}{s}. \tag{4.10}$$

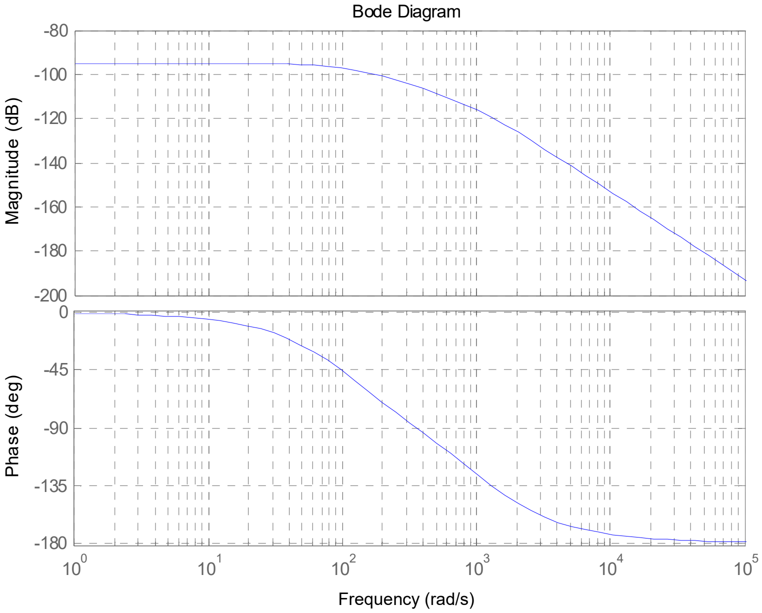

Fig. 4-8 Bode plot of the *Z*-axis plant.

Figure 4-9 is the Bode plot of the loop transfer function with the PI controller given in (4.10). Figure 4-10 presents the Bode plot of the closed-loop system. The 3-dB closed-loop bandwidth of 1.2 Hz is low because the associated *Z*-axis open-loop system is not identified when the platen is at rest but in the vicinity of the equilibrium point where the platen is levitated stably by a DC control effort. These DC and closed-loop control efforts work as the coarse and fine control efforts, respectively. This is done on purpose to reduce the control bandwidth in the closed-loop *Z*-axis while maintaining sufficient stiffness for the moving platen.

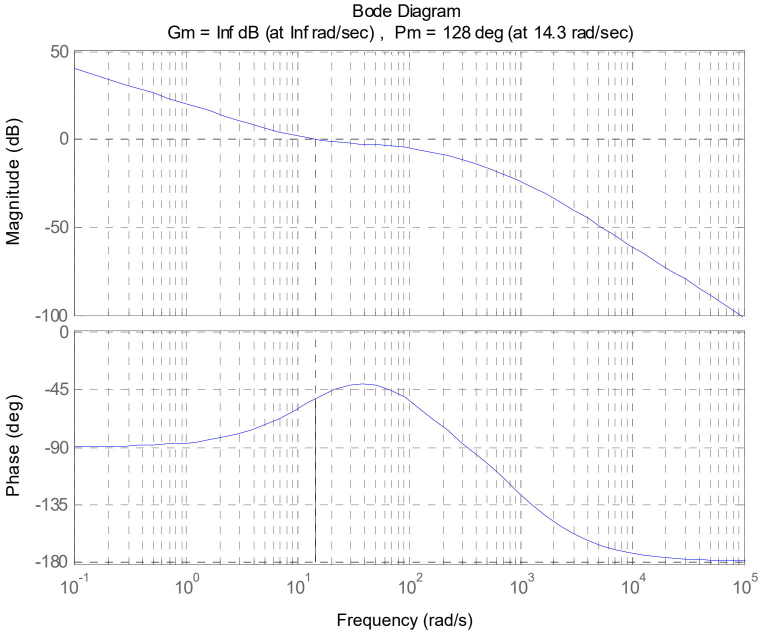

Fig. 4-9 Bode plot of the loop transfer function with the PI controller given in (4.10).

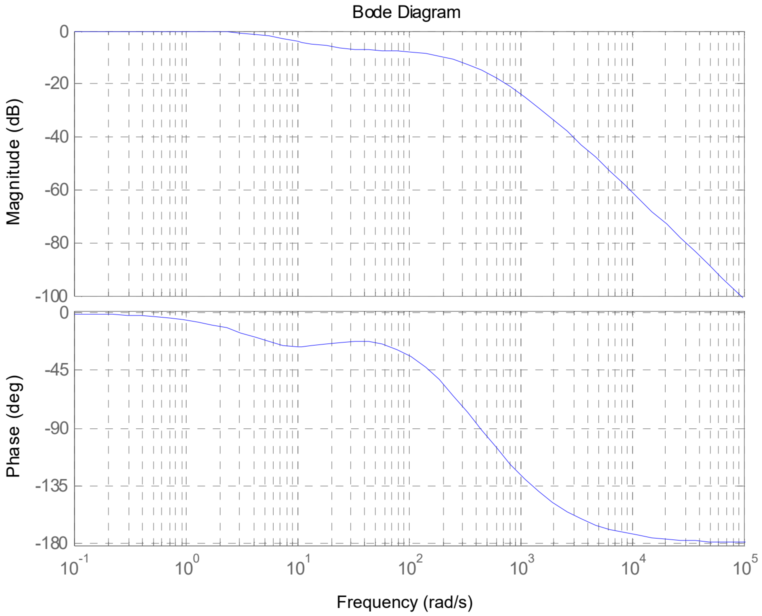

Fig. 4-10 Bode plot of the *Z*-axis closed-loop system.

The mathematical models for the out-of-plane rotations in θ_x and θ_y need to be augmented with a spring constant and a damping coefficient to represent the dynamics of the systems more accurately. In this particular case, the suspension of the moving platen with the four forcers arranged in a cross configuration can be modeled as four parallel sets, each with a spring and a damper, that equally contribute to the total spring constant of 94600 N/m and damping coefficient of 890 N-s/m. The torsional stiffness and damping coefficient are identified from the linear spring constant, the linear damping coefficient, and l = 52.1 mm, half of the distance between the two opposite forcers. These parameters and the mathematical models of the dynamics in θ_x and θ_y are as follows.

$$k_{torsional} = (k/2)\, l^2 \tag{4.11}$$

$$= 128 \text{ N-m/rad}$$

$$c_{torsional} = (c/2)\, l^2 \tag{4.12}$$

$$= 1.21 \text{ N-m-s/rad}$$

$$G_{\theta_x\theta_y}(s) = \frac{1.7}{0.0019s^2 + 1.21s + 128} \quad . \tag{4.13}$$

With this plant model, the following continuous-time PID controller is designed for the purpose of reference tracking and disturbance rejection.

$$C_{\theta_{xy}}(s) = 70 + 0.09s + \frac{17600}{s}. \tag{4.14}$$

Figure 4-11 is the Bode plot of the loop transfer function with the plant given in (4.13) and the PID controller of (4.14). The phase margin is 58.8° and the crossover frequency is 156 rad/s or 24.8 Hz. Figure 4-12 shows the Bode plot of the closed-loop systems in θ_x and θ_y. The 3dB bandwidth is 38 Hz.

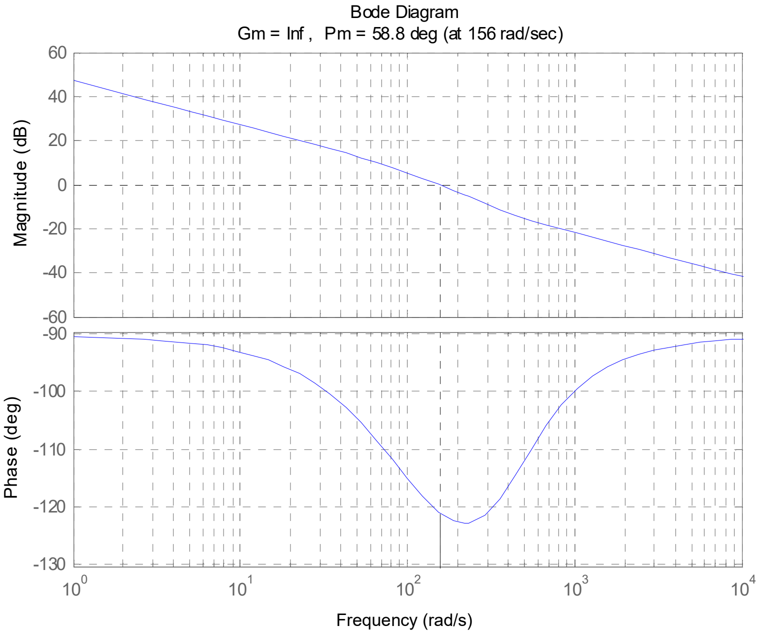

Fig. 4-11 Bode plot of the loop transfer function in θ_x and θ_y.

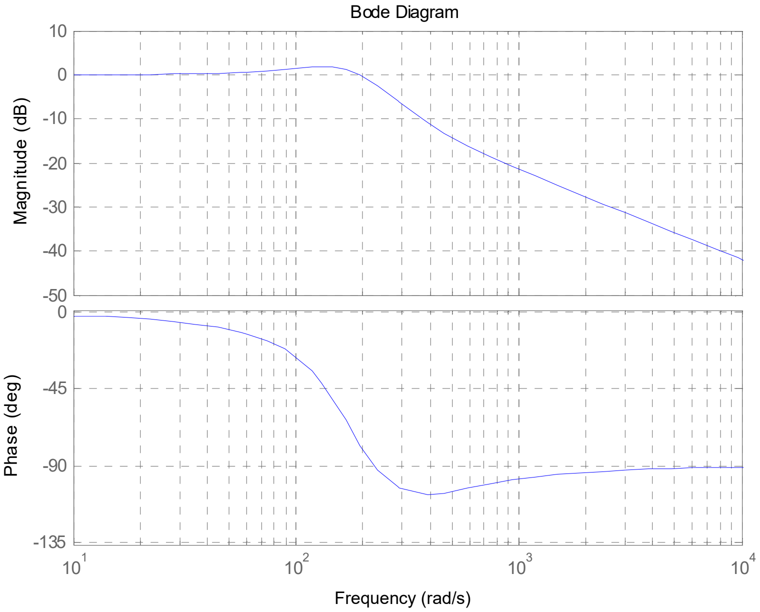

Fig. 4-12 Bode plot of the closed-loop systems in θ_x and θ_y.

4.2 Implementation of the Controllers

4.2.1 Procedures of the Controller Implementation

Figure 4-13 shows the sequence of the steps and procedures to perform 6-DOF maglev positioning in most of the experiments in this thesis. Before the first step, an initial position of the moving part on top of the magnet matrix must be selected. When the moving platen is at rest at this location, the laser head, interferometers, and receivers are deployed and adjusted so that the laser beams reflected from the precision mirrors go through the interferometers and the output beam from each interferometer is well aligned with the center axis of the associated receiver.

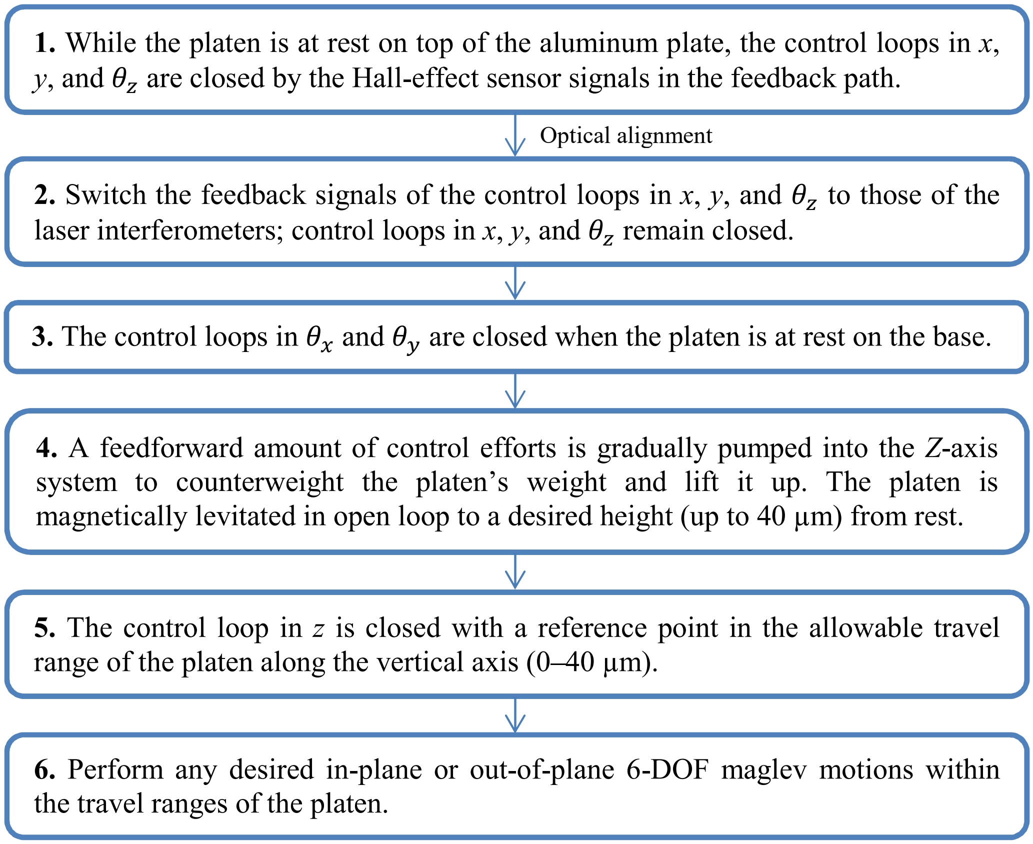

1. While the platen is at rest on top of the aluminum plate, the control loops in x, y, and θ_z are closed by the Hall-effect sensor signals in the feedback path.

2. Switch the feedback signals of the control loops in x, y, and θ_z to those of the laser interferometers; control loops in x, y, and θ_z remain closed.

3. The control loops in θ_x and θ_y are closed when the platen is at rest on the base.

4. A feedforward amount of control efforts is gradually pumped into the *Z*-axis system to counterweight the platen's weight and lift it up. The platen is magnetically levitated in open loop to a desired height (up to 40 μm) from rest.

5. The control loop in z is closed with a reference point in the allowable travel range of the platen along the vertical axis (0–40 μm).

6. Perform any desired in-plane or out-of-plane 6-DOF maglev motions within the travel ranges of the platen.

Fig. 4-13 The sequence of tasks to perform 6-DOF maglev motions.

In the first step, the platen is moved to its initial position from a random position in the initial position's vicinity. The precision mirrors on the moving platen are then well aligned with the laser interferometers and receivers. In this step, the signals used for feedback are from the two Hall-effect sensors attached to the moving platen. The positioning resolution offered by the low-cost Hall-effect sensors, being 8–10 µm, is sufficient for the purpose of aligning the laser beams.

In step 2, when the laser interferometers are ready, the feedback signals in the control loops are switched from the Hall-effect sensors so that the stage can perform nano-precision positioning. When the laser interferometers and the laser axis boards start working and the signals are read from the laser axis boards by the DSP, the nominal readings are zero. At this time the moving platen is still at rest on top of the magnet matrix. Those zero readings are associated with the initial position of the platen. When the platen moves in the horizontal *xy* plane, the laser interferometers' readings show the platen's positions relative to its initial position. The base points used to establish the force model of the system as in Fig. 3-5 and (3.10) are calculated from the locations of the base points in the *XYZ* frame when the platen is at its initial position and the readings of the laser interferometers. Therefore, the initial position of the moving platen can be anywhere above the magnet matrix, as long as the effective area in the bottom of the coils are within the square magnet matrix and the optical components of the laser interferometers are well deployed and aligned.

In step 3, while the platen sits on the aluminum plate on top of the magnet matrix, the values of θ_x and θ_y are stored to be the reference points for the feedback control systems after the control loops are closed. The nominal values of θ_x and θ_y are constants because the platen is still at rest on the base with only the control loops in x, y, and θ_z closed with constant references for feedback. After the values of θ_x and θ_y are recorded, the control loops in θ_x and θ_y are closed with the recorded values being the reference points. The reason to use the recorded values instead of zero for the references in θ_x and θ_y is that the standoff distances of the three vertical laser displacement sensors cannot be guaranteed to be equal. By having the recorded values as the references, if the steady-state errors in the feedback control of θ_x and θ_y are zero, the bottom surface of the moving platen is parallel with the surface of the aluminum plate on top of the magnet matrix.

In step 4, when all the control loops are closed except the one in *z*, the platen is ready to be lifted up. The control effort in *z* is gradually increased and the platen is lifted up from rest. The process stops when the platen is at a certain height, which is 5–15 μm from rest. In step 5, the control loop in *z* is closed with the desired reference point in the 1–2 μm vicinity of the platen's position in the vertical axis obtained in step 4. By doing this, the closed-loop control stiffness and the positioning noise in *z* can be reduced while the sub-micrometer displacements can still be finely controlled. In most of the experiments, the total time to complete steps 1–5 is 26 s. After step 5, the positioning stage is ready to perform 6-DOF positioning. The total number of data points stored and saved for the purpose of analyzing and plotting is 65000.

4.2.2 Real-Time Digital Controller Implementation

The positioning stage's controllers are programmed and run in the same interrupt service routine with the commands to acquire the data from all the sensors. The sampling rate of the control system is 4000 Hz. This sampling rate implies that the total time to run all the commands in the interrupt service routine must be within 250 μs. In the interrupt service routine, there are the commands to read the data in the buffers associated with the ADC channels connected to the sensors and the laser axis boards, the commands to filter the signals and convert the signals to the position information (with the Hall-effect sensors) for feedback, the commands to calculate the position errors and the controllers, the commands to output the control signals to the power amplifier circuits. Converting the Hall-effect sensor measurements to the position information requires four inverse trigonometric functions. These four inverse trigonometric functions are only used in the first stage of the control process when the position information is obtained from the Hall-effect sensors to do the optical alignments and make the laser interferometer signals available. After the measurements for feedback signals are switched from the Hall-effect sensors to the laser interferometers, all the associated ADC and inverse trigonometric commands are no longer run. Other four trigonometric functions are needed in the calculation of the control efforts, as can be seen in (3.8–9). These four trigonometric functions must run all the time. A test program is written and run with the data acquisition, signal filtering, control-effort calculation, and control-signal output commands. The test program is able to run well within 100 μs. The sampling rate is conservatively chosen to be 4000 Hz with the consideration that the actual programs to run the maglev experiments have more additions, multiplications, and condition commands compared to the test program.

With the sampling period of 0.00025 s, the low-pass filter with the transfer function of 1/(0.001s + 1) is converted to the digital form by the Matlab c2d command to be

$$H(z) = \frac{0.2212}{z - 0.7788}. \tag{4.15}$$

The continuous-time PID and PI controllers given in (4.2), (4.7), (4.10), and (4.14) are converted to the digital controllers by the trapezoidal transformation for the integral.

$$u_{xi}[k] = u_{xi}[k-1] + 300(e_x[k] + e_x[k-1]) \tag{4.16}$$

$$u_x[k] = 36000 e_x[k] + 400000(e_x[k] - e_x[k-1]) + u_{xi}[k] \tag{4.17}$$

$$u_{yi}[k] = u_{yi}[k-1] + 300(e_y[k] + e_y[k-1]) \tag{4.18}$$

$$u_y[k] = 36000 e_y[k] + 400000(e_y[k] - e_y[k-1]) + u_{yi}[k] \tag{4.19}$$

$$u_{\theta_z i}[k] = u_{\theta_z i}[k-1] + 3(e_{\theta_z}[k] + e_{\theta_z}[k-1]) \tag{4.20}$$

$$u_{\theta_z}[k] = 300 e_{\theta_z}[k] + 4000(e_{\theta_z}[k] - e_{\theta_z}[k-1]) + u_{\theta_z i}[k] \tag{4.21}$$

$$u_{zi}[k] = u_{zi}[k-1] + 70(e_z[k] + e_z[k-1]) \tag{4.22}$$

$$u_z[k] = 40000 e_z[k] + u_{zi}[k] \tag{4.23}$$

$$u_{\theta_x i}[k] = u_{\theta_x i}[k-1] + 2.2(e_{\theta_x}[k] + e_{\theta_x}[k-1]) \tag{4.24}$$

$$u_{\theta_x}[k] = 70 e_{\theta_x}[k] + 360(e_{\theta_x}[k] - e_{\theta_x}[k-1]) + u_{\theta_z i}[k] \tag{4.25}$$

$$u_{\theta_y i}[k] = u_{\theta_y i}[k-1] + 2.2\left(e_{\theta_y}[k] + e_{\theta_y}[k-1]\right) \tag{4.26}$$

$$u_{\theta_y}[k] = 70 e_{\theta_y}[k] + 360\left(e_{\theta_y}[k] - e_{\theta_y}[k-1]\right) + u_{\theta_y i}[k] \tag{4.27}$$

4.3 Experimental Results in Positioning Resolutions

Figure 4-14 shows three steps of 10 nm in *X*. The peak-to-peak positioning noise is within 18 nm. Figure 4-15 presents a step of 10 nm in *Y*. A step of 5 nm in *X* is shown in Fig. 4-16 with the peak-to-peak positioning noise within 13 nm. Two steps of 1 µrad in θ_z are plotted in Fig. 4-17. The peak-to-peak positioning noise is only 0.1 µrad. Figure 4-18 shows two steps of 10 nm in *Z* performed at the time instants of 14 s and 14.75 s. The achieved peak-to-peak positioning noise in *Z* is 40 nm, as can be seen in Fig. 4-18. In Fig. 4-19, there are three consecutive steps of 0.1 µrad and one step of 0.3 µrad in θ_x. The achieved peak-to-peak positioning noise in θ_x is 0.8 µrad. Figure 4-20 presents a step of 0.1 µrad in θ_x from 359.8 to 359.9 µrad performed at the time of 13 s.

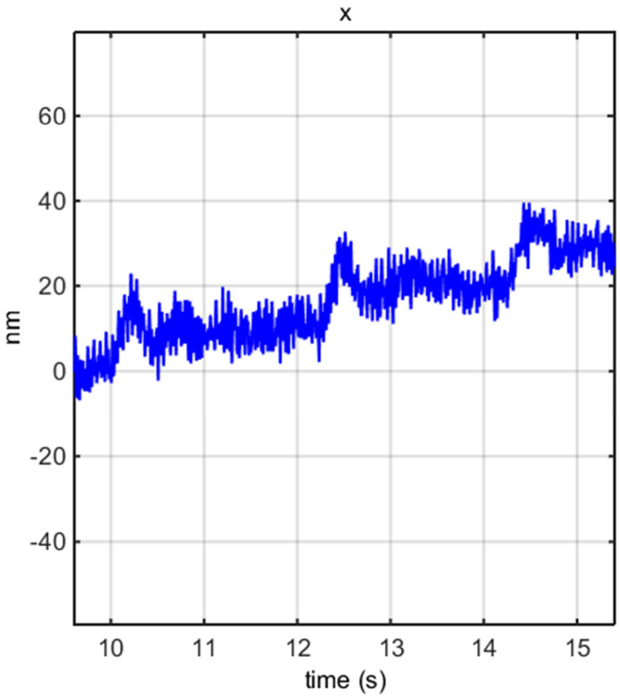

Fig. 4-14 A series of three consecutive 10-nm step responses in *x*.

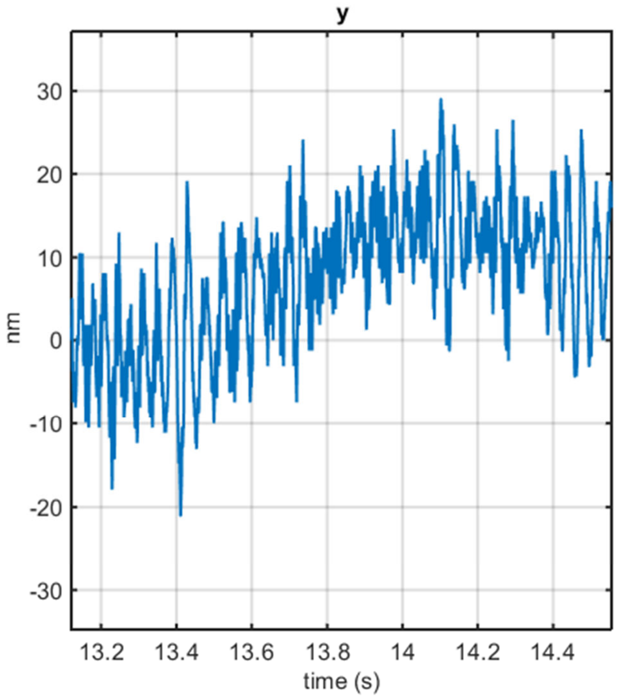

Fig. 4-15 A step response of 10 nm in *Y*.

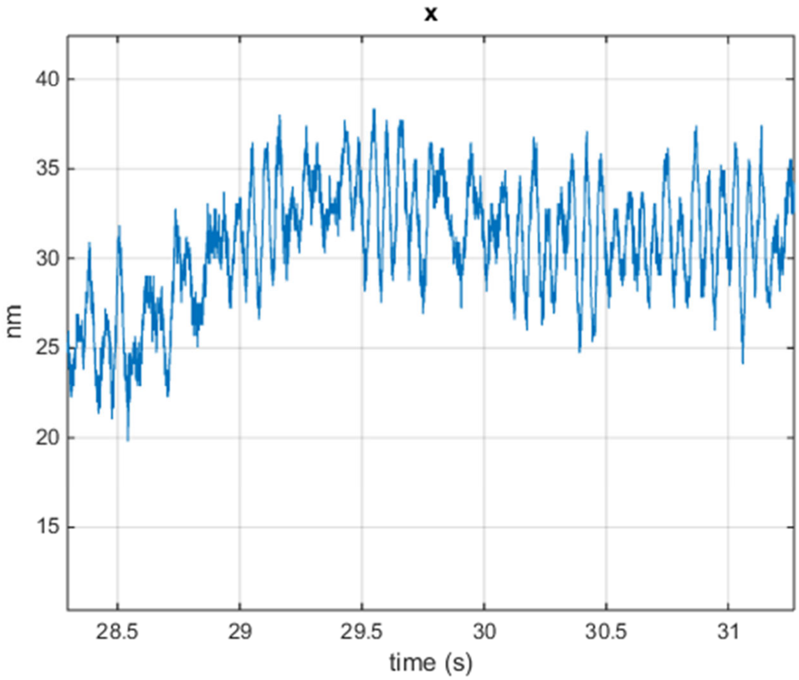

Fig. 4-16 A step of 5 nm in x.

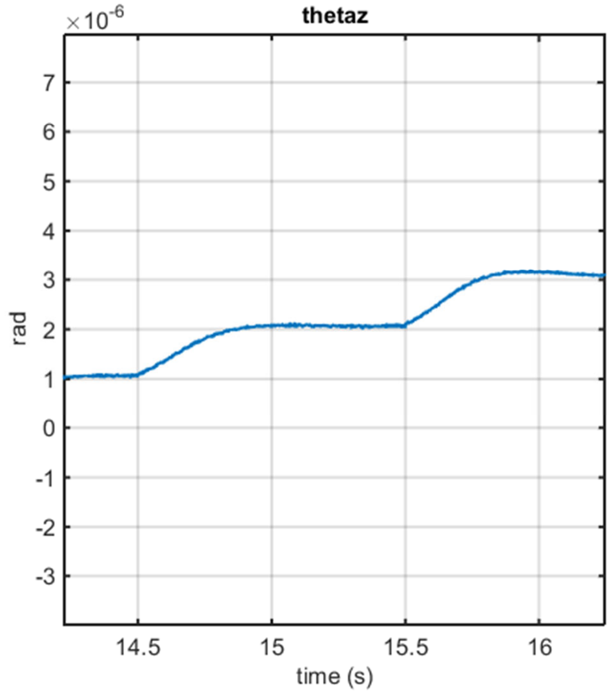

Fig. 4-17 Two consecutive steps of 1 μrad in θ_z.

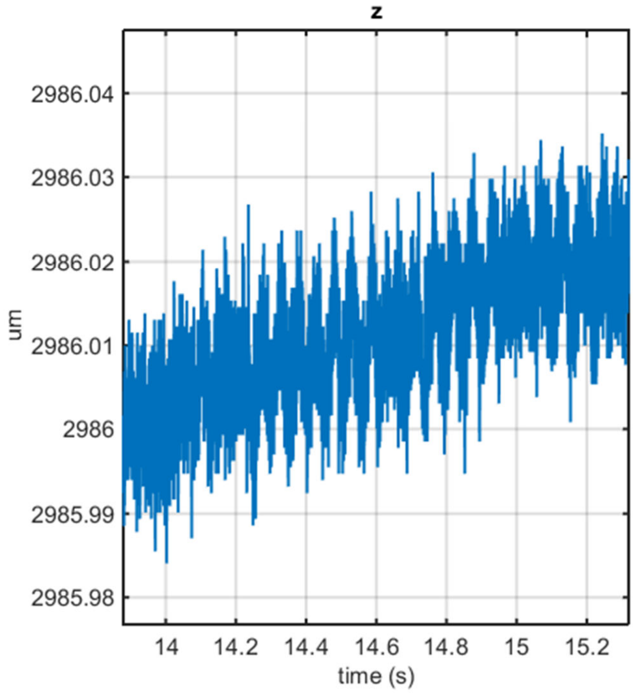

Fig. 4-18 Two consecutive steps of 10 nm in Z.

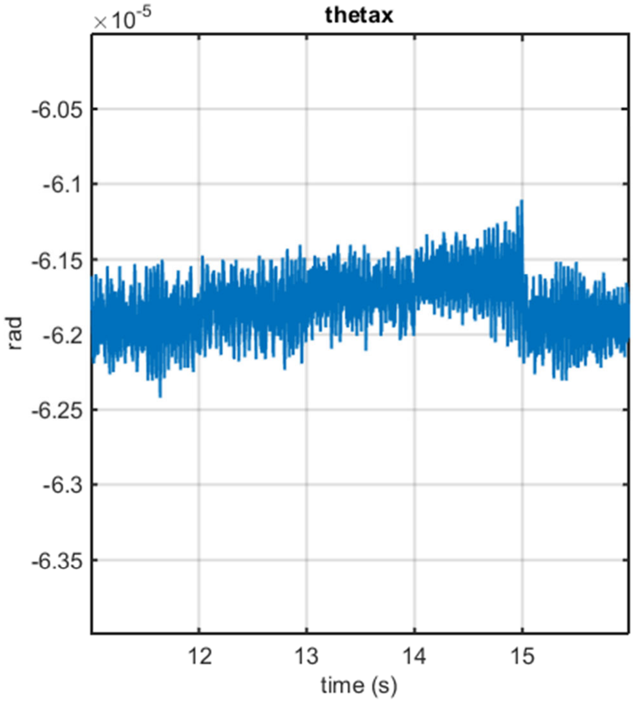

Fig. 4-19 Three steps of 0.1 µrad and a step of –0.3 µrad in θ_x.

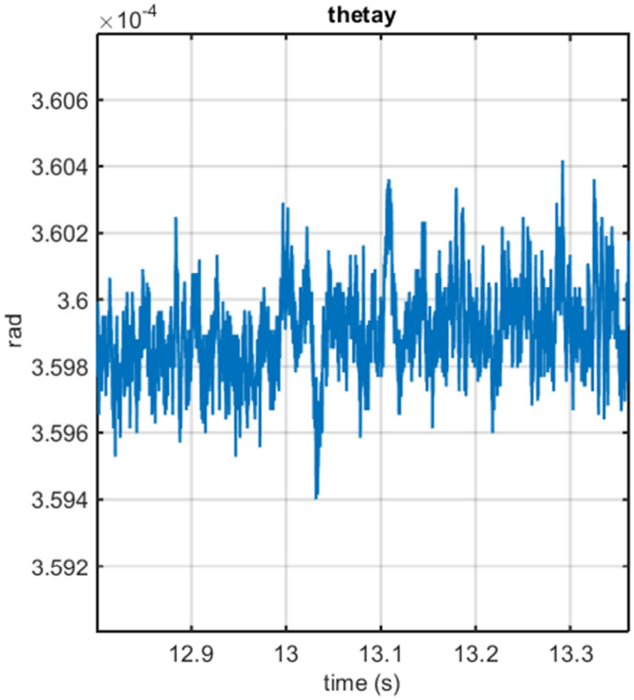

Fig. 4-20 A step of 0.1 µrad in θ_y performed at 13 s.

4.4 Experimental Results in Long-Range Motions

Figures 4-21–4-22 show the trapezoidal position profiles in *X* in the two opposite sides of the initial position of $x = 0$.

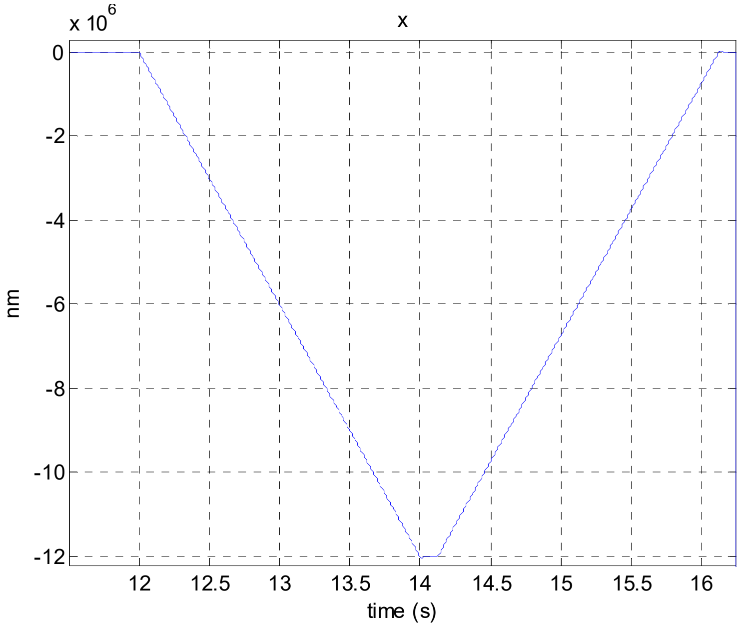

Fig. 4-21 A trapezoidal position response in *X* with the travel range of 12 mm.

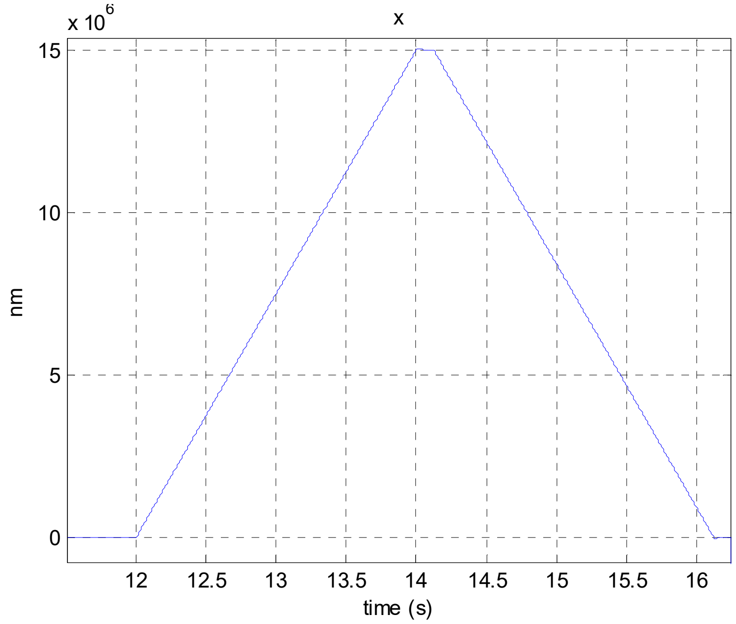

Fig. 4-22 A trapezoidal position response in *X* with the travel range of 15 mm.

Figures 4-23–4-24 present the trapezoidal position responses in *Y* in the two opposite sides of the initial position of $y = 0$. The achieved total travel range is 35.2 mm.

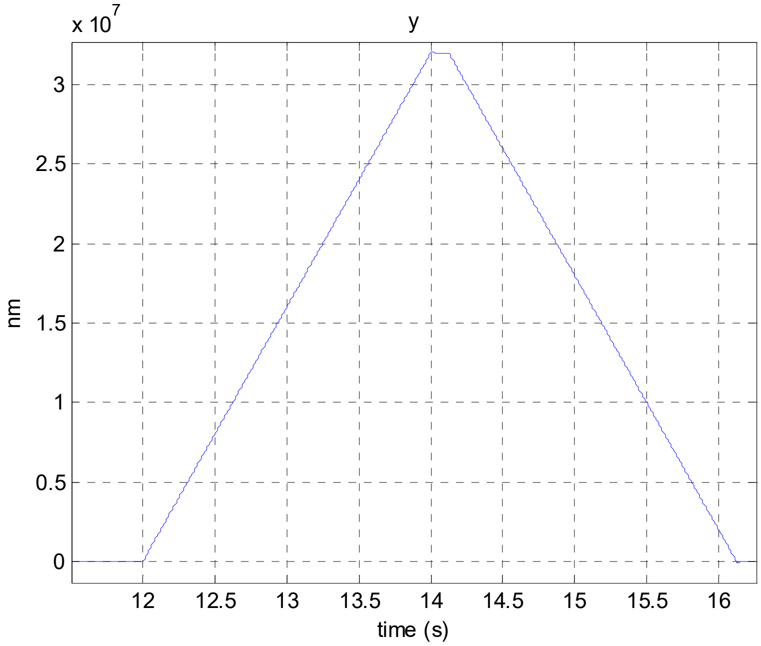

Fig. 4-23 A trapezoidal position response in *Y* with the travel range of 32 mm.

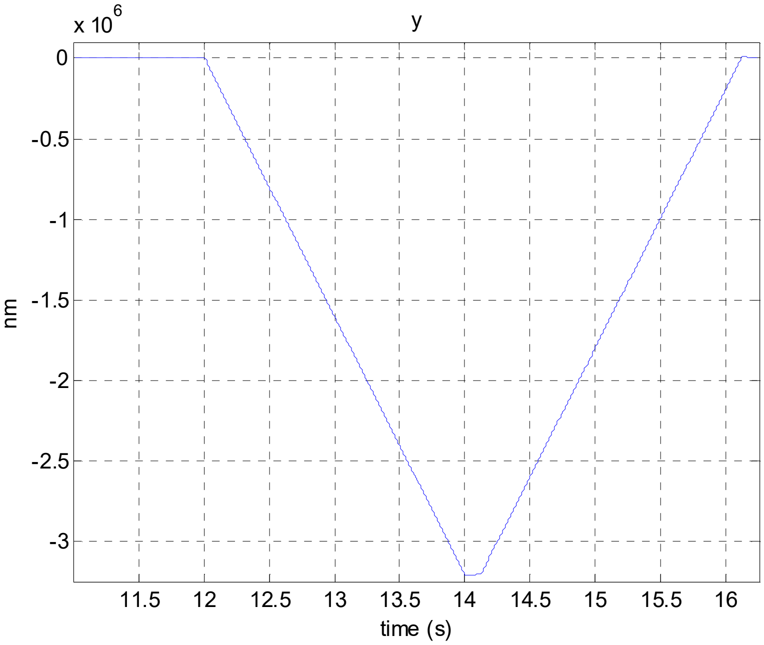

Fig. 4-24 A trapezoidal position response in *Y* with the travel range of 3.2 mm.

Figure 4-25 shows a θ_z trapezoidal position response with the travel range of 1.88 mrad. Figures 4-26–4-27 show the perturbations within 3.5 μm in X and 5 μm in Y, respectively.

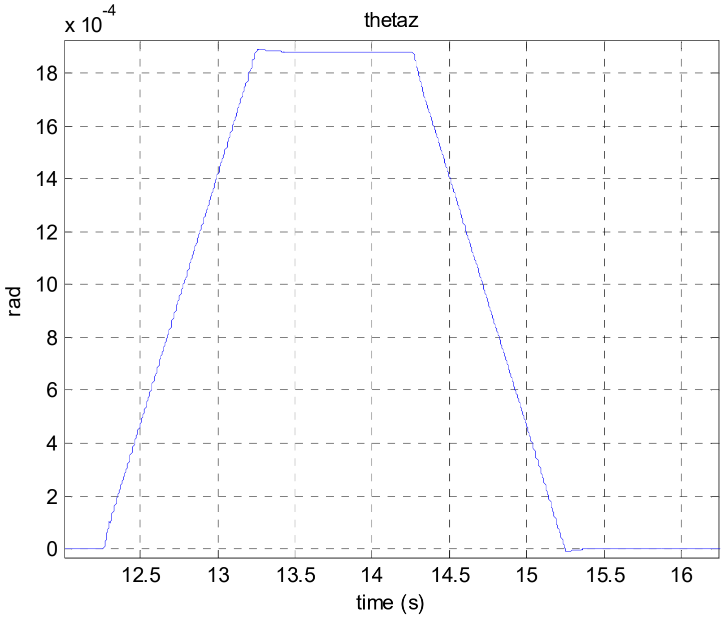

Fig. 4-25 A trapezoidal position response in θ_z with the travel range of 1.88 mrad.

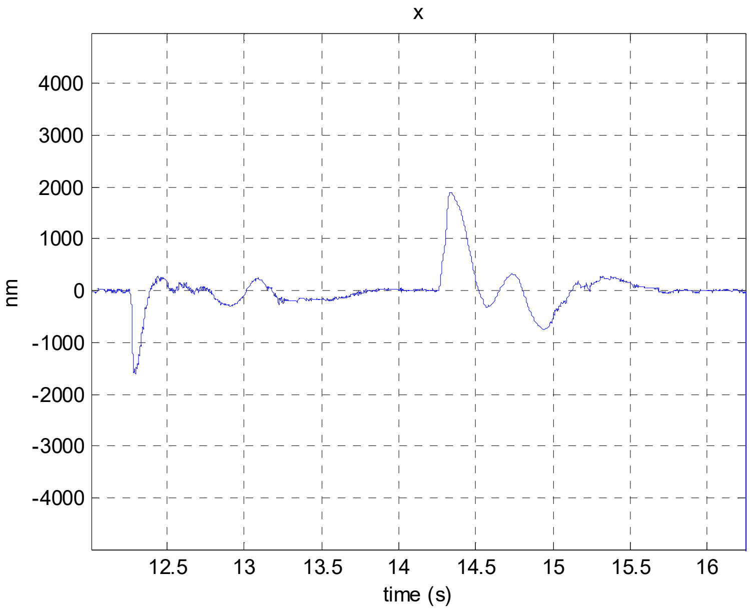

Fig. 4-26 The perturbation in X of the rotations in θ_z shown in Fig. 4-25.

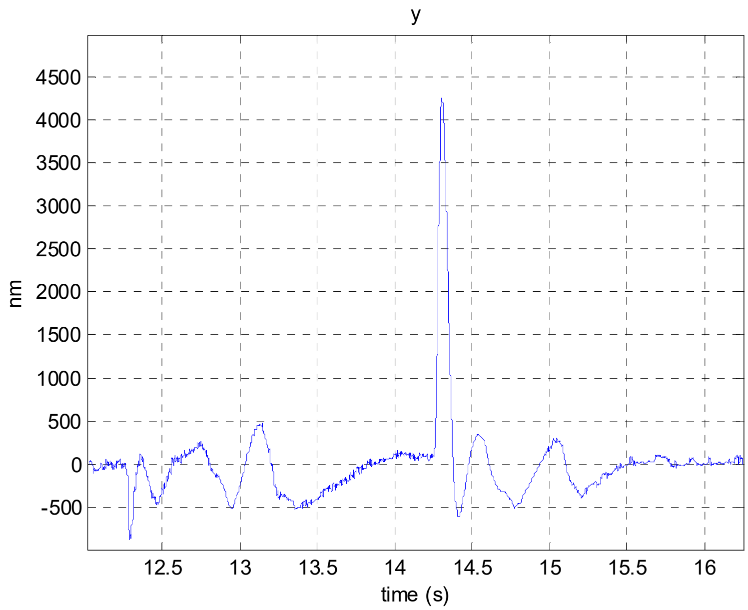

Fig. 4-27 The perturbation in *Y* of the rotations in θ_z shown in Fig. 4-25.

Figure 4-28 presents a θ_z trapezoidal position profile with the travel range of 1.84 mrad. Figures 4-29–4-30 give the perturbations within 4.5 μm in *X* and 1.8 μm in *Y*, respectively. The rotations associated with Figures 4-25 and 28 are performed in the two opposite sides of the initial position at $\theta_z = 0$ mrad. Totally a working range of 3.72 mrad in θ_z is demonstrated in these two experiments.

Figures 4-31–4-32 show θ_x trapezoidal position responses with the travel ranges of 0.32 mrad and 0.20 mrad, respectively. The rotational motions associated with Figures 4-31–4-32 are performed in the two opposite sides of the initial position at $\theta_x = -0.062$ mrad. A total working range of 0.52 mrad is demonstrated in θ_x from these experiments.

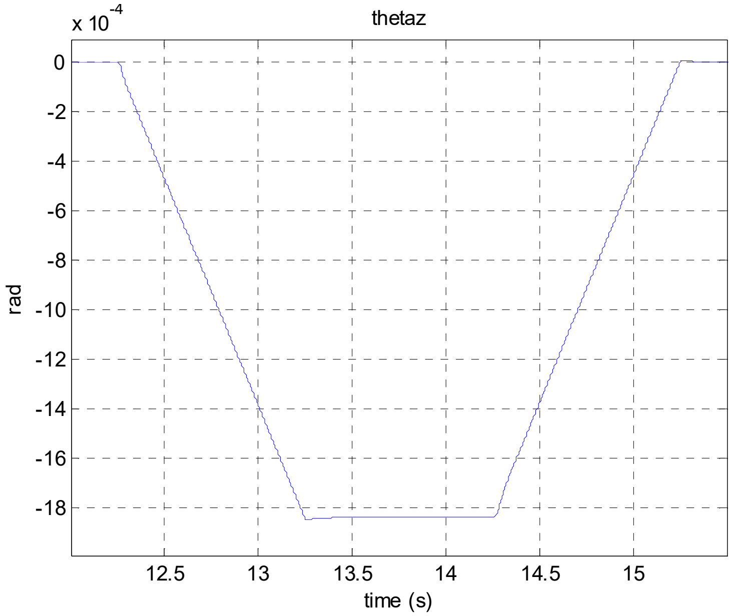

Fig. 4-28 A trapezoidal position response in θ_z with the travel range of 1.84 mrad.

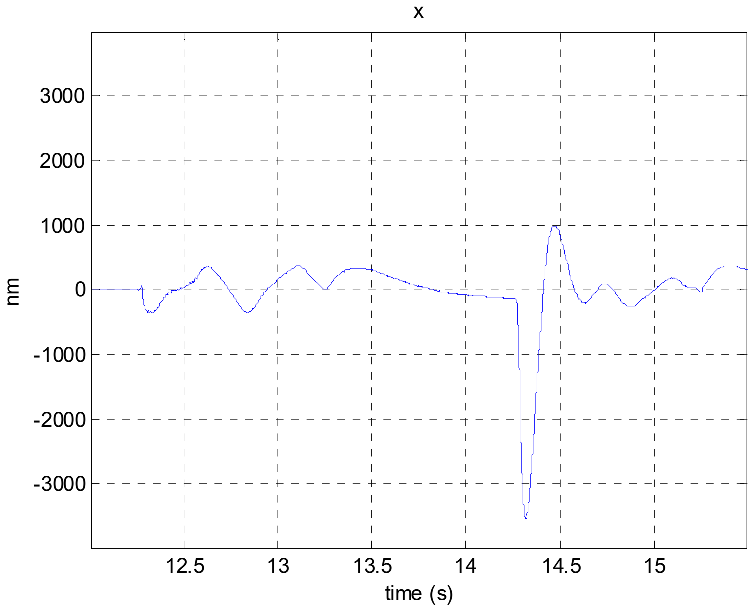

Fig. 4-29 Perturbation in *X* of the rotations in θ_z shown in Fig. 4-28.

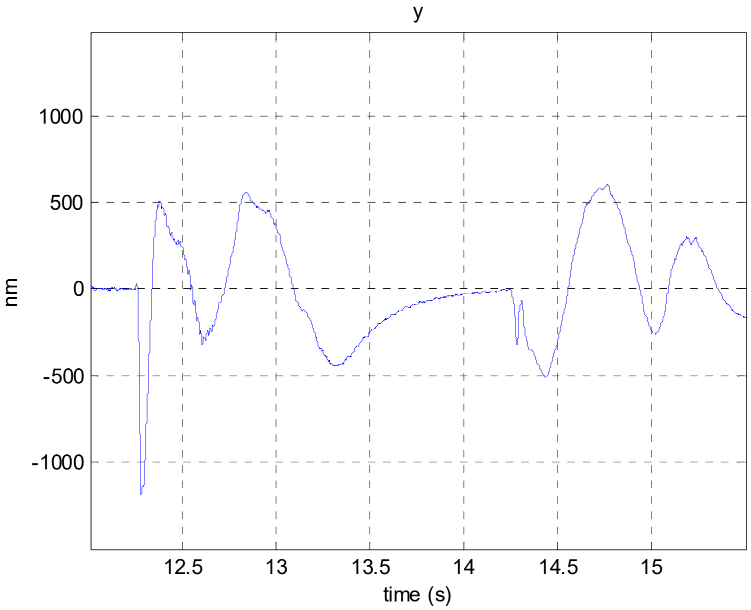

Fig. 4-30 Perturbation in *Y* of the rotations in θ_z shown in Fig. 4-28.

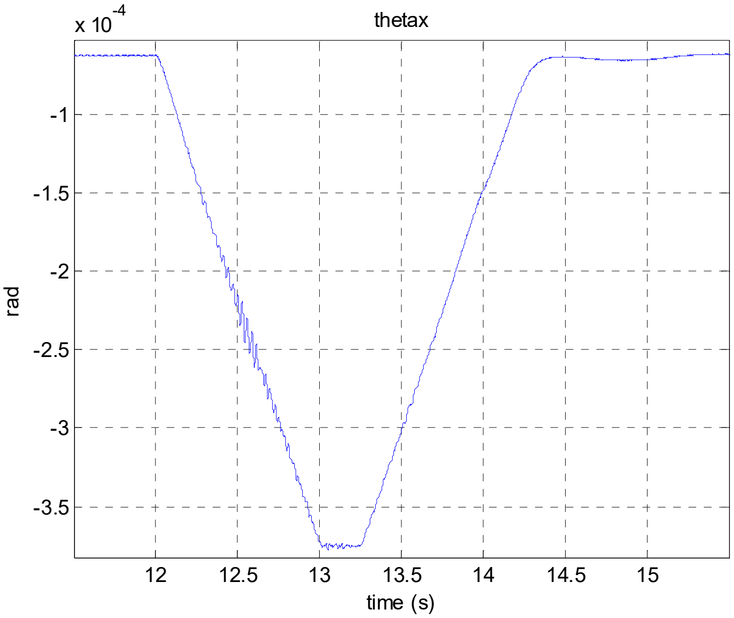

Fig. 4-31 A trapezoidal position response in θ_x with the travel range of 0.32 mrad.

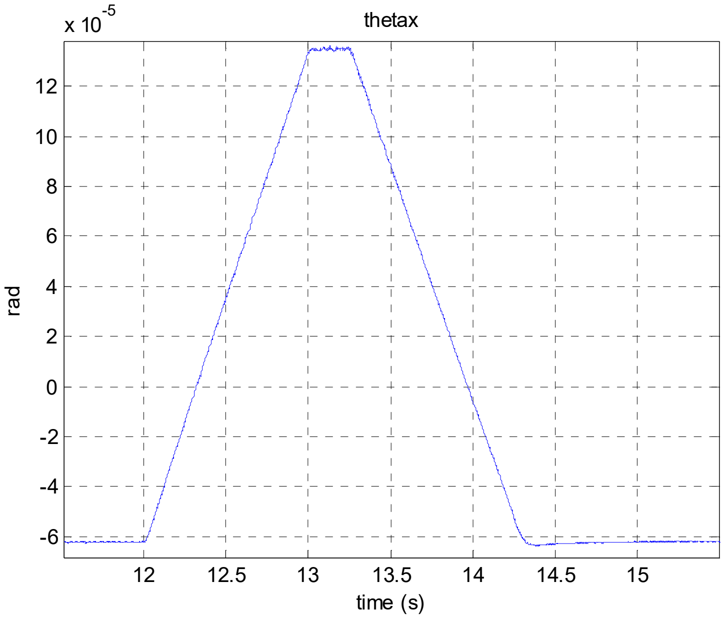

Fig. 4-32 A trapezoidal position response in θ_x with the travel range of 0.20 mrad.

Figures 4-33 gives the position response to demonstrate the maximum travel range of 56 mm in *X* with laser interferometers. Figure 4-34 shows the position response in *Y* where the Hall-effect sensors are used for position feedback in *X*, *Y*, and θ_z. Due to the large position noise from the Hall-effect sensors, which is 6 μm rms, air bearings are used to support the platen against gravity. The achieved travel range is 144 mm in this case.

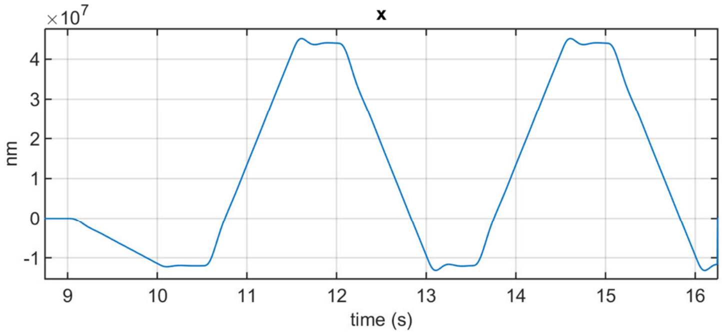

Fig. 4-33 The maximum travel range of 56 mm in *X* with laser interferometers.

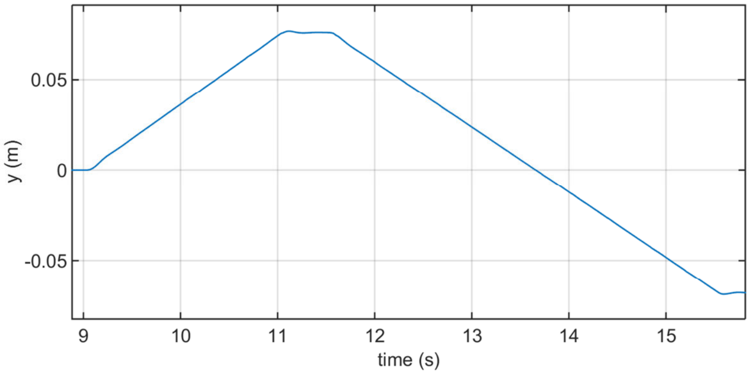

Fig. 4-34 The maximum travel range of 144 mm in *Y* with Hall-effect sensors.

Figure 4-35 shows the work spaces of the moving platen associated with two types of sensors for position feedback, laser interferometers and Hall-effect sensors. The rectangle of 56 mm × 35 mm is the work space of the platen with laser interferometers, where the achieved speed and acceleration are 0.06 m/s and 0.6 m/s^2 with magnetic levitation and 0.15 m/s and 1.5 m/s^2 with air bearings, respectively.

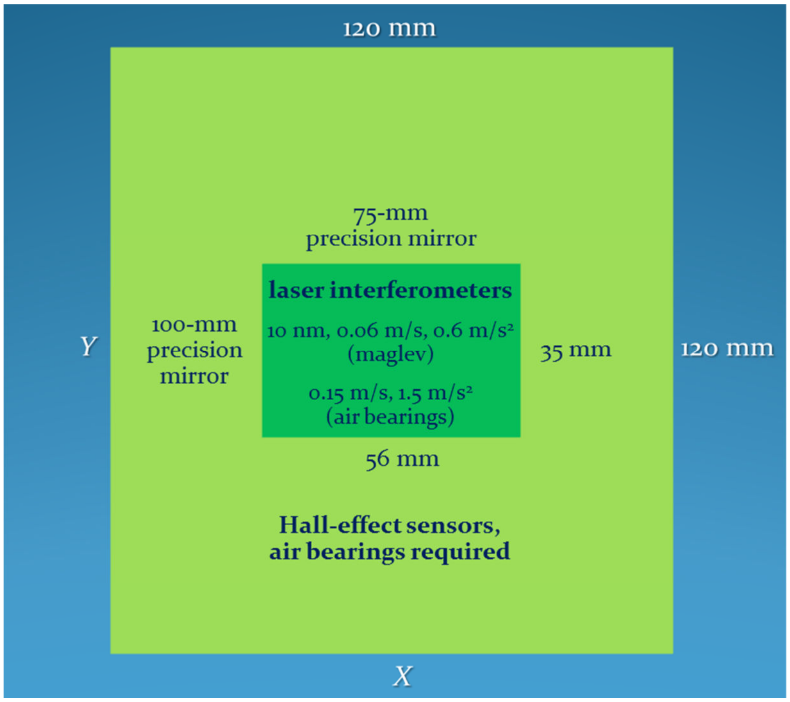

Fig. 4-35. The travel ranges of the platen with two types of sensors and bearings.

In the *XY* plane, the maximum travel range is 144 mm. Due to the structure of the Halback magnet matrix as shown in Fig. 3-1, along each row of the magnet matrix, magnet cubes with different magnetization directions are used to give the resultant superimposition of two orthogonal magnet arrays. This leads to different end effects generated by the four magnet rows in a spatial pitch of the magnet matrix. Therefore, the range in which the Hall-effect sensors give precise position information varies with different rows of magnets along *x* and *y*. This is why the square work space of the platen in the *XY* plane cannot be 144 mm × 144 mm but 120 mm × 120 mm.

With Hall-effect sensors for the position feedback, the peak-to-peak sensing noise, which is 40 μm, is 1000 times larger than that of the laser interferometers. The control bandwidth in *x* and *y* must be significantly smaller than that in the case of laser interferometers presented in Section 4.1.2 so that the output noise stays sufficiently small. Consequently, air bearings must be used to support the platen against its weight. However, with the extended travel ranges in the *XY* plane by the use of Hall-effect sensors, the positioning stage is more applicable in multi-axis precision alignment, manipulation, and assembly.

Figure 4-36 presents the process in which the platen is lifted up from the base through the sequence of steps discussed in part 4.2.1. The vibration seen from 5.4 s through 6.2 s occurred when the control loop in *z* was not closed yet and the platen's vertical position was settling down with the DC control effort. After 11 s, in 6-axis closed-loop control, the platen's position in *z* settled at 39 μm from rest. The positioning noise was then negligible, and the platen was ready for any 6-axis motions.

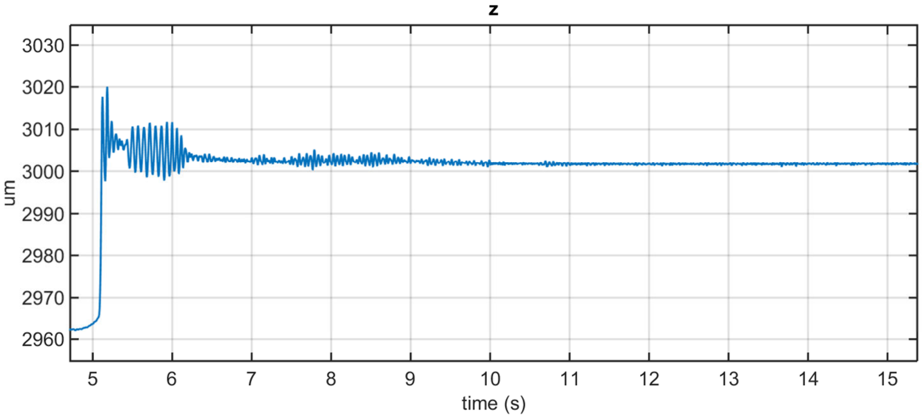

Fig. 4-36 Position response to demonstrate the achieved travel range of 39 µm in Z.

4.5 Responses with Various Step Sizes and Trajectories

In Fig. 4-37, two step responses of –4 µm and 8 µm are performed at the times of 14.5 s and 15.5 s, respectively. The overshoot of the responses is 3.25% and the settling time is within 0.32 s. Figure 4-38 is the plot of three consecutive steps of 2 µm in *Z*. The responses show the damping effects of the cables connected to the moving part and of the DC control effort to levitate the platen up before the closed-loop-control motions are performed. Figure 4-39 gives two consecutive steps of 5 µrad in the rotation about the vertical axis. In Fig. 4-40, there are three consecutive steps of 0.5 µrad and one step of –1.5 µrad in θ_y.

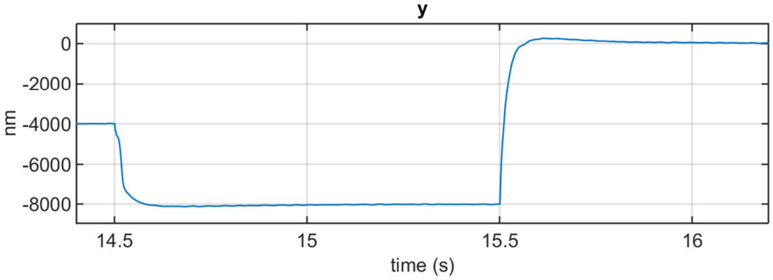

Fig. 4-37 Two steps of 4 µm and 8 µm in *Y*.

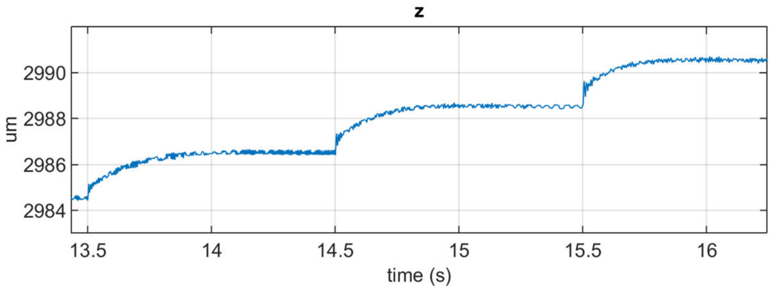

Fig. 4-38 Three consecutive steps of 2 μm in *Z*.

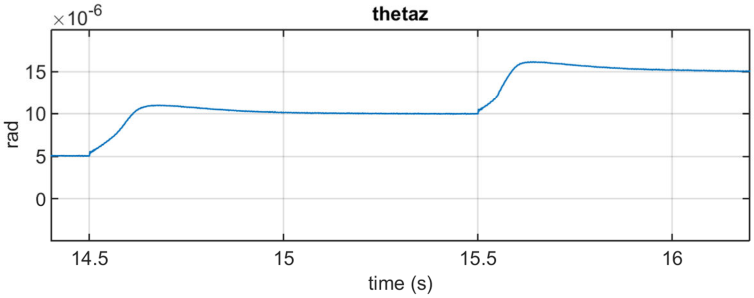

Fig. 4-39 Two consecutive steps of 5 μrad in θ_z.

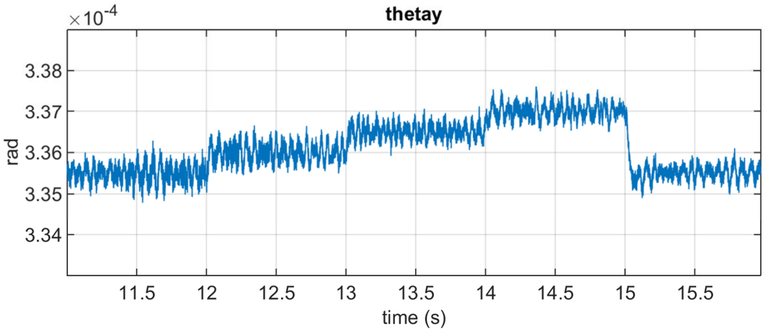

Fig. 4-40 Three steps of 0.5 μrad and one step of –1.5 μrad in θ_y.

Figure 4-41 exhibits the position profiles in all six axes in magnetic levitation where two circular motions with the dimeter of 6 mm were performed in the *xy* plane. Right after the completion of the first circular motion, at 14 s, the maglev stage was paused for 0.125 s. The perturbations in θ_z, θ_x, θ_y, and *z* are within 50 μrad, 290 μrad, 430 μrad, and 20 μm, respectively.

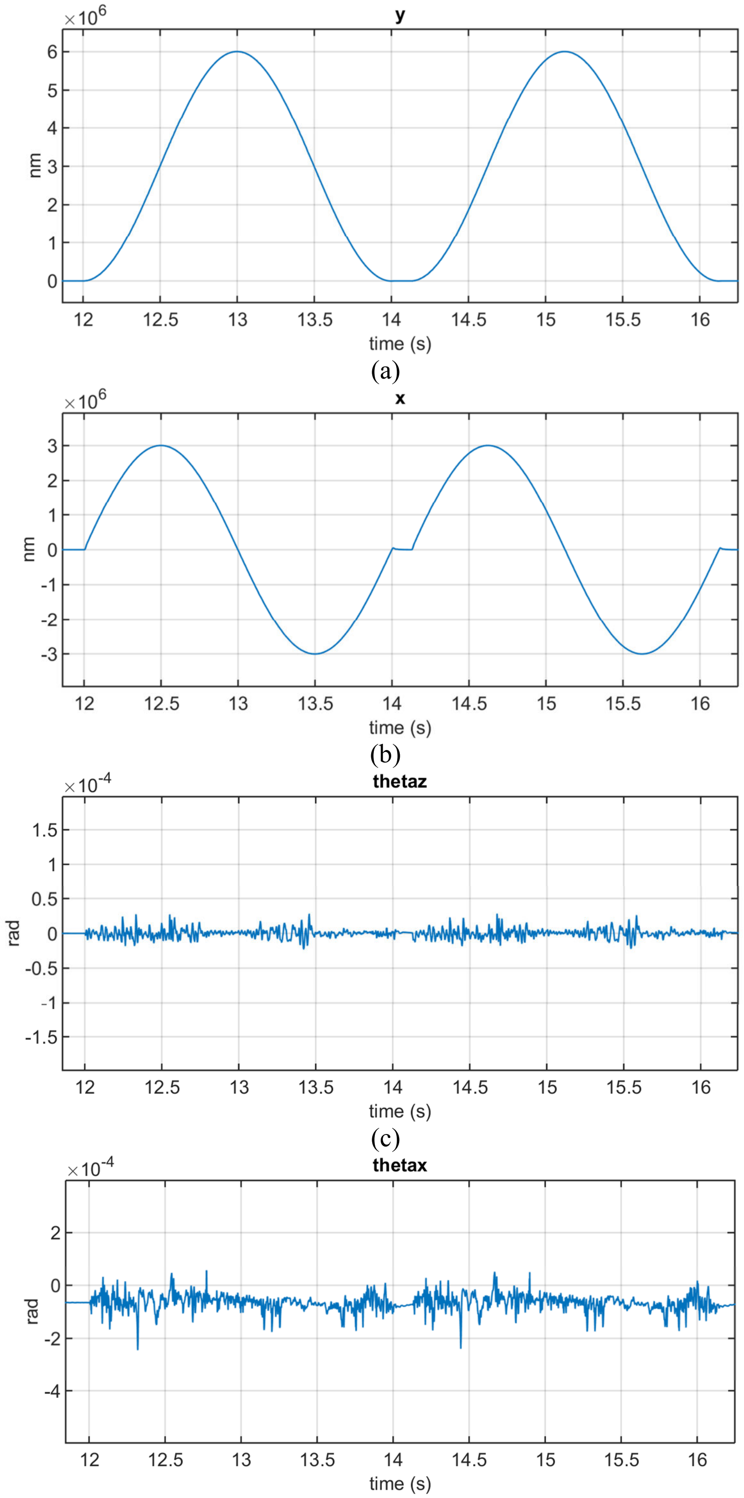

(a)

(b)

(c)

(d)

Fig. 4-41 Two circular motions with the diameter of 6 mm in the *xy* plane and the perturbations.

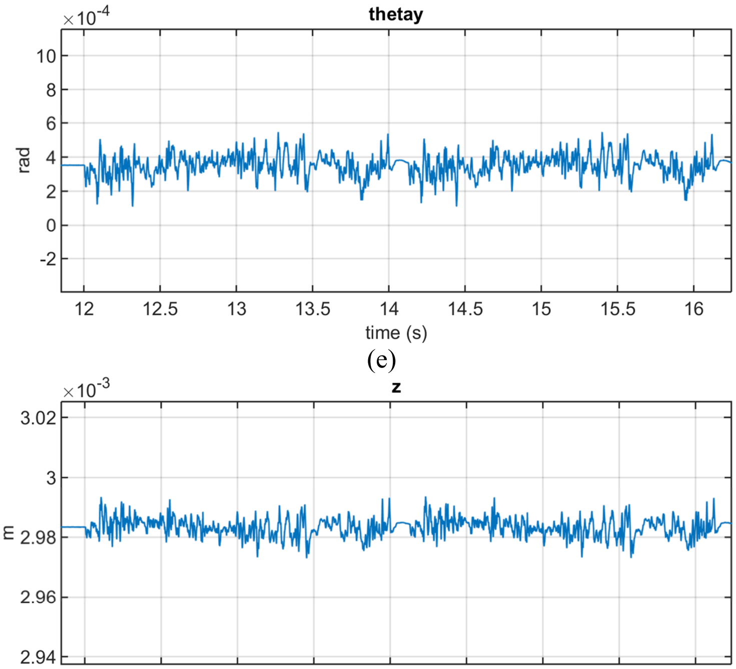

(e)

(f)

Fig. 4-41 Continued.

4.6 Experimental Results in the Achieved Speed and Acceleration

In Fig. 4-42(a), the position response of the moving platen in the experiment to determine the maximum speed and acceleration in magnetic levitation is given. During the translational motion in the time frame from 12.5 s to 12.8 s, trapezoidal-velocity input shaping is introduced to the *X*-axis. The travel range is 12 mm. The achieved speed and acceleration in the horizontal plane is 0.06 m/s and 0.6 m/s^2, respectively. Figure 4-42(b) shows the position response in *x* for the achieved velocity and acceleration when the platen is supported by the air bearings, which are 0.15 m/s and 1.5 m/s^2, respectively.

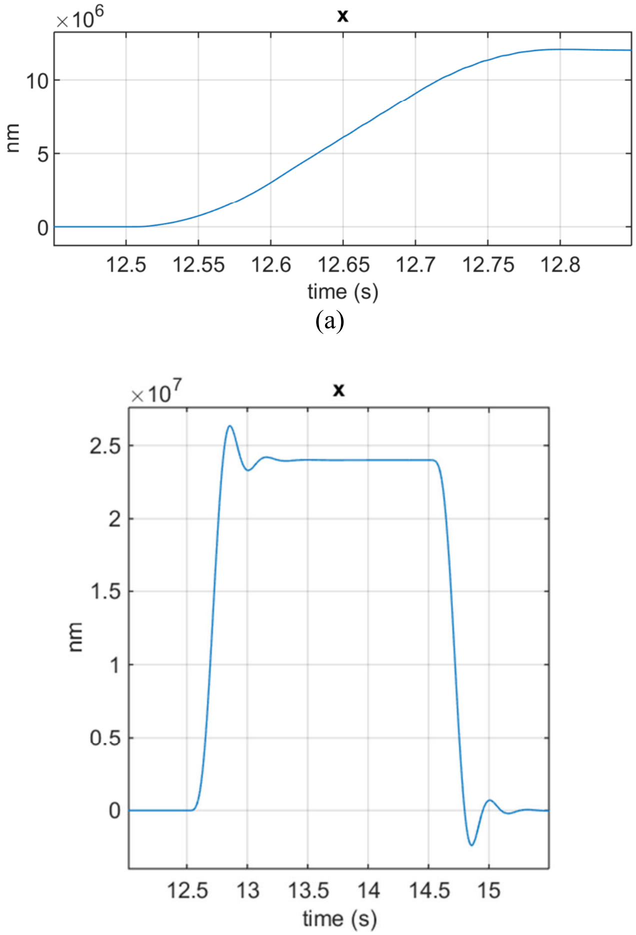

(a)

(b)

Fig. 4-42 Position profile in x to determine the achieved speed and acceleration of the platen with (a) magnetic levitation and (b) air bearings.

4.7 Load Tests

Figures 4-43–4-45 show the position profiles in z, θ_x, and θ_y of an experiment in which a load of 539.6 g was added to the moving platen. With this added mass, the system models in x, y, and θ_{xy} changed, leading to higher peaks of the associated closed-loop transfer functions' gains. This resulted in the increased positioning noise when the loaded platen moved up in z. However, the controllers effectively drove the positions of the platen to the initial set points.

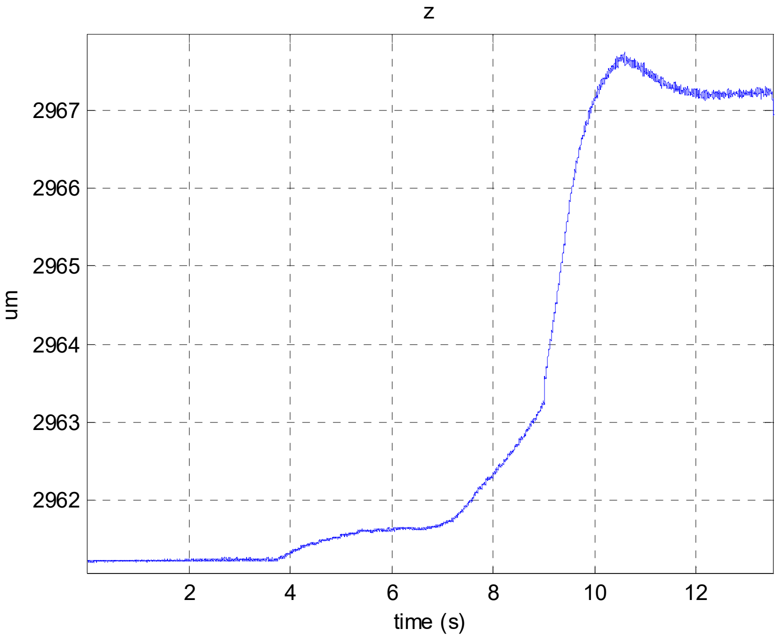

Fig. 4-43 The position response in Z in an experiment to lift up a load of 539.6 g.

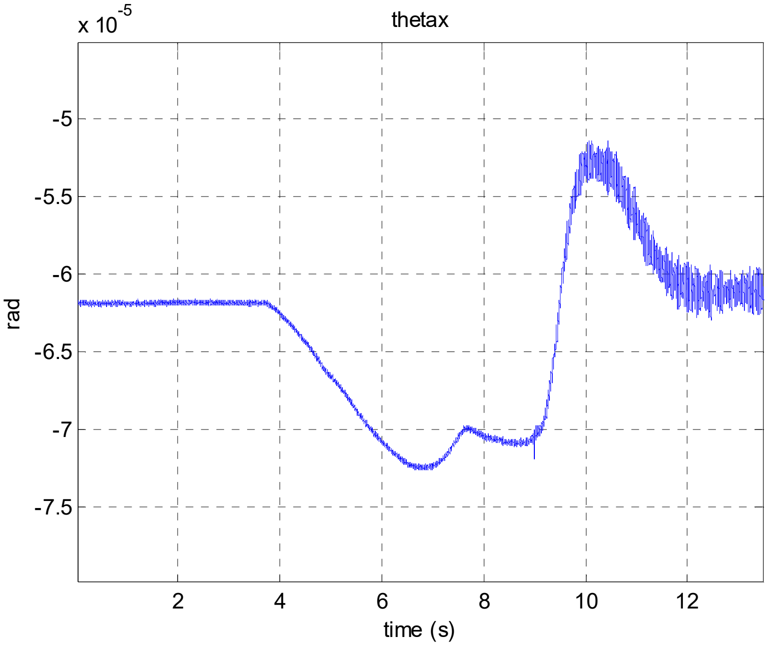

Fig. 4-44 The position response in θ_x in an experiment to lift up a load of 539.6 g.

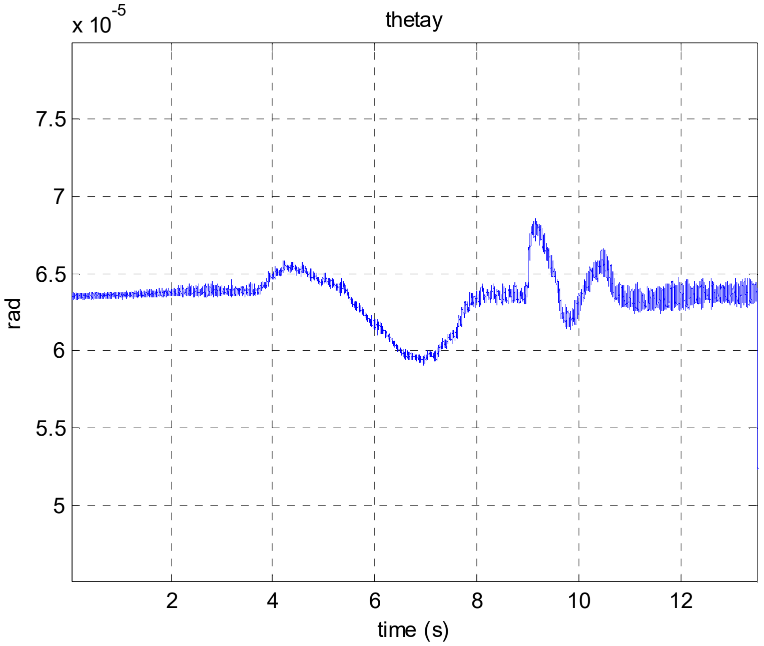

Fig. 4-45 The position response in θ_y in an experiment to lift up a load of 539.6 g.

In another experiment, a load of 579.6 g is added to the moving platen. It can be seen in Figs. 4-46–4-48 that the positions of the moving platen in z, θ_x, and θ_y can no longer be driven to the position references.

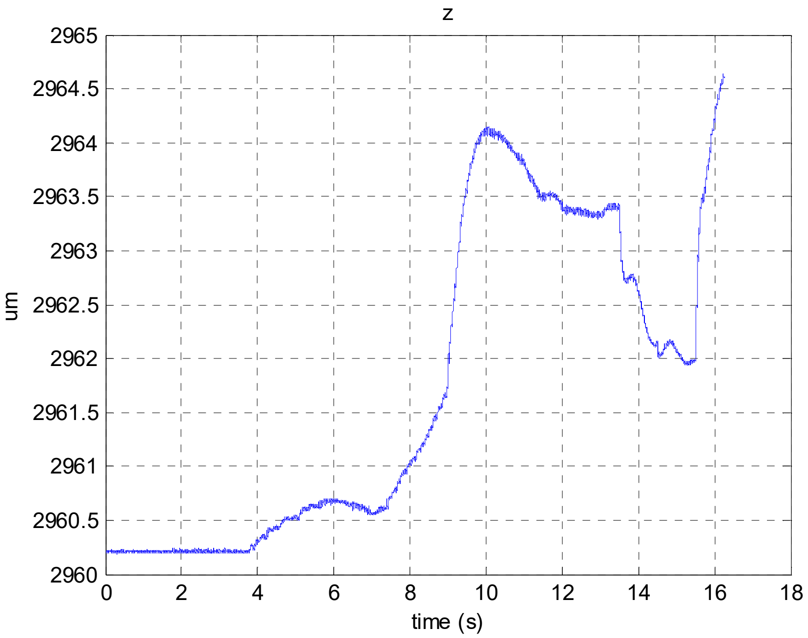

Fig. 4-46 The position profile in z in an experiment to lift up a load of 579.6 g.

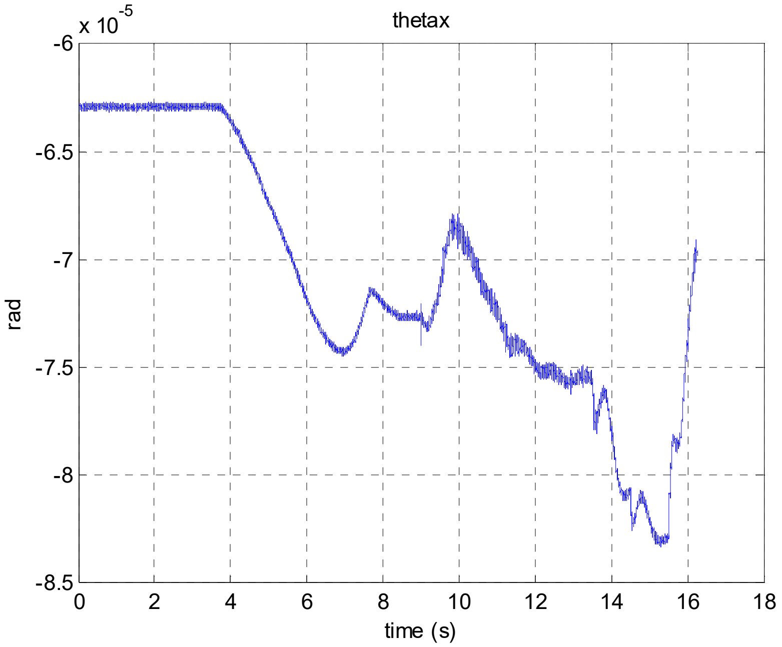

Fig. 4-47 The position profile in θ_x in an experiment to lift up a load of 579.6 g.

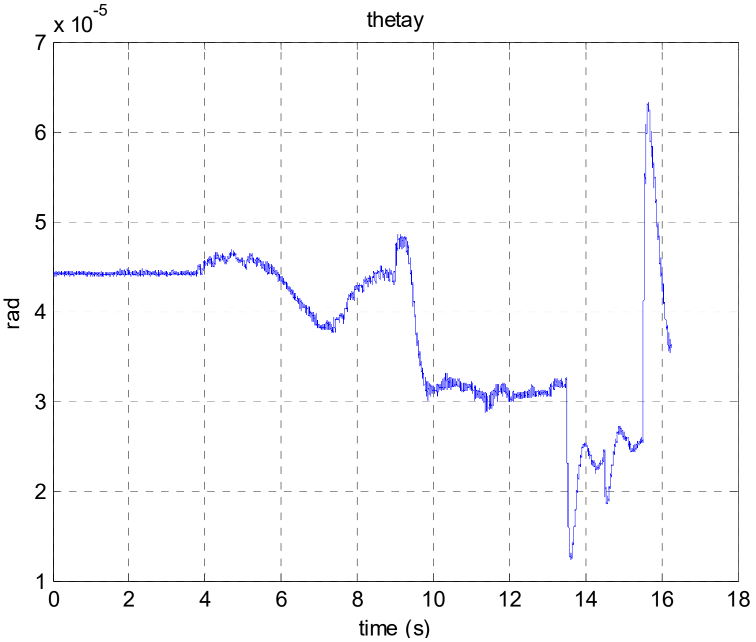

Fig. 4-48 The position profile in θ_y in an experiment to lift up a load of 579.6 g.

CHAPTER V

CONCLUSIONS AND SUGGESTED FUTURE WORK

5.1 Conclusions

In this work, a universal framework of 2-phase Lorentz coils working with a linear Halbach magnet array or matrix was proposed and analyzed. The key features of the Halbach array or matrix are that it focuses the magnetic flux in one side of its structure and generates a perfectly sinusoidal magnetic flux density on a plane parallel to the magnet array's surface. The 2-phase Lorentz coils were designed to take the advantage of the sinusoidal variance of the magnetic flux density so that the Lorentz forces acting on the two sides of each coil are equal to strengthen the resultant force and to simplify the force calculation. At least two coils are needed in each direction to guarantee the force generation capability at any point in the horizontal axis. The force calculation was implemented by volume integration with the pre-calculated field solution of the Halbach magnet array. The Lorentz force acting on each planar coil was calculated to be sinusoidally dependent on position providing that the gap between the coil and the magnet array is uniform and constant. The analytical Lorentz-force calculation was verified by an FEM. This universal framework is highly applicable in precision linear PM machines and multi-axis stages used in the positioning systems that require high positioning resolution, speed, and acceleration.

A 6-DOF maglev stage was developed in this work to verify the above-mentioned theoretical framework experimentally. The planar positioning stage is a moving-coil design with a platen moving over a superimposed concentrated-field Halbach magnet matrix. The single moving part comprises of a Delrin plastic frame, four 2-phase overlapped Lorentz coils arranged in a cross configuration, and the precision mirrors for laser interferometer position sensing. In the moving platen, there are three laser displacement sensors to measure the out-of-plane positions and two 2-axis Hall-effect sensors for planar positioning when the laser interferometers are not available. Achieved performance specifications include 10 nm positioning resolution in the horizontal plane and in the vertical axis, 1 μrad positioning resolution in the rotation about the vertical axis, 0.1 μrad positioning resolution in the out-of-plane rotations, 35.2 mm maximum travel range in y, 56 mm maximum travel range in x, 39 μm travel range in z, 6 cm/s translational speed in the horizontal plane, and 0.6 m/s^2 acceleration. With Hall-effect sensors for position feedback and air bearings to support the platen, the maximum travel range in the XY plane was extended to 144 mm. The 6-DOF maglev stage developed herein is highly applicable in nano-precision stepping, scanning, manipulation, and positioning systems.

5.2 Future Work

In the framework of 2-phase Lorentz coils with a linear Halbach array, the Halbach arrays can be attached to the moving part while the Lorentz coils are fixed to the stationary frame. This would help avoid the force disturbance from the power cables connected to the moving platen.

Additional suggested future work includes design and testing of the controllers for the positioning stage to move in a lager travel range in the vertical axis, improving the maximum speed and acceleration in the horizontal plane, improving the positioning resolution in *x* and *y* to achieve 5 nm consistently. With the capability of the moving platen to carry a 540-gram load, longer precision mirrors can be fixed to the platen to extend the travel ranges in *x* and *y*.

In controller design, adaptive control can be designed so that the capability of the platen to reject the force disturbance and attenuate the positioning noise is maintained with varying loads. This will be of significance when the maglev stage is used in high-precision assembly or conveyor applications.

Regarding the possible integration of the maglev positioning stage developed herein in other research, this stage can be part of a setup that has a 2D color plate on top of the mirror-finished aluminum surface to develop a color sensing system for planar positioning. The positioning stage presented herein can also be part of a micro-and-nano scratching or indentation system where back-and-forth relative motions between a scratching tool and a substrate create the groves on the substrate with the smallest feature sizes in the micrometer or nanometer scale.

REFERENCES

[1] W.-J. Kim, “High-precision planar magnetic levitation,” Ph.D. dissertation, Massachusetts Institute of Technology, Cambridge, MA, Jun. 1997.

[2] F. Ayela, J. Chaussy, T. Fournier, and E. Menegaz, “A micromachined actuator for nanopositioning in two dimensions,” *Sensors and Actuators A: Physical*, vol. 76, no. 1–3, pp. 459–462, Aug. 1999.

[3] V. Snitka, “Ultrasonic actuators for nanometre positioning,” *Ultrasonics*, vol. 38, no. 1–8, pp. 20–25, Mar. 2000.

[4] W. Gao, S. Dejima, H. Yanai, K. Katakura, S. Kiyono, and Y. Tomita, “A surface motor-driven planar motion stage integrated with an XYθZ surface encoder for precision positioning,” *Precision Engineering*, vol. 28, no. 3, pp. 329–337, Jul. 2004.

[5] S. Verma, W.-J. Kim, and J. Gu, “Six-axis nanopositioning device with precision magnetic levitation technology,” *IEEE/ASME Trans. Mechatronics*, vol. 9, no. 2, pp. 384–391, Jun. 2004.

[6] T. Hu and W.-J. Kim, “Extended range six-DOF high-precision positioner for wafer processing,” *IEEE/ASME Trans. Mechatronics*, vol 11, no. 6, pp. 682–689, Dec. 2006.

[7] W.-J. Kim and S. Verma, “Multiaxis maglev positioner with nanometer resolution over extended travel range,” *ASME Journal of Dynamic Systems, Measurement, and Control*, vol. 129, no. 6, pp. 777–785, Jan. 2007.

[8] Z. Zhang and C.-H. Menq, “Six-axis magnetic levitation and motion control,” *IEEE Trans. Robotics*, vol. 23, no. 2, pp. 196–205, Apr. 2007.

[9] Q. Yao, J. Dong, and P. M. Ferreira, “A novel parallel-kinematics mechanisms for integrated, multi-axis nanopositioning: Part 1. Kinematics and design for fabrication,” *Precision Engineering*, vol 32, no. 1, pp. 7–19, Jan. 2008.

[10] Q. Yao, J. Dong, and P. M. Ferreira, “A novel parallel-kinematics mechanisms for integrated, multi-axis nanopositioning: Part 2. Dynamics, control and performance analysis,” *Precision Engineering*, vol. 32, no. 1, pp. 20–33, Jan. 2008.

[11] Y. K. Yong, S. S. Aphale, and S.O.R. Moheimani, “Design, identification, and control of a flexure-based XY stage for fast nanoscale positioning,” *IEEE Trans. Nanotechnology*, vol. 8, no. 1, pp. 46–54, Jan. 2009.

[12] S. Polit and J. Dong, “Development of a high-bandwidth *XY* nanopositioning stage for high-rate micro-/nanomanufacturing,” *IEEE/ASME Trans. Mechatronics,* vol. 16, no. 4, pp. 724–733, Aug. 2011.

[13] H. Shinno, H. Yoshioka, and H. Sawano, “A newly developed long range positioning table system with a sub-nanometer resolution,” *CIRP Annals - Manufacturing Technology*, vol. 60, no. 1, pp. 403-406, Apr. 2011.

[14] R. Fesperman, O. Ozturk, R. Hocken, S. Ruben, T.-C. Tsao, J. Phipps, T. Lemmons, J. Brien, and G. Caskey, “Multi-scale alignment and positioning system–MAPS,” *Precision Engineering*, vol. 36, pp. 517–537, Oct. 2012.

[15] L. Juhász and J. Maas, “Control of hybrid nanopositioning systems for trajectory-tracking applications,” *Mechatronics*, vol. 23, no. 6, pp. 617–629, Jul. 2013.

[16] Q. Xu, “Design and development of a compact flexure-based XY precision positioning system with centimeter range,” *IEEE Trans. Industrial Electronics*, vol. 61, no. 2, pp. 893–903, Feb. 2014.

[17] Aerotech Inc. (2015). [Online]. Available: http://www.aerotech.com/product-catalog/stages.

[18] Physik Instrumente. (2015). [Online]. Available: http://www.pi-usa.us/products.

[19] G. Schitter, K. J. Åström, B. E. DeMartini, P. J. Thurner, K. L. Turner, and P. K. Hansma, “Design and modeling of a high-speed AFM-scanner,” *IEEE Trans. Control Systems Technology*, vol. 15, no. 5, pp. 906–915, Sep. 2007.

[20] G. K. Parmar, “Dynamics and control of flexure-based large range nanopositioning systems,” Ph.D. dissertation, University of Michigan, Ann Arbor, 2014.

[21] A. Zehden, “Electric traction apparatus,” U.S. Patent 782,312, Feb. 14, 1905.

[22] A. Zehden, “Electric traction apparatus,” U.S. Patent 12,700, Oct. 1, 1907.

[23] R. P. Geoffrey, “Magnetic system of transportation,” U.S. Patent 3,158,765, Nov. 24, 1964.

[24] S. Yamamura, “Magnetic levitation technology of tracked vehicles present status and prospects,” *IEEE Trans. Magnetics*, vol. 12, no. 6, pp.874 878, Nov. 1976.

[25] S. L. Wipf, "Magnetic suspension system," U.S. Patent 3,589,300, Jun. 29, 1971.

[26] J. A. Ross, "Feedback control circuit for magnetic suspension and propulsion system," U.S. Patent 3,736,880, Jun. 5, 1973.

[27] R. L. Byer, R. F. Begley, and G. R. Stewart, "Superconducting, magnetically levitated merry-go-round," *American Journal of Physics*, vol. 42, no. 2, pp. 111–125, 1974.

[28] W. Kortum and A. Utzt, "Control law design and dynamic evaluations for a MAGLEV vehicle with a combined lift and guidance suspension system," *American Control Conference*, pp. 276–282, Jun. 1983.

[29] P. K. Sinha, "Design of a magnetically levitated vehicle," *IEEE Trans. Magnetics*, vol. 20, no. 5, pp. 1672–1674, Sep. 1984.

[30] Y.-J. Kim, P.-S. Shin, D.-H. Kang, and Y.-H. Cho, "Design and analysis of electromagnetic system in a magnetically levitated vehicle, KOMAG-01," *IEEE Trans. Magnetics*, vol. 28, no. 5, pp. 3321–3323, Sep. 1992.

[31] D. Cho, Y. Kato, D. Spilman, "Sliding mode and classical controllers in magnetic levitation systems," *IEEE Control Systems Magazine*, vol. 13, no. 1, pp. 42–48, Feb. 1993.

[32] T. Saitoh, N. Maki, T. Kobayashi, M. Shibata, and T. Takizawa, "Electromagnetic force and eddy current loss in dynamic behavior of a superconducting magnetically levitated vehicle," *IEEE Trans. Applied Superconductivity*, vol. 3, no. 1, pp. 417–420, Mar. 1993.

[33] I. Takahashi and Y. Ide, "Decoupling control of thrust and attractive force of a LIM using a space vector control inverter," *IEEE Trans. Industry Applications*, vol. 29, no. 1, pp. 161–167, Jan./Feb. 1993.

[34] R. F. Post, "Magnetic levitation system for moving objects," U.S. Patent 5,722,326, Mar. 3, 1998.

[35] C.-T. Liu and S.-Y. Lin, "An orthogonal control scheme of linear switched-reluctance motor for magnetic levitated vehicle applications," in *Power Engineering Society Winter Meeting*, vol. 1, pp. 249–252, 2000.

[36] D. H. Kang and H. Weh, "Design of an integrated propulsion, guidance, and levitation system by magnetically excited transverse flux linear motor (TFM-LM)," *IEEE Trans. Energy Conversion*, vol. 19, no. 3, pp. 477–484, Sept. 2004.

[37] H. H. van den Bergh, R. Kratz, and P. L. Jeter, "Magnetic levitation and propulsion system," U.S. Patent 6,827,022 B2, Dec. 7, 2004.

[38] D. Rogg, "General survey of the possible applications and development tendencies of magnetic levitation technology," *IEEE Trans. Magnetics*, vol. 20, no. 5, pp. 1696–1701, Sep. 1984.

[39] A. R. Eastham and W. F. Hayes, "Maglev systems development status," *IEEE Aerospace and Electronic Systems Magazine,* vol. 3, no. 1, pp. 21–30, Jan. 1988.

[40] M. Ono, S. Koga, and H. Ohtsuki, "Japan's superconducting Maglev train," *IEEE Instrumentation & Measurement Magazine*, vol. 5, no. 1, pp. 9–15, Mar. 2002.

[41] D. M. Rote and Y. Cai, "Review of dynamic stability of repulsive-force maglev suspension systems," *IEEE Trans. Magnetics*, vol. 38, no. 2, pp. 1383–1390, Mar. 2002.

[42] H.-W. Lee, K.-C. Kim, and J. Lee, "Review of maglev train technologies," *IEEE Trans. Magnetics*, vol. 42, no. 7, pp. 1917–1925, Jul. 2006.

[43] R. Hellinger and P. Mnich, "Linear motor-powered transportation: History, present status, and future outlook," *Proceedings of the IEEE* , vol. 97, no. 11, pp. 1892–1900, Nov. 2009.

[44] Guinness World Records. (2015). [Online]. Available: http://www.guinnessworldrecords.com/world-records/fastest-maglev-train.

[45] F. Matsumura and T. Yoshimoto, "System modeling and control design of a horizontal-shaft magnetic-bearing system," *IEEE Trans. Magnetics*, vol. 22, no. 3, pp. 196–203, May 1986.

[46] M. Ooshima, A. Chiba, T. Fukao, and M. A. Rahman, "Design and analysis of permanent magnet-type bearingless motors," *IEEE Trans. Industrial Electronics*, vol. 43, no. 2, pp. 292–299, Apr. 1996.

[47] J. D. Lindlau and C. R. Knospe, "Feedback linearization of an active magnetic bearing with voltage control," *IEEE Trans. Control Systems Technology*, vol. 10, no. 1, pp. 21–31, Jan. 2002.

[48] P. Karutz, T. Nussbaumer, W. Gruber, and J. W. Kolar, "Novel magnetically levitated two-level motor," *IEEE/ASME Trans. Mechatronics*, vol. 13, no. 6, pp. 658–668, Dec. 2008.

[49] C.-T. Liu, Y.-Y. Yang, and S.-Y. Lin, "Online realizations of dynamic gap detection and control for levitated industrial steel-plate conveyance system," *IEEE Trans. Industry Applications*, vol. 49, no. 5, pp. 1946–1953, Sept./Oct. 2013.

[50] M. Mofushita, T. Azukizawa, S. Kanda, N. Tamura, and T. Yokoyama, "A new maglev system for magnetically levitated carrier system," *IEEE Trans. Vehicular Technology*, vol. 38, no. 4, pp. 230–236, Nov. 1989.

[51] M. Fabbri, P. L. Ribani, and D. Zuffa, "Design and testing of a magnetically levitated conveyor," *IEEE Trans. Magnetics*, vol. 49, no. 1, pp. 577–585, Jan. 2013.

[52] S. R. Oh, R. L. Hollis, and S. E. Salcudean, "Precision assembly with a magnetically levitated wrist," in *Proc. IEEE International Conference on Robotics and Automation,* vol. 1, pp. 127–134, May 1993.

[53] D. L. Trumper, W.-J. Kim, and M. E. Williams, "Design and analysis framework for permanent-magnet machines," *IEEE Trans. Industry Applications*, vol. 32, no. 2, pp. 371–379, Mar./Apr. 1996.

[54] W.-J. Kim, D. L. Trumper, and J. H. Lang, "Modeling and vector control of planar magnetic levitator," *IEEE Trans. Industry Applications*, vol. 34, no. 6, pp. 1254–1262, Nov./Dec. 1998.

[55] R. L. Hollis, S. E. Salcudean, and A. P. Allan, "A six-degree-of-freedom magnetically levitated variable compliance fine-motion wrist: design, modeling, and control," *IEEE Trans. Robotics and Automation*, vol **7,** no. 3, pp. 320–332, Jun. 1991.

[56] C. Fulford and M. Maggiore, "Control of a 5DOF magnetically levitated positioning stage," *IEEE Trans. Control Systems Technology*, vol. 17, no. 4, pp. 844–852, Jul. 2009.

[57] S. E. Salcudean, N. M. Wong, and R. L. Hollis, "Design and control of a force-reflecting teleoperation system with magnetically levitated master and wrist," *IEEE Trans. Robotics and Automation*, vol. 11, no. 6, pp. 844–858, Dec. 1995.

[58] P. Berkelman and M. Dzadovsky, "Magnetic levitation over large translation and rotation ranges in all directions," *IEEE Trans. Mechatronics*, vol. 18, no. 1, pp. 44–52, Feb. 2013.

[59] M. B. Khamesee, N. Kato, Y. Nomura, and T. Nakamura, "Design and control of a microrobotic system using magnetic levitation," *IEEE/ASME Trans. Mechatronics*, vol. 7, no. 1, pp. 1–14, Mar. 2002.

[60] M. P. Kummer, J. J. Abbott, B. E. Kratochvil, R. Borer, A. Sengul, and B. J. Nelson, "OctoMag: An electromagnetic system for 5-DOF wireless micromanipulation," *IEEE Trans. Robotics*, vol. 26, no. 6, pp. 1006–1017, Dec. 2010.

[61] M. E. Hoque, M. Takasaki, Y. Ishino, and T. Mizuno, "Development of a three-axis active vibration isolator using zero-power control," *IEEE/ASME Trans. Mechatronics*, vol. 11, no. 4, pp. 462–470, Aug. 2006.

[62] B. P. Mann, and N. D. Sims, "Energy harvesting from the nonlinear oscillations of magnetic levitation," *Journal of Sound and Vibration*, vol. 319, no. 1–2, pp. 515–530, Jan. 2009.

[63] L. Liu, and F. G. Yuan, "Diamagnetic levitation for nonlinear vibration energy harvesting: Theoretical modeling and analysis," *Journal of Sound and Vibration*, vol. 332, no. 2, pp. 455–464, Jan. 2013.

[64] D. F. Berdy, D. J. Valentino, and D. Peroulis, "Kinetic energy harvesting from human walking and running using a magnetic levitation energy harvester," *Sensors and Actuators A: Physical*, vol. 222, pp. 262–271, Feb. 2015.

[65] S. Palagummi, and F. G. Yuan, "An optimal design of a mono-stable vertical diamagnetic levitation based electromagnetic vibration energy harvester," *Journal of Sound and Vibration*, vol. 342, pp. 330–345, Apr. 2015.

[66] D. L. Trumper, M. E. Williams, and T. H. Nguyen, "Magnet arrays for synchronous machines," in *Proc. 1993 IEEE Industry Applications Society 28th Annual Meeting*, vol. 1, pp. 9–18, Oct. 1993.

[67] H. Yu and W.-J. Kim, "A compact Hall-effect-sensing 6-DOF precision positioner," *IEEE Trans. Mechatronics*, vol. 15, no. 6, pp. 982−985, Dec. 2010.

[68] C. M. M. van Lierop, "Magnetically levitated planar actuator with moving magnets: Dynamics, commutation and control design," Ph.D. dissertation, Eindhoven University of Technology, Eindhoven, Netherlands, 2008.

[69] V. H. Nguyen and W.-J. Kim, "Novel electromagnetic design for a precision planar positioner moving over a superimposed concentrated-field magnet matrix," *IEEE Trans. Energy Conversion*, vol. 27, no. 1, pp. 52–62, Mar. 2012.

[70] W.-J. Kim, N. D. Bhat, and T. Hu, "Integrated multidimensional positioner for precision manufacturing," *Journal of Engineering Manufacture*, vol. 218, no. 4, pp. 431–442, Apr. 2004.

[71] J. C. Mallinson, "One-sided fluxes–A magnetic curiosity?," *IEEE Trans. Magnetics*, vol. 9, no. 4, Dec. 1973.

[72] K. Halbach, "Design of permanent multipole magnets with oriented rare earth cobalt material," *Nuclear Instruments and Methods*, vol. 169, no. 1, pp. 1–10, Feb. 1980.

[73] K. Halbach, "Physical and optical properties of rare earth cobalt magnets," *Nuclear Instruments and Methods*, vol. 187, no. 1, pp. 109–117, Aug. 1981.

[74] K. Halbach, "Application of permanent magnets in accelerators and electron storage rings," *Journal of Applied Physics*, vol. 57, no. 8, pp. 3605–3608, Apr. 1985.

[75] V. H. Nguyen and W.-J. Kim, "A Two-Phase Framework for Linear Permanent-Magnet Machines and Multi-Axis Stages with Magnetic Levitation", in *Proc. 2014 ASME Dynamic Systems and Control Conference,* No. 5936, Oct. 2014.

[76] McMaster-Carr Supply Company (2015). [Online]. Available: http://www.mcmaster.com/#8574kac/=xprjbi.

[77] Nelson Air Corp. (2015). [Online]. Available: http://www.nelsonair.com/NA_prods_flatpad_fp.htm.

[78] OPTRA Inc. (2015). [Online]. Available: http://www.optra.com/nanogage.html.

[79] GMW Associates. (2015). [Online]. Available: http://www.gmw.com/magnetic_sensors/sentron/2sa/2SA-10.html.

[80] Keysight Technologies. (2015). [Online]. Available: http://www.keysight.com/en/pd-1000001477%3Aepsg%3Apro-pn-5517D/laser-head?cc=US&lc=eng.

[81] Keysight Technologies. (2015). [Online]. Available: http://www.keysight.com/en/pd-1000000994%3Aepsg%3Apro-pn-10706B/high-stability-plane-mirror-interferometer?cc=US&lc=eng.

[82] APEX Microtechnology. (2015). [Online]. Available: https://www.apexanalog.com/apex-products/pa12a/.

[83] Pentek Inc. (2015). [Online]. Available: http://www.pentek.com/products/detail.cfm?model=4284.

[84] Texas Instrument. (2015). [Online]. Available: http://www.ti.com/lit/ds/sprs038/sprs038.pdf.

[85] Pentek Inc. (2015). [Online]. Available: http://www.pentek.com/products/detail.cfm?model=6102.

APPENDIX

A.1 C Code Implemented in Code Composer

This code is compiled into the executable file that is loaded to the DSP board.

File name: **main.h**

```
/*** This is the file to define the global variables for DSP files ***/

/*** Dual port memory address ***/

unsigned long int DSP_COM;          /* Command to DSP*/

unsigned long int POS_COM;          /*Beginning of PC Position input

                                    0x80000002~0x80000007*/

unsigned long int DSPCOM_ACK;   /* Acknowledge to DSP_COM*/

unsigned long int INT_COUNT;       /* Count to interrupt*/

unsigned long int POS_PLATTEN;   /* Beginning of the position data

                                    0x80000020~0x80000025 */

unsigned long int VEL_PLATTEN;   /* Beginning of the velocity data

                                    0x80000026~0x8000002B */

unsigned long int POS_MEASURE;  /* Beginning of the position measurement data

                                    0x80000030~0x80000035 */

unsigned long int CURR_OUTPUT; /* Beginning of the current output

                                    0x80000036~0x8000003B */

unsigned long int FORCE_OUTPUT;/* Beginning of the force output

                                    0x80000040~0x80000045*/

/*************************************/
```

```
unsigned long int ACC_MEASURE; /* Beginning of the acceleration data
                                0x80000060~0x80000065 */
/**************************************/
unsigned long int POS1, POS2, POS3, POS4, POSZ1, POSX2, POSX1, POSY, POS_U;
unsigned long int index;
unsigned long int index2;
int sensor_a1, sensor_a2, sensor_b1, sensor_b2, sensor_c1, sensor_c2, sensor_d2;
float x1,x2, x, xb, xbb, ex, exb, exbb, ux, uxb, uxbb;
float y1,y2, y, yb, ybb, ey, eyb, eybb, uy, uyb, uybb;
float thetaz, thetazb, ethetaz, ethetazb, uthetaz, uthetazi, uthetazd;
float z1,z2,z3, z10,z20,z30, z10b,z20b,z30b;
float z, zb, ez, ezb, uz, uzi, uzd;
float thetax, thetaxb, ethetax, ethetaxb, uthetax, uthetaxi, uthetaxd, uthetaxdb;
float thetay, thetayb, ethetay, ethetayb, uthetay, uthetayi, uthetayd, uthetaydb;
float ux12, ux56, uy34, uy78;
float uyd, uzd, uzdb, uxd;
float uyi, uzi, uxi;
int utemp;
float t, acc, TT;
float xref;
float yref;
float x1r, x2r, x3r, x4r, x5r, x6r, y1r, y2r, y3r, y4r, y5r, y6r, z1r, z2r, z3r;
```

```
float thetax1r, thetax2r, thetay1r, thetay2r;

float thetaz1r, thetaz2r, thetaz3r, thetaz4r;

float step1, step2;

float trigoy, trigox, siny, cosy;

float mx, mtheta;

float i1,i2,i3,i4,i5,i6,i7,i8, i01,i02,i03,i04,i05,i06,i07,i08;

float y1s_temp, y2s_temp, x1s_temp, x2s_temp;

float y1s_tempb, y2s_tempb, x1s_tempb, x2s_tempb;

float pi, L, gama1;

float cf, r;

float cx,cy,sx,sy;

float uz_added, uthetax_added, uthetay_added;

float er0x, er1x, er2x, u0x, u1x, u2x;

float er0y, er1y, er2y, u0y, u1y, u2y;

float er0h, er1h, er2h;

float u0h, u1h, u2h;

float hstart, coupling;

long int raw_y_pos, raw_x1_pos, raw_x2_pos, raw_y_vel, raw_x1_vel;

float y_pos,y_posb, x1_pos,x1_posb, x2_pos,x2_posb;

float y_laser,y_laserb,y_laserbb, x1_laser,x2_laser, x_laser,x_laserb,x_laserbb;

float thetaz_laser, thetaz_laserb;

float y_vel, x1_vel, x2_vel;
```

```
/*** Register Address ***/
unsigned long int            MX_Int_Clr;
unsigned long int            MX_Ctrl;
unsigned long int            Clk1_Div;
unsigned long int            Clk4_Div;
unsigned long int            AD_FIFO_Rst;
unsigned long int            AD_Data_Fmt;
unsigned long int            AD_CkSl_Sct;
unsigned long int            AD_Trig_Ctrl;
unsigned long int            AD_Mask_CD;
unsigned long int            DA_FIFO_Rst;
unsigned long int            DA_Data_Fmt;
unsigned long int            DA_CkSl_Sct;
unsigned long int            DA_Trig_Ctrl;
unsigned long int            AD_FIFO_A1;
unsigned long int            AD_FIFO_A2;
unsigned long int            AD_FIFO_B1;
unsigned long int            AD_FIFO_B2;
unsigned long int            AD_FIFO_C1;
unsigned long int            AD_FIFO_C2;
unsigned long int            AD_FIFO_D1;
unsigned long int            AD_FIFO_D2;    /* newly added */
```

```
unsigned long int            DA_FIFO_A1;
unsigned long int            DA_FIFO_A2;
unsigned long int            DA_FIFO_B1;
unsigned long int            DA_FIFO_B2;
unsigned long int            DA_FIFO_C1;
unsigned long int            DA_FIFO_C2;
unsigned long int            DA_FIFO_D1;
unsigned long int            DA_FIFO_D2;
/*** function ***/
void tr_low(void);
void tr_high(void);
void int_enable(void);
void int_disable(void);
void c_int01();
void adda_setup(void);
void d2a_enable(void);
void d2a_disable(void);
```

File name: **main.c**

```
#include "main.h"
main(){
/* initialize the Dual Port Memory Address */
```

```
/*** Dual port memory address ***/

        DSP_COM=            0x80000000;  /* Command to DSP*/

        POS_COM=            0x80000002;  /* Beginning of PC Position input

                                         0x80000002~0x80000007*/

        DSPCOM_ACK=                 0x80000010;  /* Acknowledge to DSP_COM*/

        INT_COUNT=                  0x80000012;  /* Count to interrupt*/

        POS_PLATTEN=        0x80000020;  /* Beginning of the position data

                                         0x80000020~0x80000025 */

        VEL_PLATTEN=        0x80000026;  /* Beginning of the velocity data

                                         0x80000026~0x8000002B */

        POS_MEASURE=        0x80000030;  /* Beginning of the position measurement

                                         data 0x80000030~0x80000035 */

        CURR_OUTPUT=        0x80000036;  /* Beginning of the current output

                                         0x80000036~0x8000003B */

        FORCE_OUTPUT=       0x80000040;  /* Beginning of the force output

                                         0x80000040~0x80000045*/

        ACC_MEASURE=        0x80000060; /* Beginning of the acceleration data

                                         0x80000060~0x80000065 */

        POS_U = 0x80010000;

        POS1 = 0x80030000;

        POS2 = 0x80050000;

        POS3 = 0x80070000;
```

```
POS4 = 0x80090000;
POSY = 0x800b0000;
POSX1 = 0x800d0000;
POSX2 = 0x800f0000;                    /*for interferometer laser sensors*/
index2 = 0;
pi = 3.141596;
L        =        0.0508;
gama1  =          2 * pi/L;
cf = 13000;
r = 9.6025;
t = 0;
yref = 0;
xref = 0;
TT = 0.3;
step1 = 0.002;
step2 = 0.002;
/*** Register Address ***/
MX_Int_Clr=          0x20000029;
MX_Ctrl=             0x20000028;
Clk1_Div=            0x20000010;
AD_FIFO_Rst=         0x2000001B;
AD_Data_Fmt=         0x20000019;
```

```
AD_CkSl_Sct=        0x2000001C;

AD_Trig_Ctrl=       0x20000014;

AD_Mask_CD=         0x20000018;

DA_FIFO_Rst=        0x2000003B;

DA_Data_Fmt=        0x20000039;

DA_CkSl_Sct=        0x2000003C;

DA_Trig_Ctrl=       0x20000034;

AD_FIFO_A1=         0x20000000;

AD_FIFO_A2=         0x20000001;

AD_FIFO_B1=         0x20000002;

AD_FIFO_B2=         0x20000003;

AD_FIFO_C1=         0x20000004;

AD_FIFO_C2=         0x20000005;

AD_FIFO_D1=         0x20000006;

AD_FIFO_D2=         0x20000007;

DA_FIFO_A1=         0x20000020;

DA_FIFO_A2=         0x20000021;

DA_FIFO_B1=         0x20000022;

DA_FIFO_B2=         0x20000023;

DA_FIFO_C1=         0x20000024;

DA_FIFO_C2=         0x20000025;

DA_FIFO_D1=                 0x20000026;
```

```
DA_FIFO_D2=                    0x20000027;

tr_low();

adda_setup();

/* Initialize the command and flag words */

tr_low();

*(unsigned long int *)DSPCOM_ACK=0;

/*loop*/

tr_low();

y1s_tempb = 0;

y2s_tempb = 0;

x1s_tempb = 0;

x2s_tempb = 0;

xb = 0;

xbb = 0;

yb = 0;

ybb = 0;

zb = 0;

z1 = 0.003;

z2 = 0.003;

z3 = 0.003;


z10b = 0.003;
```

```
z20b = 0.003;
z30b = 0.003;
x1 = 0;
y1 = 0;
x2 = 0;
y2 = 0;
x1r = 0.00027;
x2r = 0.00027;
x3r = 0;
x4r = 0.00656;
x5r = 0.006565;
y1r = 0.00282;
y2r = 0.00282;
y3r = 0.00501;
y4r = 0.0016;
y5r = 0.00161;
thetaz1r = 0.0085;
thetaz2r = 0.0085;
thetaz3r = 0.017;
thetaz4r = 0.018;

z1r = 2986*0.000001;
```

```
        z2r = 2984*0.000001;
        enable_int();
        d2a_enable();
}
```

File name: **int_01.c**

```
#include "dsp.h"
#include "C:\tic3x4x\c3x4x\cgtools\include\math.h"
void c_int01(){
        unsigned long D1reading;
        long ADreading;
        long LSreading;
        tr_low();
        D1reading=*(unsigned long int *)AD_FIFO_D1;     /* Why is it neccessay? */
        if (index2 < 130000){
                *(unsigned int *)(POS4+index2) = D1reading;
                sensor_d2 = (D1reading & 0xffff0000) >> 16;
                if (sensor_d2 > 32767){
                        sensor_d2 = sensor_d2 - 65536;
                }
                ADreading=*(unsigned long int *)AD_FIFO_A1;
                *(unsigned int *)(POS1+index2) = ADreading;
```

```
sensor_a1 = (ADreading & 0x0000ffff);
if (sensor_a1 > 32767){
        sensor_a1 = sensor_a1 - 65536;
}
sensor_a2 = (ADreading & 0xffff0000) >> 16;
if (sensor_a2 > 32767){
        sensor_a2 = sensor_a2 - 65536;
}
ADreading=*(unsigned long int *)AD_FIFO_B1;
*(unsigned int *)(POS2+index2) = ADreading;
sensor_b1 = (ADreading & 0x0000ffff);
if (sensor_b1 > 32767){
        sensor_b1 = sensor_b1 - 65536;
}
sensor_b2 = (ADreading & 0xffff0000) >> 16;
if (sensor_b2 > 32767){
        sensor_b2 = sensor_b2 - 65536;
}
ADreading=*(unsigned long int *)AD_FIFO_C1;
*(unsigned int *)(POS3+index2) = ADreading;
sensor_c1 = (ADreading & 0x0000ffff);
if (sensor_c1 > 32767){
```

```
                    sensor_c1 = sensor_c1 - 65536;}
            sensor_c2 = (ADreading & 0xffff0000) >> 16;
            if (sensor_c2 > 32767){
                    sensor_c2 = sensor_c2 - 65536;
            }
}
    if (index2 < 60000){
            y1s_temp = -asin(sensor_a1/6074.9)*0.008085;
            y1 = 19*y1/21 + 2*y1s_temp/21;
            y2s_temp = asin(sensor_a2/6074.9)*0.008085;
            y2 = 19*y2/21 + 2*y2s_temp/21;
            y = (y1-y2)/2;
            x1s_temp = -asin(sensor_b1/6074.9)*0.008085;
            x1 = 19*x1/21 + 2*x1s_temp/21;
            x2s_temp = asin(sensor_b2/6074.9)*0.008085;
            x2 = 19*x2/21 + 2*x2s_temp/21;
            x = (x2-x1)/2;
            thetaz = (-y1-y2+0.0127)/0.1397;
            trigox = gama1*(x2-0.0742);
            trigoy = gama1*(y1-0.08995);
}
    z10 = (3000+sensor_d2*0.00152588)*0.000001;
```

```
        z20 = (3000+sensor_c1*0.00152588)*0.000001;
        z30 = (3000+sensor_c2*0.00152588)*0.000001;
        z1 = 0.7788*z1 + 0.2212*z10b;
        z2 = 0.7788*z2 + 0.2212*z20b;
        z3 = 0.7788*z3 + 0.2212*z30b;
        z = (z3+z2)/2;
        thetax = (z3-z1)/0.108;
        thetay = (z2-z1)/0.108;
        if (index2<29998){
                *(unsigned int *)DA_FIFO_A1=( (unsigned int)(84) << 16 ) &
0xffff0000 ;
                *(unsigned int *)DA_FIFO_A2=( (unsigned int)(114) << 16 ) &
0xffff0000 ;
                *(unsigned int *)DA_FIFO_B1=( (unsigned int)(50) << 16 ) &
0xffff0000 ;
                *(unsigned int *)DA_FIFO_B2=( (unsigned int)(171) << 16 ) &
0xffff0000 ;
                *(unsigned int *)DA_FIFO_C1=( (unsigned int)(66) << 16 ) &
0xffff0000 ;
                *(unsigned int *)DA_FIFO_C2=( (unsigned int)(-23) << 16 ) &
0xffff0000 ;
                *(unsigned int *)DA_FIFO_D1=( (unsigned int)(0) << 16 ) & 0xffff0000;
```

```
        *(unsigned int *)DA_FIFO_D2=( (unsigned int)(6) << 16 ) & 0xffff0000;
}
if((index2 >= 29998)&(index2 < 30000)){
        ux = 0;
        uxb = 0;
        uxbb = 0;
        uxi = 0;
        uxd = 0;
        uy = 0;
        uyb = 0;
        uybb = 0;
        uyi = 0;
        uyd = 0;
        uthetaz = 0;
        uthetazi = 0;
        uthetazd = 0;
        uthetax = 0;
        uthetaxi = 0;
        uthetaxd = 0;
        uthetay = 0;
        uthetayi = 0;
        uthetayd = 0;
```

```
            uthetaxdb = 0;

            uthetaydb = 0;

            uz = 0;

            uzi = 0;

            uzd = 0;

            uzdb = 0;

            uz_added = 0;

            uthetax_added = 0;

            uthetay_added = 0;

            x1_posb = 0;

            x2_posb = 0;

            y_posb = 0;

            x1_laser = 0;

            x2_laser = 0;

            y_laser = 0;

            x_laserb = 0;

            x_laserbb = 0;

            y_laserb = 0;

            y_laserbb = 0;

    }


    if ((index2 >= 30000)&(index2 < 59000)){
```

```
if (index2 == 58999){
thetax1r = thetax;
thetay1r = thetay;
}
ex = x1r - x;
exb = x1r - xb;
exbb = x1r - xbb;
ey = y2r - y;
eyb = y2r - yb;
eybb = y2r - ybb;
ethetaz = thetaz1r - thetaz;
ethetazb = thetaz1r - thetazb;
ez = z1r - z;
ezb = z1r - zb;
ethetax = thetax1r - thetax;
ethetaxb = thetax1r - thetaxb;
ethetay = thetay1r - thetay;
ethetayb = thetay1r - thetayb;
ux = 1.9448*uxb - 0.9448*uxbb + 6416*ex - 12782.6*exb + 6367*exbb;
uy = 1.9448*uyb - 0.9448*uybb + 6416*ey - 12782.6*eyb + 6367*eybb;

uthetazi = uthetazi + 0.0015*ethetazb;
```

```
        uthetazd = 1200*(ethetaz-ethetazb);
        uthetaz = uthetazi + 6*ethetaz + uthetazd;
        sx = sin(trigox);
        cx = cos(trigox);
        sy = sin(trigoy);
        cy = cos(trigoy);
i01 =  sx*ux  +  0.5*cx*(uz+uz_added)  -  2*r*cx*uthetax  +  r*sx*uthetaz;
i02 = -cx*ux  +  0.5*sx*(uz+uz_added)  -  2*r*sx*uthetax  -  r*cx*uthetaz;
i03 =  cy*uy  -  0.5*sy*(uz+uz_added)  +  2*r*sy*uthetay  +  r*cy*uthetaz;
i04 =  sy*uy  +  0.5*cy*(uz+uz_added)  -  2*r*cy*uthetay  +  r*sy*uthetaz;
i05 =  cx*ux  -  0.5*sx*(uz+uz_added)  -  2*r*sx*uthetax  -  r*cx*uthetaz;
i06 = -sx*ux  -  0.5*cx*(uz+uz_added)  -  2*r*cx*uthetax  +  r*sx*uthetaz;
i07 = -sy*uy  -  0.5*cy*(uz+uz_added)  -  2*r*cy*uthetay  +  r*sy*uthetaz;
i08 = -cy*uy  +  0.5*sy*(uz+uz_added)  +  2*r*sy*uthetay  +  r*cy*uthetaz;
        if (i01>2.318) {i01 = 2.318;}
        if (i01<-2.318) {i01 = -2.318;}
        if (i02>2.318) {i02 = 2.318;}
        if (i02<-2.318) {i02 = -2.318;}
        if (i03>2.318) {i03 = 2.318;}
        if (i03<-2.318) {i03 = -2.318;}
        if (i04>2.318) {i04 = 2.318;}
        if (i04<-2.318) {i04 = -2.318;}
```

```
if (i05>2.318) {i05 = 2.318;}

if (i05<-2.318) {i05 = -2.318;}

if (i06>2.318) {i06 = 2.318;}

if (i06<-2.318) {i06 = -2.318;}

if (i07>2.318) {i07 = 2.318;}

if (i07<-2.318) {i07 = -2.318;}

if (i08>2.318) {i08 = 2.318;}

if (i08<-2.318) {i08 = -2.318;}

i1 = 14130*i01 + 84.46;

i2 = 13490*i02 + 114.20;

i3 = 14100*i03 + 50.14;

i4 = 13450*i04 + 171.50;

i5 = 13820*i05 + 66.55;

i6 = 13410*i06 - 23.49;

i7 = 13495*i07;

i8 = 13480*i08 + 6.49;

uxbb = uxb;

uxb = ux;

uybb = uyb;

uyb = uy;
```

```
*(unsigned int *)DA_FIFO_A1=( (unsigned int)(i1) << 16 ) & 0xffff0000 ;
*(unsigned int *)DA_FIFO_A2=( (unsigned int)(i2) << 16 ) & 0xffff0000 ;
*(unsigned int *)DA_FIFO_B1=( (unsigned int)(i3) << 16 ) & 0xffff0000 ;
*(unsigned int *)DA_FIFO_B2=( (unsigned int)(i4) << 16 ) & 0xffff0000 ;
*(unsigned int *)DA_FIFO_C1=( (unsigned int)(i5) << 16 ) & 0xffff0000 ;
*(unsigned int *)DA_FIFO_C2=( (unsigned int)(i6) << 16 ) & 0xffff0000 ;
*(unsigned int *)DA_FIFO_D1=( (unsigned int)(i7) << 16 ) & 0xffff0000 ;
*(unsigned int *)DA_FIFO_D2=( (unsigned int)(i8) << 16 ) & 0xffff0000 ;
}
if((index2 >= 59000)&(index2 < 59001)){
        laser_setup();
}
if((index2 >= 59500)&(index2 < 60000)){
        /* F = 4 for plane mirror optics */
        /* where lamda is a laser wavelength (632.991 nm) */
        /* lamda/(F*2^22*100ns)= 3.77292037e-7, */
        /* METERS-BIT approx 0.625 nm */
        /* write down y_pos, x1_pos, x2_pos to memory and read by gel*/
        tr_low();
        *(unsigned long int *)0xb0300003=0x0041;
        raw_y_pos  = (*(long int *)0xb0300048 << 16) & 0xffff0000;
        raw_x1_pos = (*(long int *)0xb0310048 << 16) & 0xffff0000;
```

```
raw_x2_pos = (*(long int *)0xb0320048 << 16) & 0xffff0000;

raw_y_vel  = (*(long int *)0xb030004e << 16) & 0xffff0000;

raw_x1_vel = (*(long int *)0xb031004e << 16) & 0xffff0000;

raw_x2_vel = (*(long int *)0xb032004e << 16) & 0xffff0000;

tr_high();

raw_y_pos  |= ((*(long int *)0xb0300048 >> 16) & 0x0000ffff);

raw_x1_pos |= ((*(long int *)0xb0310048 >> 16) & 0x0000ffff);

raw_x2_pos |= ((*(long int *)0xb0320048 >> 16) & 0x0000ffff);

raw_y_vel  |= ((*(long int *)0xb030004e >> 16) & 0x0000ffff);

raw_x1_vel |= ((*(long int *)0xb031004e >> 16) & 0x0000ffff);

raw_x2_vel |= ((*(long int *)0xb032004e >> 16) & 0x0000ffff);

*(unsigned int *)(POSY+index2) = raw_y_pos;

*(unsigned int *)(POSX1+index2) = raw_x1_pos;

*(unsigned int *)(POSX2+index2) = raw_x2_pos;

y_pos=raw_y_pos*6.1815119987e-10;

x1_pos=raw_x1_pos*6.1815119987e-10;

x2_pos=raw_x2_pos*6.1815119987e-10;

y_vel = raw_y_vel * 3.77292037e-7;

x1_vel= raw_x1_vel* 3.77292037e-7;

x2_vel= raw_x2_vel* 3.77292037e-7;

x1_laser = 9*x1_laser/11 + x1_pos/11 + x1_posb/11;

x2_laser = 9*x2_laser/11 + x2_pos/11 + x2_posb/11;
```

```
y_laser = 9*y_laser/11 + y_pos/11 + y_posb/11;
x_laser = (x1_laser + x2_laser)/2;
thetaz_laser = (x1_laser - x2_laser)/0.055;
ex = 0 - x_laser;
exb = 0 - x_laserb;
ey = 0 + y_laser;
eyb = 0 + y_laserb;
ethetaz = 0 - thetaz_laser;
ethetazb = 0 - thetaz_laserb;
ez = z1r - z;
ezb = z1r - zb;
ethetax = thetax1r - thetax;
ethetaxb = thetax1r - thetaxb;
ethetay = thetay1r - thetay;
ethetayb = thetay1r - thetayb;
trigox = gama1*(x2 - 0.0742 + x_laser);
trigoy = gama1*(y1 - 0.08995 - y_laser);
y_posb = y_pos;
x1_posb = x1_pos;
x2_posb = x2_pos;
x_laserbb = x_laserb;
x_laserb = x_laser;
```

```
        y_laserbb = y_laserb;
        y_laserb = y_laser;
        thetaz_laserb = thetaz_laser;
        ux = 0;
        uxb = 0;
        uxbb = 0;
        uxi = 0;
        uxd = 0;
        uy = 0;
        uyb = 0;
        uybb = 0;
        uyi = 0;
        uyd = 0;
        uthetaz = 0;
        uthetazi = 0;
        uthetazd = 0;
*(unsigned int *)DA_FIFO_A1=( (unsigned int)(84) << 16 ) & 0xffff0000 ;
*(unsigned int *)DA_FIFO_A2=( (unsigned int)(114) << 16 ) & 0xffff0000 ;
*(unsigned int *)DA_FIFO_B1=( (unsigned int)(50) << 16 ) & 0xffff0000 ;
*(unsigned int *)DA_FIFO_B2=( (unsigned int)(171) << 16 ) & 0xffff0000 ;
```

```
*(unsigned int *)DA_FIFO_C1=( (unsigned int)(66) << 16 ) & 0xffff0000 ;
*(unsigned int *)DA_FIFO_C2=( (unsigned int)(-23) << 16 ) & 0xffff0000 ;
*(unsigned int *)DA_FIFO_D1=( (unsigned int)(0) << 16 ) & 0xffff0000 ;
*(unsigned int *)DA_FIFO_D2=( (unsigned int)(6) << 16 ) & 0xffff0000 ;
}
if ((index2 >= 60000)&(index2 < 129999)){
        tr_low();
        *(unsigned long int *)0xb0300003=0x0041;
        raw_y_pos  = (*(long int *)0xb0300048 << 16) & 0xffff0000;
        raw_x1_pos = (*(long int *)0xb0310048 << 16) & 0xffff0000;
        raw_x2_pos = (*(long int *)0xb0320048 << 16) & 0xffff0000;
        raw_y_vel  = (*(long int *)0xb030004e << 16) & 0xffff0000;
        raw_x1_vel = (*(long int *)0xb031004e << 16) & 0xffff0000;
        raw_x2_vel = (*(long int *)0xb032004e << 16) & 0xffff0000;
        tr_high();
        raw_y_pos  |= ((*(long int *)0xb0300048 >> 16) & 0x0000ffff);
        raw_x1_pos |= ((*(long int *)0xb0310048 >> 16) & 0x0000ffff);
        raw_x2_pos |= ((*(long int *)0xb0320048 >> 16) & 0x0000ffff);
        raw_y_vel  |= ((*(long int *)0xb030004e >> 16) & 0x0000ffff);
        raw_x1_vel |= ((*(long int *)0xb031004e >> 16) & 0x0000ffff);
        raw_x2_vel |= ((*(long int *)0xb032004e >> 16) & 0x0000ffff);
```

```
*(unsigned int *)(POSY+index2) = raw_y_pos;

*(unsigned int *)(POSX1+index2) = raw_x1_pos;

*(unsigned int *)(POSX2+index2) = raw_x2_pos;

y_pos=raw_y_pos*6.1815119987e-10;

x1_pos=raw_x1_pos*6.1815119987e-10;

x2_pos=raw_x2_pos*6.1815119987e-10;

y_vel = raw_y_vel * 3.77292037e-7;

x1_vel= raw_x1_vel* 3.77292037e-7;

x2_vel= raw_x2_vel* 3.77292037e-7;

x1_laser = 0.7788*x1_laser + 0.2212*x1_posb;

x2_laser = 0.7788*x2_laser + 0.2212*x2_posb;

y_laser = 0.7788*y_laser + 0.2212*y_posb;

x_laser = (x1_laser + x2_laser)/2;

thetaz_laser = (x1_laser - x2_laser)/0.055;

ey = 0 + y_laser;

eyb = 0 + y_laserb;

eybb = 0 + y_laserbb;

ethetaz = 0 - thetaz_laser;

ethetazb = 0 - thetaz_laserb;

acc = 25*step1;

if (index2 < 115000){

        ex =  0 - x_laser;
```

```
            exb = 0 - x_laserb;

}

if ((index2 >= 115000) & (index2 < 115400)){

            t = t + 0.00025;

            xref = acc*t;

            xref = xref*t;

            ex =  xref - x_laser;

            exb = xref - x_laserb;

}

if ((index2 >= 115400) & (index2 < 115800)){

            t = t + 0.00025;

            xref = step1/4 + acc*(t-0.1)*0.2;

            ex =  xref - x_laser;

            exb = xref - x_laserb;

}

if ((index2 >= 115800) & (index2 < 116200)){

            t = t + 0.00025;

            xref = step1 - acc*(0.3-t)*(0.3-t);

            ex =  xref - x_laser;

            exb = xref - x_laserb;

}
```

```
if ((index2 >= 116200) & (index2 < 123000)){

        ex =  step1 - x_laser;

        exb = step1 - x_laserb;

        t = 0;

}

if ((index2 >= 123000) & (index2 < 123400)){

        t = t + 0.00025;

        xref = step1 - acc*t*t;

        ex =  xref - x_laser;

        exb = xref - x_laserb;

}

if ((index2 >= 123400) & (index2 < 123800)){

        t = t + 0.00025;

        xref = 0.75*step1 - acc*(t-0.1)*0.2;

        ex =  xref - x_laser;

        exb = xref - x_laserb;

}

if ((index2 >= 123800) & (index2 < 124200)){

        t = t + 0.00025;

        xref = acc*(0.3-t)*(0.3-t);

        ex =  xref - x_laser;

        exb = xref - x_laserb;}
```

```
if (index2 >= 124200){
            ex =  0 - x_laser;
            exb = 0 - x_laserb;
}
ethetax = thetax1r - thetax;
ethetaxb = thetax1r - thetaxb;
ethetay = thetay1r - thetay;
ethetayb = thetay1r - thetayb;
if (index2 < 109000){
            ez = z1r - z;
            ezb = z1r - zb;
}
if (index2 >= 109000){
            ez = z2r - z;
            ezb = z2r - zb;
}
uxi = uxi + 240*(ex + exb);
uxd = -35*(x1_vel + x2_vel);
ux = uxi + uxd + 24000*ex;
uyi = uyi + 240*(ey + eyb);
uyd = 55*y_vel;
uy = uyi + uyd + 24000*ey;
```

```
uthetazi = uthetazi + 0.3*ethetazb;

uthetazd = -3*(x1_vel-x2_vel);

uthetaz = uthetazi + 15*ethetaz + uthetazd;

if (index2 >= 70000){

        uthetaxi = uthetaxi + 0.4*(ethetax+ethetaxb);

        uthetaxd = 500*(ethetax-ethetaxb);

        uthetax = uthetaxi + 32*ethetax + uthetaxd;

        uthetayi = uthetayi + 0.4*(ethetay+ethetayb);

        uthetayd = 500*(ethetay-ethetayb);

        uthetay = uthetayi + 36*ethetay + uthetayd;

}

if ((index2 >= 80000) & (index2 < 109000)){

        if(ez > 0.000002){

                uz_added = uz_added + 0.0002;

        }

        if(ez < -0.000002){

                uz_added = uz_added - 0.0002;

        }

}

if (index2 >= 109000){

        uzi = uzi + 70*(ez + ezb);
```

```
                uzd = 0.9992*uzdb + 70.31*(ez - ezb);
                uz = uzi + uzd + 40000*ez;
            }
            trigox = gama1*(x2 - 0.0742 + x_laser);
            trigoy = gama1*(y1 - 0.08995 - y_laser);
            sx = sin(trigox);
            cx = cos(trigox);
            sy = sin(trigoy);
            cy = cos(trigoy);
        i01 =  sx*ux  +  0.5*cx*(uz+uz_added)  -  2*r*cx*(uthetax+uthetax_added)  +
r*sx*uthetaz;
        i02 = -cx*ux  +  0.5*sx*(uz+uz_added)  -  2*r*sx*(uthetax+uthetax_added)  -
r*cx*uthetaz;
        i03 =  cy*uy  -  0.5*sy*(uz+uz_added)  +  2*r*sy*(uthetay+uthetay_added)  +
r*cy*uthetaz;
        i04 =  sy*uy  +  0.5*cy*(uz+uz_added)  -  2*r*cy*(uthetay+uthetay_added)  +
r*sy*uthetaz;
        i05 =  cx*ux  -  0.5*sx*(uz+uz_added)  -  2*r*sx*(uthetax+uthetax_added)  -
r*cx*uthetaz;
        i06 = -sx*ux  -  0.5*cx*(uz+uz_added)  -  2*r*cx*(uthetax+uthetax_added)  +
r*sx*uthetaz;
```

```
        i07 = -sy*uy - 0.5*cy*(uz+uz_added) - 2*r*cy*(uthetay+uthetay_added) +
r*sy*uthetaz;
        i08 = -cy*uy + 0.5*sy*(uz+uz_added) + 2*r*sy*(uthetay+uthetay_added) +
r*cy*uthetaz;
        utemp = 10000*i01;
        *(unsigned int *)(POS_U + index2 - 60000) = utemp;
        /*
        *(unsigned int *)(POS_U + index2 - 60000) = raw_x1_vel; */
                if (i01>2.318) {i01 = 2.318;}
                if (i01<-2.318) {i01 = -2.318;}
                if (i02>2.318) {i02 = 2.318;}
                if (i02<-2.318) {i02 = -2.318;}
                if (i03>2.318) {i03 = 2.318;}
                if (i03<-2.318) {i03 = -2.318;}
                if (i04>2.318) {i04 = 2.318;}
                if (i04<-2.318) {i04 = -2.318;}
                if (i05>2.318) {i05 = 2.318;}
                if (i05<-2.318) {i05 = -2.318;}
                if (i06>2.318) {i06 = 2.318;}
                if (i06<-2.318) {i06 = -2.318;}
                if (i07>2.318) {i07 = 2.318;}
                if (i07<-2.318) {i07 = -2.318;}
```

```
if (i08>2.318) {i08 = 2.318;}
if (i08<-2.318) {i08 = -2.318;}
i1 = 14130*i01 + 84.46;
i2 = 13490*i02 + 114.20;
i3 = 14100*i03 + 50.14;
i4 = 13450*i04 + 171.50;
i5 = 13820*i05 + 66.55;
i6 = 13410*i06 - 23.49;
i7 = 13495*i07;
i8 = 13480*i08 + 6.49;
y_posb = y_pos;
x1_posb = x1_pos;
x2_posb = x2_pos;
x_laserbb = x_laserb;
x_laserb = x_laser;
y_laserbb = y_laserb;
y_laserb = y_laser;
thetaz_laserb = thetaz_laser;
uxbb = uxb;
uxb = ux;
uybb = uyb;
uyb = uy;
```

```
        uthetaxdb = uthetaxd;
        uthetaydb = uthetayd;
        uzdb = uzd;
*(unsigned int *)DA_FIFO_A1=( (unsigned int)(i1) << 16 ) & 0xffff0000 ;
*(unsigned int *)DA_FIFO_A2=( (unsigned int)(i2) << 16 ) & 0xffff0000 ;
*(unsigned int *)DA_FIFO_B1=( (unsigned int)(i3) << 16 ) & 0xffff0000 ;
*(unsigned int *)DA_FIFO_B2=( (unsigned int)(i4) << 16 ) & 0xffff0000 ;
*(unsigned int *)DA_FIFO_C1=( (unsigned int)(i5) << 16 ) & 0xffff0000 ;
*(unsigned int *)DA_FIFO_C2=( (unsigned int)(i6) << 16 ) & 0xffff0000 ;
*(unsigned int *)DA_FIFO_D1=( (unsigned int)(i7) << 16 ) & 0xffff0000 ;
*(unsigned int *)DA_FIFO_D2=( (unsigned int)(i8) << 16 ) & 0xffff0000 ;
}
if((index2 >= 129999)&(index2 < 130000)){
*(unsigned int *)DA_FIFO_A1=( (unsigned int)(84) << 16 ) & 0xffff0000 ;
*(unsigned int *)DA_FIFO_A2=( (unsigned int)(114) << 16 ) & 0xffff0000 ;
*(unsigned int *)DA_FIFO_B1=( (unsigned int)(50) << 16 ) & 0xffff0000 ;
*(unsigned int *)DA_FIFO_B2=( (unsigned int)(171) << 16 ) & 0xffff0000 ;
*(unsigned int *)DA_FIFO_C1=( (unsigned int)(66) << 16 ) & 0xffff0000 ;
*(unsigned int *)DA_FIFO_C2=( (unsigned int)(-23) << 16 ) & 0xffff0000 ;
*(unsigned int *)DA_FIFO_D1=( (unsigned int)(0) << 16 ) & 0xffff0000 ;
*(unsigned int *)DA_FIFO_D2=( (unsigned int)(6) << 16 ) & 0xffff0000 ;}
```

```
        y1s_tempb = y1s_temp;

        y2s_tempb = y2s_temp;

        x1s_tempb = x1s_temp;

        x2s_tempb = x2s_temp;

        z10b = z10;

        z20b = z20;

        z30b = z30;

        xbb = xb;

        xb = x;

        ybb = yb;

        yb = y;

        thetazb = thetaz;

        zb = z;

        thetaxb = thetax;

        thetayb = thetay;

        index2 = index2 + 1;

        MX_Int_Clr= 0x20000029;

        *(unsigned int *)MX_Int_Clr=0x0;

}
```

A.2 Matlab Code Used for Data Analysis

This m file is to read the measurements of the vertical laser sensors stored in the txt files and plot the out-of-plane positions of the moving platen.

```
%sta = textread('anew2000.txt','%s');
%stb = textread('bnew2000.txt','%s');
stc = textread('cnew1240.txt','%s');
std = textread('dnew1240.txt','%s');
muiM0 = 0.71;  zs = 26.74 * 0.001;  L = 0.0508;  gama = 2 * pi / L;
delta = 0.0127;
Bs_siny_ratio = -(2/pi)*(2^0.5)*muiM0*(1-exp(-gama*delta))*exp(-
gama*zs);  Co = 1000*327.68*Bs_siny_ratio;
numby1 = 1:1:65000;
numby2 = 1:1:65000;
numbx1 = 1:1:65000;
numbx2 = 1:1:65000;
numbz1 = 1:1:65000;
numbz2 = 1:1:65000;
numbz3 = 1:1:65000;
t1 = 1:1:65000;
t11 = (t1-1)/4000;
for i = 1:65000
%     tempa = char(sta(i+5));
%     tempb = char(stb(i+5));
      tempc = char(stc(i+5));
      tempd = char(std(i+5));
```

```
%    numby2(i) = hex2dec(strcat(tempa(3),tempa(4),tempa(5),tempa(6)));
%    numby1(i) = hex2dec(strcat(tempa(7),tempa(8),tempa(9),tempa(10)));
%    numbx2(i) = hex2dec(strcat(tempb(3),tempb(4),tempb(5),tempb(6)));
%    numbx1(i) = hex2dec(strcat(tempb(7),tempb(8),tempb(9),tempb(10)));
     numbz3(i) = hex2dec(strcat(tempc(3),tempc(4),tempc(5),tempc(6)));
     numbz2(i) = hex2dec(strcat(tempc(7),tempc(8),tempc(9),tempc(10)));
     numbz1(i) = hex2dec(strcat(tempd(3),tempd(4),tempd(5),tempd(6)));
end
for i = 1:65000
%     if numby1(i) > 2^15
%         numby1(i) = numby1(i)-2^16;
%     end
%     if numby2(i) > 2^15
%         numby2(i) = numby2(i)-2^16;
%     end
%     if numbx1(i) > 2^15
%         numbx1(i) = numbx1(i)-2^16;
%     end
%     if numbx2(i) > 2^15
%         numbx2(i) = numbx2(i)-2^16;
%     end
    if numbz1(i) > 2^15
        numbz1(i) = numbz1(i)-2^16;
    end
    if numbz2(i) > 2^15
        numbz2(i) = numbz2(i)-2^16;
    end
```

```
    if numbz3(i) > 2^15
        numbz3(i) = numbz3(i)-2^16;
    end
end
t2 = 1:1:65000;
t22 = (t2-1)/4000;
y1 = 1:1:65000;
y2 = 1:1:65000;
y = 1:1:65000;
x1 = 1:1:65000;
x2 = 1:1:65000;
x = 1:1:65000;
z1 = 1:1:65000;
z2 = 1:1:65000;
z3 = 1:1:65000;
z = 1:1:65000;
phi = 1:1:65000;
ba_y1 = 1:1:65000;
ba_y2 = 1:1:65000;
ba_x1 = 1:1:65000;
ba_x2 = 1:1:65000;
theta = 1:1:65000;
thetax = 1:1:65000;
thetay = 1:1:65000;
for i = 1:65000
      z1(i) = 3000+(numbz1(i)/32768)*50;
      z2(i) = 3000+(numbz2(i)/32768)*50;
```

```
      z3(i) = 3000+(numbz3(i)/32768)*50;

      z(i) = (z3(i)+z2(i))/2;

      thetax(i) = 0.0000092593*(z3(i)-z1(i));

      thetay(i) = 0.0000092593*(z2(i)-z1(i));

end

u_id = 1:1:8000;

z_id = (z(48000:55999)-2977.85)*0.000001;

for i = 1:8000

    u_id(i) = 0.00025*i;

end

% figure

% plot(t22,z3),grid,xlabel('time (s)'), ylabel('um'),title('Sensor 3');

% figure

% plot(t22,z2),grid,xlabel('time (s)'), ylabel('um'),title('Sensor 2');

% figure

% plot(t22,z1),grid,xlabel('time (s)'), ylabel('um'),title('Sensor 1');

% figure

figure

plot(t22,z),grid,xlabel('time (s)'), ylabel('um'),title('z');

figure

plot(t22,thetax),grid,xlabel('time (s)'),

ylabel('rad'),title('thetax');

figure

plot(t22,thetay),grid,xlabel('time (s)'),

ylabel('rad'),title('thetay');
```

A.3 Out-of-Plane Error Torques Generated by the Horizontal Lorentz Forces

With the 4 pairs of overlapped coils and the precision mirrors added to the platen, its center of mass is estimated in SolidWorks to be approximately at the top surface of the plastic frame of the platen, as can be seen in Fig. 3-6. The thickness of the coil sides that are effective for force generation is only 2.54 mm. The acting points of the horizontal forces can be considered to be in the symmetrical plane between the top and the bottom surfaces of the coil sides. Therefore, the distance to calculate the out-of-plane error torque generated by the horizontal Lorentz forces is $(0.380 - 0.045) \times 0.0254 = 0.0085$ m. Compared with the distance of 0.0521 m to calculate the torques generated by the forcers to actuate the control axes in θ_x and θ_y, the ratio is 16%. This means that the X-direction Lorentz force ($F_{x,12}$) generated by the forcer 1&2 causes an error torque of 16% of the torque generated by the Z-direction force from the forcer 3&4 ($F_{z,34}$) about the Y'-axis, providing that $F_{x,12} = F_{z,34}$. However, since the achieved acceleration in x and y does not exceed 2 m/s^2, the maximum current flown in the coils can be as large as 2.5 A, and the mass of the platen is only 0.75 kg, in addition to the amount of current to magnetically levitate the platen, larger $F_{z,34}$ can be generated to outweigh or cancel the error torque generated by $F_{x,12}$.

To examine this in detail, a set of control efforts in all 6 axes are given and the associated currents are calculated as follows. The control effort in x, $u_x = 1$ A, is theoretically sufficient to generate an acceleration of 2.26 m/s^2 in x. The control effort in z, $u_z = 4$ A, is able to magnetically levitate the platen of 0.75 kg. The control effort in θ_y, $u_{\theta y} = 0.0085$, is sufficient to cancel the error torque generated by the Lorentz forces in x.

The positions of the base points for the Lorentz force calculation, x_2 and y_8, as seen in Fig. 3-5(a), are varied in an entire spatial pitch of the magnet matrix, which is 0.0508 m. The currents flown in the 8 coils calculated from (3.10) do not exceed 1.9 A, which is well below the limit of 2.5 A. This means that an extra amount of current up to 0.6 A can be used to generate accelerations in both x and y, and to cancel other force or torque disturbances if necessary.